NEAR INFRARED STUDIES OF REFLECTION NEBULAE

Thesis by

Kristen Sellgren

In partial Fulfillment of the Requirements

for the Degree of

Doctor of Philosophy

California Institute of Technology

Pasadena, California

1983

(submitted May 10, 1983)

Dedication

To all the women whose pioneering efforts and continued support have made my achievements possible.

ACKNOWLEDGEMENTS

The people who have been most important in shaping the course of my graduate school career have been my advisors, Tom Soifer and Gerry Neugebauer. I can never thank Tom enough for his infinite patience with teaching me professional self-reliance and scientific judgement, and with reading all the many versions of the papers in my thesis. I would like to thank Gerry for financial support and for making Caltech infrared group equipment available to me, and for having encouraged me to pursue a varied and interesting career. Mike Werner, who was my advisor for my first two years at Caltech, has also strongly influenced my scientific development. It has been a pleasure to collaborate with Mike on one of the papers in my thesis, and I thank him for his insight and constructive criticism.

A number of people, in addition to my advisors, have contributed significantly to the development of the ideas contained in my thesis. Stan Whitcomb collaborated with me on the original 2.2 μm observations of extended emission and stars in NGC 7023. I thank him for his contribution to our original interpretation of the extended emission as reflected light, and regret that he has not been involved in the re-interpretation of my thesis data. I would also like to thank Harriet Dinerstein for her collaboration on one of the papers in my thesis. I thank Mike Jura and Rick White for a number of conversations about reflection nebulae and possible explanations of my observations; Adolf Witt for sending me his visual observations of NGC 7023 and NGC 2023 and for his continued interest in infrared observations of reflection nebulae; and Judy Cohen for her interest in the stellar clusters in the reflection nebulae and for taking visual spectra of some of the stars for me.

The observations in my thesis would not have been possible without the infrared equipment built and maintained by Keith Matthews. I have greatly appreciated the hospitality and assistance of the staffs of the Infrared Telescope

Facility, and especially, Mount Wilson Observatory. Night assistants Jim Frazer and Howard Lanning at Mount Wilson were especially helpful in surviving my many and long observing runs. I would also like to acknowledge the financial support of NASA and NSF throughout my graduate career.

I would like to thank the following colleagues for their friendship, encouragement, and moral support throughout my years at Caltech: Graham Berriman, Geoff Blake, Judy Cohen, Barbara Cooper, Harriet Dinerstein, David Ennis, Erich Grossman, Jocelyn Keene, Mark Keil, John Lacy, Pat Neill, Beth Nordholt, JJ Nugent, Tom Roellig, Ann Rosenthal, Anneila Sargent, Ed Sutton, Dan Watson, and Rick White. My friends outside of Caltech were also instrumental in preserving my sanity. I would like to thank the following people for their love and support: Cathy Barber, Jan Bogstad, Cindy Friedman, Anne Lee, Joan Leech, Sande Staley, Laurie Tanenbaum, and Marie Wood. Finally, I would like to thank Rick, Cindy, David, Joan, and Jody for their very special friendship.

ABSTRACT

Near infrared studies have been made of the extended emission from, and stellar clusters within, three visual reflection nebulae, NGC 7023, 2023, and 2068. The extended emission from each nebula consists of a smooth continuum from 1.25 to 4.8 μm, which can be described by a greybody with a color temperature of $\sim$ 1000 K, and strong emission features at 3.3 and 3.4 μm. The spectrum is the same in all three sources, and is independent of position over regions 0.4-0.9 pc in diameter within each source. The 2.2 μm surface brightness distributions in NGC 7023 and 2023 agree well with the distributions of visual reflected light. The continuum emission cannot be explained by free-free emission, reflected light, fluorescent processes, field stars, or thermal emission from grains in equilibrium with the stellar radiation field.

A model is proposed in which the extended emission is due to thermal emission from very small grains (radius $\sim$ 10 Å) which are briefly heated to $\sim$ 1000 K by absorption of an ultraviolet photon. This model explains the agreement between near infrared and visual surface brightness distributions, and the constancy of the energy distribution with offset from the central stars. The numbers of 10 Å sized grains required by the observations are in agreement with the numbers expected from an extrapolation of the grain size distribution of Mathis, Rumpl, and Nordsieck (1977) to smaller grain sizes.

Clusters of young stars found associated with the reflection nebulae NGC 7023, 2023, and 2068 have also been studied at near infrared wavelengths. At least 30-60 % of the stars found at 2.2 μm are pre-main sequence objects, as indicated by their infrared excesses, hydrogen line emission, or irregular variability. The spatial distributions and observed luminosity functions of these young open clusters are derived, and the inferred mass function and star formation efficiencies are discussed.

TABLE OF CONTENTS

INTRODUCTION

Visual reflection nebulae are astronomical sources whose emission at visual wavelengths is due to light from a central star reflected from dust grains in the surrounding nebula. Studies of the reflected light in these sources have in the past provided much information on the scattering properties of the dust grains at visual wavelengths, which in turn has constrained models of the size and composition of the grains. The work described in this thesis was begun to extend observations of the grain scattering properties to previously unstudied wavelengths of 1 to 5 μm. Three visual reflection nebulae, NGC 7023, 2023, and 2068, were selected for near infrared observations, on the basis of having central illuminating stars that were bright, yet did not ionize substantial amounts of hydrogen whose free-free emission might overwhelm starlight reflected from dust, and on the basis of their being associated with dust clouds containing enough column density of dust to make reflected light detectable at near infrared wavelengths, yet a small enough column density that the illuminating stars are not too obscured to be well studied at visual wavelengths.

The primary discovery of the observations described in this thesis is that the near infrared emission detected in the three reflection nebulae NGC 7023, 2023, and 2068 is not due to reflected light. More importantly, no well-known emission mechanism could explain the observations. The goal of this thesis has been to understand the source of the near infrared emission of these three nebulae, by a combination of astronomical observations and detailed examination of possible emission mechanisms.

This thesis consists of three papers. The first paper, written in collaboration with M. W. Werner and H. L. Dinerstein, briefly reports the discovery of the anomalous character of the near infrared emission of NGC 7023, 2023, and 2068. Spectra from 1.9 to 3.7 μm with 1% spectral resolution,

obtained for positions in NGC 7023 and NGC 2023, show that the near infrared emission consists of a smooth continuum from 2 to 5 μm, and strong emission features at 3.3 and 3.4 μm. The continuum emission can be described by a dilute blackbody with a color temperature of $\sim$ 1000 K. The features at 3.3 and 3.4 μm are two of six unidentified infrared emission features seen in many astronomical sources, for which neither the material nor the emission mechanism is known. Broadband photometry at 2.2, 3.8, and 4.8 μm, and 1% resolution spectrophotometry at the wavelength of the 3.3 μm feature, is also presented for several positions in NGC 7023, 2023, and 2068. These observations show the shape of the continuum energy distribution and the 3.3 μm feature-to-continuum ratio is the same in all three nebulae, in all positions observed. The first paper also summarizes briefly some of the possible emission mechanisms for the near infrared emission, which are discussed in more detail in the second paper.

The second paper presents further observations of NGC 7023, 2023, and 2068 and detailed analysis of possible emission mechanisms. Maps of the reflection nebulae at 2.2 μm show the emission has a strong peak near the central star, decreases smoothly with distance from the star, and extends over a region 0.4-0.9 pc in diameter. The 2.2 μm and visual surface brightness distributions are compared and found to agree very well. Results of photometry of many positions at 1.25 and 1.65 μm are also given, and show that the near infrared colors are the same in all three nebulae, and show no dependence on distance from the central star. A spectrum, with 5% resolution from 1.5 to 2.5 μm, for one position in NGC 7023 demonstrates that the near infrared continuum emission continues to be smooth and featureless to wavelengths as short as 1.5 μm.

A number of emission mechanisms can be ruled out for the observed near infrared emission. Reflected light would produce near infrared emission much fainter and with a much different energy distribution than is observed. Thermal emission from dust grains in equilibrium with the radiation field of the central star can be ruled out because of the high value of the color temperature, ~ 1000 K, over distances from the central star of 0.2-0.4 pc. Fluorescence from grains or molecules cannot produce the smooth continuum observed over a factor of 4 in wavelength. Faint, undetected stars can contribute only a small amount to the observed emission because they have colors very different from that of the nebulae, and because the numbers of faint stars predicted from the luminosity function observed in the third paper are too few. Free-free emission from ionized hydrogen can be ruled out by the lack of corresponding continuum radio emission.

One model that may be able to explain the observations is thermal emission from small grains which are briefly heated to high temperatures upon absorption of an ultraviolet photon. Other mechanisms for inducing thermal fluctuations in small grains, such as collisions with atoms, are examined and found not to be as plausible or effective as ultraviolet photons. The grain radii required in this model are ~ 10 Å, but only a small fraction of the total dust mass need be contained in the small grains. The number of small grains required by the observations are in good agreement with the numbers predicted from a current model for the size distribution of interstellar grains. The thermal fluctuation model has the advantage of explaining quite naturally the observed agreement between the 2.2 μm and visual surface brightness distributions, since both the near infrared emission and visual reflected light are proportional to the incident stellar flux, and also predicts the energy distribution of the near infrared emission should be independent of position

within the nebula, as is observed.

The third paper in this thesis concerns the properties of stars found near the reflection nebulae. These observations were made initially to correct the observations of extended near infrared emission for the contributions of field stars, but the stars found in 2.2 μm scans were discovered to be members of a young cluster which is interesting in its own right. Near infrared photometry of these stars show that many are pre-main sequence stars, with infrared variability or infrared excesses due to circumstellar shells. These indicators, together with hydrogen line emission which is also characteristic of pre-main sequence stars, are used to establish lower limits to the fraction of pre-main sequence stars in these clusters of 30-60%. The spatial distributions of the stars show strong clustering, with a surface density of stars varying as the inverse of the projected distance from the cluster center. The observations are used to derive a luminosity function at 2.2 μm for the young clusters, and estimates of the mass function and star formation efficiencies are made.

In summary, this thesis presents a wide range of observational approaches to understanding both the extended near infrared nebular emission from, and the young stellar clusters within, visual reflection nebulae. A model is proposed which argues for the near infrared emission being due to thermal fluctuations in small grains. This postulates a previously undetected grain population in the interstellar medium.

PAPER I: EXTENDED NEAR INFRARED EMISSION FROM VISUAL REFLECTION NEBULAE

ABSTRACT

Extended near infrared (2–5 μm) emission has been observed from three visual reflection nebulae, NGC 7023, 2023, and 2068. The emission from each nebula consists of a smooth continuum, which can be described by a greybody with a color temperature of 1000 K, and emission features at 3.3 and 3.4 μm. The continuum emission cannot be explained by free-free emission, reflected light, or field stars, or by thermal emission from grains, with commonly accepted ratios of infrared to ultraviolet emissivities, which are in equilibrium with the stellar radiation field. A possible explanation is thermal emission from grains with extremely low ratios of infrared to ultraviolet emissivities, or from grains with a temperature determined by mechanisms other than equilibrium radiative heating. Another possibility is continuum fluorescence.

I. INTRODUCTION

This paper reports photometric and spectrophotometric observations of extended near infrared emission from three visual reflection nebulae, NGC 7023, 2023, and 2068. These observations reveal that the near infrared emission in all three nebulae consists of a smooth continuum which can be described by a color temperature of $\sim$ 1000 K, and strong emission features at 3.3 and 3.4 μm. Emission processes hitherto thought to be important in infrared sources appear to be incapable of explaining these observations.

II. OBSERVATIONS

Observations were made of NGC 7023, 2023, and 2068 on 1982 October 8-13 using the Infrared Telescope Facility at Mauna Kea Observatory. A solid nitrogen cooled InSb detector was used with standard photometric filters at K (λ = 2.20 μm, $\Delta\lambda$ = 0.42 μm), L' (λ = 3.77 μm, $\Delta\lambda$ = 0.66 μm), and M (λ = 4.8 μm, $\Delta\lambda$ = 0.57 μm). A circular variable filter wheel with 1% resolution from 1.9 to 3.7 μm was also used.

The observations were made with a 12" diameter diaphragm, and a spacing in right ascension between source and sky positions of 2-3'. Maps at 2.2 μm of the extended emission in the nebulae (Sellgren 1983) were consulted in order to ensure that the surface brightness of the sky positions was negligible.

The observations were calibrated using standard techniques, described in more detail by Sellgren (1983). The observations of NGC 7023 have been corrected for the contribution of instrumental scattered light from the illuminating star of the visual reflection nebula. This correction, about 10% at most, was determined by observations of isolated bright stars.

III. RESULTS

Spectrophotometry of the extended emission in NGC 7023 and NGC 2023 from 1.9 to 3.7 μm is shown in Figure 1. The near infrared emission consists of a

smooth, relatively flat continuum and a bright emission feature at 3.3 μm, with a broad emission wing centered at 3.4 μm. These features at 3.3 and 3.4 μm have been observed in other infrared sources (Aitken 1981). The broadband photometry at 2.2, 3.8 and 4.8 μm is also shown in Figure 1. The 3.8 μm broadband filter extends from 3.44 to 4.10 μm, so that it should exclude the strong 3.3 μm feature and most of the weaker 3.4 μm feature. The spectra of both sources look very similar, both in the continuum shape and in the strength of the 3.3 μm feature relative to the continuum.

Table 1 gives the 2.2, 3.8, and 4.8 μm surface brightnesses of all positions observed in NGC 7023, 2023, and 2068. The shape of the continuum emission from NGC 7023 and 2023 can be characterized by the temperature of a greybody passing through the broadband points. The 2.2 to 3.8 μm color temperatures can be seen in Table 1 to be similar at all positions in these nebulae, ranging from 900 to 1100 K. The 2.2 to 4.8 μm color temperature ranges from 900 to 1300 K.

The strength of the 3.3 μm emission feature, relative to the continuum, also varies little among the various nebular positions. Table 1 gives the observed surface brightness at the peak of the 3.3 μm feature, measured with the 1% circular variable filter wheel. It also gives the ratio of the 3.3 μm feature, corrected for the continuum at 3.3 μm estimated from the 2.2 and 3.8 μm broadband points, to the 3.3 μm continuum. The feature-to-continuum ratio in NGC 7023, 2023, and 2068 is nearly constant, with values between 3 and 8, and an average value of 6. For comparison, the sources discussed by Dwek *et al.* (1980) have 3.3 μm feature-to-continuum ratios of 0.4 to 4, while the observations of the Orion nebula by Sellgren (1981) show that the 3.3 μm feature-to-continuum ratio in that source varies from < 0.15 to 7 across the nebula. Thus the 3.3 μm feature-to-continuum ratios observed in the three reflection nebulae are among

the highest found, and furthermore are considerably more constant than is observed from source to source in other objects, or between different positions in spatial mapping of the Orion nebula.

IV. DISCUSSION

Our observations pose two separate questions. The first is the origin of the unidentified emission features, which is a long-standing mystery. The second is the source of the extended continuum emission. As is discussed below, the emission mechanisms believed to be important in other infrared sources are inadequate to explain the continuum emission, particularly the high and uniform color temperature over an extended region. The association in these visual reflection nebulae of the strong 3.3 μm feature with the anomalous continuum emission, as shown by the constant 3.3 μm feature-to-continuum ratio, suggests that the two phenomena may have similar explanations or even a common physical basis.

a. The 3.3 μm emission feature

The emission feature at 3.3 μm and its wing at 3.4 μm, observed in the three reflection nebulae, are two of six unidentified infrared emission features between 3.3 and 11.3 μm, usually seen together, for which neither the material nor the emission mechanism is known. The breadth of the features (Tokunaga and Young 1980; Grasdalen and Joyce 1976; Bregman and Rank 1975) indicate that the emitting material is in the solid phase. Current models for the emission mechanism, fluorescence excited by ultraviolet (UV) radiation (Allamandola, Greenberg, and Norman 1979) and thermal emission from small grains heated by UV radiation (Dwek *et al.* 1980), fail to explain the observed 3.3 μm emission in the reflection nebulae. The fluorescence model requires too high a UV fluorescence efficiency (Dwek *et al.* 1980), while the thermal emission model is unable to account for the high brightness temperature of the 3.3 μm emission,

190K.

b. The extended near infrared continuum emission

Many possible emission mechanisms have been investigated in searching for the source of the observed extended near infrared continuum emission; detailed arguments will be given in a later paper (Sellgren 1983). The following emission mechanisms appear to be unable to account for the continuum emission:

1) Free-free emission. Measurements of 6 cm emission in NGC 2023 and 2068 and upper limits on 6 cm emission from NGC 7023 (Sellgren *et al.* 1983) predict near infrared surface brightnesses due to free-free emission accounting for less than 1% of the observed near infrared emission.

2) Reflected light. The observed surface brightness of NGC 2023 exceeds by a factor of 3 at 2.2 μm, and a factor of 20 at 3.8 μm, the maximum surface brightness possible for reflected light from any of the known stellar sources associated with the region, including the visual illuminating star. Similarly NGC 7023 and 2068 are brighter by factors of 5-6 at 3.8 μm than the maximum possible surface brightness of reflected light. The true contribution of reflected light to the observed infrared surface brightness is probably significantly less than the maximum possible, since the actual nebular geometries and grain properties will likely differ from those which produce the maximum amount of reflected light.

3) Faint stars. An argument against the observed emission being due to faint members of the stellar clusters associated with the reflection nebulae is that the emission appears uniformly extended, in diaphragms with diameters between 6" and 60". Furthermore, Sellgren (1983) has shown, using the surface density of stars and luminosity functions observed in these regions, that the expected 2.2 μm surface brightness from faint stars is < 10% of the observed 2.2 μm emission.

4) Thermal emission from "normal" dust. The observed constancy of the continuum color temperature with distance from the central star is a problem for explaining the observations by thermal dust emission. A more severe problem, however, is the high value of the inferred dust temperature. The brightness temperature of the 2.2 μm emission is $\sim$ 240 K in the three reflection nebulae, implying a minimum dust temperature of 240 K if the emission is due to thermal dust emission. In fact the dust presumably would have a temperature close to the observed color temperature of the emission, 1000 K, much higher than would be expected either from calculations or by comparison with observations of dust in other regions.

Near infrared emission is observed at a distance of 1' from the early B stars, with luminosities $L_* \sim 4-12 \times 10^3\ L_\odot$, which illuminate the visual reflection nebulae. This 1' distance corresponds to $r \cong 0.15$ pc at the distances of the nebulae (Viotti 1969; Lee 1968). If the grains are in equilibrium with the stellar radiation field then the dust temperature T_d is given by $T_d = (Q_{UV}\, L_*)^{\frac{1}{4}} (16\, \pi\, \sigma\, r^2\, Q_{IR})^{-\frac{1}{4}}$, where Q_{UV} and Q_{IR} are the Planck averaged ultraviolet and infrared emissivities, and σ is the Stefan-Boltzmann constant. With $L_* = 10^4\ L_\odot$ and $r = 0.15$ pc, $T_d = 17\ (Q_{UV}/Q_{IR})^{\frac{1}{4}}$ K. The values of Q_{IR}/Q_{UV} predicted from calculations based on laboratory measurements of candidate grain materials (Draine 1981; Jones *et al.* 1977; Jones and Merrill 1976; Leung 1975; Aannestad 1975) fall between those corresponding to infrared emissivities proportional to λ^{-1} and λ^{-2}. These emissivities in turn imply $T_d = 70$ - 150 K.

In the Orion ridge (Becklin *et al.* 1976) grain temperatures of 60 - 300 K are seen, which, scaled to the lower fluxes of heating radiation appropriate to the visual reflection nebulae, would correspond to $T_d = 40$ - 200 K. Thus grain parameters derived either from calculations or from observations in other regions predict grain temperatures far below the observed color temperature of

1000 K, and well below even the 2.2 μm brightness temperature of 240 K observed in NGC 7023, 2023, and 2068. Both the far infrared observations (Whitcomb *et al.* 1981; Emerson, Furniss, and Jennings 1975; Harvey, Thronson, and Gatley 1980; Sargent 1982) and the radio observations (Sellgren *et al.* 1983) indicate that the visual illuminating stars are the most luminous stars in the reflection nebulae, so there do not appear to be any other sources of heating which might produce higher grain temperatures in these nebulae.

c. Speculations

The problem with explaining the near infrared emission lies in the shape of the energy distribution rather than its integrated luminosity, which is $\sim 10^{-2}$ of the total luminosity of the illuminating stars of the visual reflection nebulae. The small luminosity of the unexplained continuum emission, and the fact that this emission was found in all three reflection nebulae observed, argue that the emission observed here may be a widespread phenomenon whose small contribution to the total luminosity of more complex regions may have been masked by other near infrared continuum emission mechanisms (e.g., free-free emission) with larger shares of the total luminosity.

While several mechanisms discussed above have failed to explain the observed emission, other possibilities exist which will be explored in more detail in a later paper (Sellgren 1983). One possibility is thermal emission from grains with a ratio of the average infrared emissivity to the average UV emissivity $\sim 10^4$ - 10^7 times lower than the ratio inferred from calculations or observations of other sources, in order to account for the extremely high color temperatures observed. In this case a mechanism to hold the grain temperature constant with distance from the star, such as a sublimation process, would also be needed. Another possibility for producing the observed continuum by thermal emission is very small grains, which momentarily reach a high temperature following the

absorption of individual UV photons or after collisions (Harwit 1975; Purcell 1976). The peak temperature of such a thermally fluctuating grain would be to first order independent of position, thus explaining the lack of a radial temperature gradient in these sources. A third possible explanation is that fluorescence in grains produces not only emission features such as the 3.3 and 3.4 μm features, as suggested by Allamandola, Greenberg, and Norman (1979), but also a smooth continuum extending at least from 2 to 5 μm. Whatever the final explanation proves to be, it is clear that infrared observations of these nebulae have identified a phenomenon in the interstellar medium whose existence has not been previously suspected, and whose explanation may lead us to a better understanding of interstellar grains.

We thank R. Capps, Y. Pendleton, and our telescope operators C. Kaminski and D. Griep for assistance with the observations; the Infrared Telescope Facility for providing their RC-2 InSb system; and E. Erickson for the loan of a 2-4 μm circular variable filter wheel. We also thank S. Whitcomb and M. Harwit for useful discussions. Financial support was provided by NASA and NSF. HLD was supported by NASA Ames Research Center-University of Texas Joint Research Interchange NCA2-OR781-201.

REFERENCES

Aannestad, P.A. 1975, *Ap. J.*, **200**, 30.

Aitken, D. K. 1981, in IAU Symposium **96**, *Infrared Astronomy*, eds. C.G. Wynn-Williams and D.P. Cruikshank (Dordrecht:Reidel).

Allamandola, L. J., Greenberg, J. M., and Norman, C. A. 1979, *Astr. Ap.*, **77**, 66.

Becklin, E. E., Beckwith, S., Gatley, I., Matthews, K., Neugebauer, G., Sarazin, C., and Werner, M. W. 1976, *Ap. J.*, **207**, 770.

Bregman, J. D. and Rank, D. M. 1975, *Ap. J. (Letters)*, **195**, L125.

Draine, B. T. 1981, *Ap. J.*, **245**, 880.

Dwek, E., Sellgren, K., Soifer, B. T., and Werner, M. W. 1980, *Ap. J.*, **238**, 140.

Emerson, J. P., Furniss, I., and Jennings, R. E. 1975, *M. N. R. A. S.*, **172**, 411.

Grasdalen, G. L. and Joyce, R. R. 1976, *Ap. J. (Letters)*, **205**, L11.

Harvey, P. M., Thronson, H. A., and Gatley, I. 1980, *Ap. J.*, **235**, 894.

Harwit, M. 1975, *Ap. J.*, **199**, 398.

Jones, T.W., Leung, C.M., Gould, R.J., and Stein, W.A. 1977, *Ap. J.*, **212**, 52.

Jones, T.W. and Merrill, K.M. 1976, *Ap. J.*, **209**, 509.

Lee, T.A. 1968, *Ap. J.*, **152**, 913.

Leung, C.M. 1975, *Ap. J.*, **199**, 340.

Purcell, E. M. 1976, *Ap. J.*, **206**, 685.

Sargent, A. I. 1982, private communication.

Sellgren, K. 1981, *Ap. J.*, **245**, 138.

Sellgren, K. 1983, in preparation.

Sellgren, K., Becker, R., Pravdo, S.H., and White, R.L. 1983, in preparation.

Tokunaga, A. T. and Young, E. T. 1980, *Ap. J. (Letters)*, **237**, L93.

Viotti, R. 1969, *Mem. Soc. Astr. Ital.* **40**,75.

Whitcomb, S.E., Gatley, I., Hildebrand, R.H., Keene, J., Sellgren, K., and Werner, M.W. 1981, *Ap. J.*, **246**, 416.

Table 1

Position[a]	$S_{2.2}$[b]	$S_{3.8}$[b]	$S_{4.8}$[b]	$T_c\left(\frac{2.2}{3.8}\right)^c$	$T_c\left(\frac{2.2}{4.8}\right)^c$	$S_{3.3}$[b]	Feature[d] / Cont
			NGC 7023				
30" W 20" N	7.0	20	12 ±3	1020	1300 ±100	100	6.0
30" N	5.5	18	24 ±6	980	940 ±70	74	5.0
60" N	2.1	5.7 ±0.6		1050 ±50		36 ±3	7.6 ±0.8
60" S	1.4	5.5 ±0.8		910 ±50		29 ±2	7.0 ±0.8
120" N	0.31 ±0.04	<3.2		>690		<12	<15
			NGC 2023				
60" S	4.8	15 ±1	9.8 ±3.5	990 ±30	1200 ±200	86	7.0 ±0.4
60" N	2.0	5.1 ±0.5		1090 ±40		17 ±1	3.4 ±0.3
40" W 40" S	3.7	13 ±1		950 ±30			
			NGC 2068				
60" E 40" S	0.93	3.9 ±0.7		900 ±60		18 ±2	6.3 ±1.1

(a) Offset from illuminating star of visual reflection nebula, which is HD 200775, HD 37903, and HD 38563-N for NGC 7023, 2023, and 2068 respectively.

(*b*) Surface brightness measured with broad band filters at 2.2, 3.8, and 4.8 μm, and with 1% resolution at the peak of the 3.3 μm feature, uncorrected for continuum. Units are 10^{-20} W m^{-2} Hz^{-1} $ster^{-1}$. Uncertainties are ± 1 σ and are given only when larger than 5%. All limits are 3-σ limits, except at NGC 2023 60" S, where the 4.8 μm observation given is a 2.8 σ measurement.

(*c*) Color temperatures (K) determined from ratios of surface brightnesses at 2.2 and 3.8 μm, and from ratios at 2.2 and 4.8 μm.

(*d*) Surface brightness in 3.3 μm feature, corrected for continuum, divided by 3.3 μm continuum surface brightness estimated from observed surface brightness at 2.2 and 3.8 μm. For NGC 7023 120" N, the 3.8 μm surface brightness was estimated from an average ratio of 2.2 to 3.8 μm surface brightnesses and the measured 2.2 μm surface brightness.

Figure Caption

Figure 1. Spectrophotometry (filled circles) with 1% resolution, from 1.9 to 3.7 μm, is shown of (*top*) NGC 7023 and (*bottom*) NGC 2023. Photometry (open squares) at 2.2, 3.8, and 4.8 μm is also shown. Error bars indicate $\pm 1\ \sigma$ statistical uncertainties when larger than 5 %. The units are mJy within a 12" diameter diaphragm; the left hand scale refers to NGC 7023 (*top*) while the right hand scale refers to NGC 2023 (*bottom*). The nebular positions measured are (*top*) 30" W 20" N of HD 200775, and (*bottom*) 60" S of HD 37903, where these stars are the illuminating stars of the visual reflection nebulae. Also shown is a curve representing a greybody fit through the 2.2 and 4.8 μm broad band measurements. The color temperature is 1300 K for NGC 7023 (*top*) and 1200 K for NGC 2023 (*bottom*). The wavelength coverage of the 2.2 μm (K), 3.8 μm (L'), and 4.8 μm (M) broad band filters is also shown at the bottom of the figure.

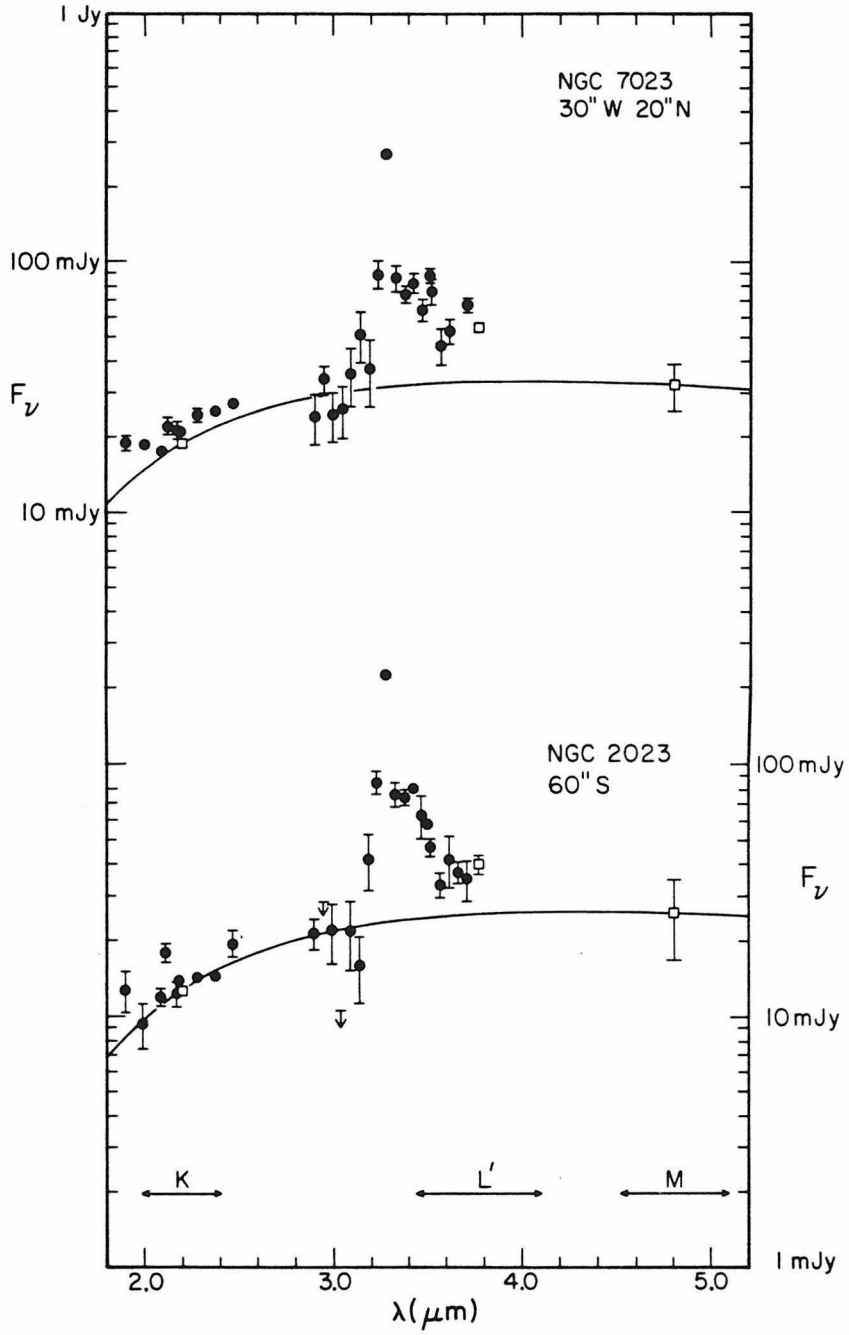
1 Jy
100 mJy
10 mJy
F_ν
NGC 7023
30" W 20"N
NGC 2023
60" S
100 mJy
10 mJy
1 mJy
F_ν
K
L'
M
2.0
3.0
4.0
5.0
λ(μm)

Figure 1

PAPER II: THE NEAR INFRARED CONTINUUM EMISSION OF VISUAL REFLECTION NEBULAE

ABSTRACT

The near infrared emission of the visual reflection nebulae NGC 7023, 2023, and 2068 is found to consist of a smooth continuum from 1.25 to 4.8 μm, characterized by a color temperature of ~ 1000 K, and strong emission features at 3.3 and 3.4 μm. The spectrum is the same in all three sources, and is independent of position over regions 0.4-0.9 pc in diameter within each source. The 2.2 μm surface brightness distributions in NGC 7023 and 2023 agree well with the distributions of visual reflected light.

A model is proposed in which the emission is due to thermal emission from very small grains (radius ~ 10 Å) which are briefly heated to ~ 1000 K by absorption of indiviudal ultraviolet photons. This model explains the agreement between near infrared and visual surface brightness distributions, and the constancy of the energy distribution with offset from the central stars. The number of 10 Å sized grains required by the observations is in agreement with the numbers expected from an extrapolation of the grain size distribution of Mathis, Rumpl, and Nordsieck (1977) to smaller grain sizes.

I. INTRODUCTION

Reflection nebulae have provided in the past an astrophysical laboratory well-suited for the study of the reflection properties of interstellar dust grains at visual and ultraviolet wavelengths. The observations of this paper were begun with the goal of extending to near infrared wavelengths the study of grains in reflection. Three classical visual reflection nebulae, NGC 7023, 2023, and 2068, were observed between 1.25 and 2.2 μm. Soon two mysteries were uncovered: all three nebulae had similar near infrared colors, despite widely different colors of their illuminating stars, and two of the nebulae were much brighter at 2.2 μm than could be easily explained by reflected light. Observations were subsequently obtained of the nebulae at longer wavelengths (Sellgren, Werner, and Dinerstein 1983*a*, hereafter paper 1) and of the 2.2 μm polarization (Sellgren *et al.* 1983*b*). These observations showed that the near infrared extended emission of these nebulae: (1) consisted of a smooth continuum whose spectrum could be characterized by a color temperature of $\sim$ 1000 K; (2) showed the unidentified 3.3 and 3.4 μm features, seen in many other infrared sources, in emission; (3) had a 2.2 μm polarization much lower than was expected for reflected light; and (4) had a surface brightness at 3.8 μm far in excess of what could be explained by reflected light, for all three nebulae. A number of emission mechanisms were considered briefly in paper 1, most of which were found to be unlikely. The most viable mechanisms discussed were thermal emission from dust grains with ratios of infrared to ultraviolet emissivities much lower than is usually found from observations or theory; thermal emission from grains small enough to be heated briefly to high temperatures, by individual ultraviolet (UV) photons or by collisions; and fluorescent mechanisms producing a continuum.

This paper presents near infrared mapping, photometry, and spectrophotometry of these three nebulae, in order to expand on the observations of paper 1 and to provide as much observational insight into the phenomenon of the unexplained continuum emission as possible. Detailed considerations are also presented of a wide variety of possible emission mechanisms, with the aim of understanding the source of the emission, and its implications for the composition of the interstellar medium. To date no satisfactory explanation of all the observations is available.

II. OBSERVATIONS

Observations of NGC 7023 in 1979 August and 1981 July, and of NGC 2023 and NGC 2068 in 1981 January-February and 1981 October, were made using the 24 inch telescope at Mt. Wilson Observatory. Diaphragms of 30" and 60" diameter were used. The spacing between source and sky positions was 3' in right ascension in 1979 and 6' in right ascension in 1981. An InSb detection system was used to obtain nebular surface photometry at wavelengths of 1.25 μm (J), 1.65 μm (H), and 2.2 μm (K). The positional uncertainties of the surface brightness maps are estimated to be ± 4".

The Mt. Wilson Observatory 60 inch telescope was used to obtain spectrophotometry, from 1.5 to 2.5 μm with $\Delta\lambda/\lambda$ = 0.05, of HD 200775, the central star of NGC 7023, in 1979 November and 1980 June, and of the NGC 7023 nebula, 23" north and 14" west of HD 200775, in 1980 June. A circular variable filter wheel cooled to 77 K was used. The nebular measurements were made with a 16" diameter diaphragm and 77" spacing in right ascension between source and sky positions. Broadband photometry at 1.25, 1.65, and 2.2 μm was also obtained for star and nebula.

The Infrared Telescope Facility at Mauna Kea Observatory was used to obtain spectrophotometry, between 1.9 and 3.7 μm with $\Delta\lambda/\lambda$ = 0.01, of the central stars of NGC 7023, 2023, and 2068 in 1982 October, as well as broadband photometry at 1.25 μm, 1.65 μm, 2.2 μm, 3.5 μm (L), 3.8 μm (L'), and 4.8 μm (M). A 12" diameter diaphragm and a spacing in right ascension of 2-3' between source and sky positions was used. A circular variable filter wheel at 77 K was used for the spectrophotometry. Spectrophotometry between 1.9 and 3.7 μm and photometry at 1.25, 1.65, 2.2, 3.8, and 4.8 μm was also obtained at various positions in the three nebulae.

The surface brightness photometry and spectrophotometry of NGC 7023 required correction for instrumental scattered light from HD 200775. This correction, of order 10-20%, was determined by observations of isolated bright stars, and has been applied to all observations of NGC 7023 reported in this paper.

The observed nebular surface brightnesses were corrected for the contributions of field stars found in 2.2 μm scans of NGC 7023, 2023, and 2068 by Sellgren (1983, hereafter paper 2), using the stellar magnitudes and positions listed there. In NGC 2068 the observations of Strom, Strom, and Vrba (1976) were also included in correcting for field stars.

All observations were calibrated using the standard stars of Elias *et al.* (1982) and Neugebauer (1982). Since L' and M magnitudes were not available in all cases, the L magnitude was adopted at longer wavelengths for a few stars of spectral type A or earlier. The flux densities for zero magnitude listed by Beckwith *et al.* (1976) and Neugebauer *et al.* (1979) were adopted. The photometric filters used are described in paper 1 and by Neugebauer *et al.* (1982), except for the L filter, which has λ = 3.50 μm and $\Delta\lambda$ = 1.05 μm. The spectrophotometry with 1% and 5% resolution was calibrated assuming that the early type standard stars could be approximated by 9700 K blackbodies normalized to the 2.2 μm broad band point. No correction for Brackett γ absorption in the standard stars was made. This correction should be 3% or less for the stars used to calibrate the 1% resolution spectrophotometry, 1% or less for the 5% resolution spectrophotometry, and negligible in all cases for the 2.2 μm broadband filter (Elias 1978).

III. RESULTS

In paper 1 photometry at 2.2, 3.8, and 4.8 μm, and spectrophotometry from 1.9 to 3.7 μm, were presented for a few positions in NGC 7023, 2023, and 2068. This paper expands the observations of these sources to include surface brightness maps at 2.2 μm, photometry at many positions at 1.25 and 1.65 μm, and spectrophotometry extending the shortest wavelength observed with medium resolution to 1.5 μm. These additional observations strengthen the conclusions of paper 1, showing the near infrared emission extends over regions 3–6' in diameter with the same 1.25–4.8 μm energy distribution at all positions. This section discusses the results of the observations of reflection nebulae in detail, including comparisons with observations at visual, mid infrared, and far infrared wavelengths.

a. The spatial distribution

The maps of the surface brightness of NGC 7023 at 2.2 and 1.65 μm are shown in Figure 1, while the maps of the surface brightnesses of NGC 2023 and NGC 2068 at 2.2 μm are shown in Figure 2. The 2.2 and 1.65 μm surface brightness distributions of NGC 7023 resemble each other closely. The integrated 2.2 μm flux densities of the nebulae, excluding the contributions of their illuminating stars and other field stars, are 1.5, 4.1, and 3.0 Jy for NGC 7023, 2023, and 2068 respectively.

In NGC 7023, 2023, and 2068 respectively 5, 2, and 6 of the stars whose contributions were subtracted from the near infrared surface photometry are pre-main sequence stars (paper 2) which may be or are variable. Positions containing contributions from known pre-main sequence stars were given lower weight or ignored in the analysis. Additional uncertainties in the photometry arise from the high surface density of stars near the centers of the stellar clusters. The near infrared surface brightness of NGC 2068 (Fig. 2) is uncertain

by typically ± 1 contour interval within a radius of ~ 1' from its central star, due to the combined positional uncertainties of the stellar and nebular positions. The uncertainties due to star subtraction in any of the nebulae should not affect the general surface brightness level, extent, and integrated flux densities of the near infrared maps, or the average properties of the near infrared colors.

The near infrared, far infrared, and visual surface brightness distributions are similar in NGC 7023 and NGC 2023, sharing in common the general locations of the peak surface brightnesses, north and south of the central star for NGC 7023 and 2023 respectively, the general extent of the emission, and the bar of emission 1' south of the star in NGC 7023. The visual radiation from the nebulae is starlight from the central stars reflected by dust grains in the surrounding molecular clouds, while the far infrared emission (Whitcomb *et al.* 1981; Harvey, Thronson, and Gatley 1980) is due to thermal radiation from dust grains at temperatures of 40 - 60 K.

A quantitative comparison of the distribution of visual and near infrared emission in NGC 7023 and 2023 can be found in Figures 3 and 4, which show at 0.55 μm and 2.2 μm the nebular surface brightness as a function of angular offset from the visual illuminating stars. The ratio of surface brightnesses at 0.55 μm and 2.2 μm in these two nebulae is remarkably constant, generally varying by no more than a factor of 2, over regions where the absolute values of the visual and infrared surface brightnesses vary by a factor of ~ 20.

The ratio of visual (V) and 2.2 μm (K) surface brightnesses additionally has a similar value in NGC 7023 and NGC 2023. For NGC 7023 $V-K$ = 2.7 mag, while $V-K$ = 3.2 mag for NGC 2023, where these are average values in the nebulae. In NGC 2068, at one position observed at visual wavelengths by Zellner (1970), $V-K$ = 2.8 mag, in good agreement with the average values for NGC 7023 and NGC 2023.

b. The energy distribution

Near infrared spectra at selected positions in NGC 7023 and 2023 are shown in Figure 5. These spectra clearly show that the near infrared emission of these nebulae is characterized by a smooth continuum from 1.5 to 3.7 μm, a strong emission feature at 3.3 μm, and a broad emission wing near 3.4 μm. The emission features at 3.3 and 3.4 μm are two of six unidentified infrared emission features, whose observed properties have been reviewed by Aitken (1981) and Willner (1983). The broad band photometry at 1.25 and 4.8 μm agrees well with extrapolations of the continuum observed between 1.5 and 3.7 μm, suggesting that the smooth continuum extends at least from 1.25 to 4.8 μm.

Figure 6 shows the ratio of the strength of the 3.3 μm feature, corrected for continuum, to the continuum strength, plotted *vs.* the ratio of 3.8 to 2.2 μm surface brightnesses for positions observed in NGC 7023, 2023, and 2068. The color temperature defined by the broadband observations at 2.2 and 3.8 μm in NGC 7023, 2023, and 2068 appears to be the same, ~ 1000 K, for all nebulae, and is independent of position within each nebula (paper 1). The 3.3 μm feature-to-continuum ratio also appears to be constant at a value of ~ 6 in each of these nebulae (paper 1). Thus the observed values generally fall in the same portion of Figure 6, with the most discrepant point having a 3.3 μm feature-to-continuum ratio a factor of ~ 2 less than other positions, but the same ratio of 3.8 to 2.2 μm surface brightness. This generally good agreement again shows the similarity of the continuum color temperature, and 3.3 μm feature-to-continuum ratio, everywhere in the three nebulae.

The colors at shorter wavelengths are also apparently independent of position. The results of surface photometry at 1.25 μm (J), 1.65 μm (H), and 2.2 μm (K) in the three reflection nebulae are shown in Figure 7. The range of colors (paper 2) for stars in the nebulae, including the stars which illuminate the

visual reflection nebulosity, is outlined in Figure 7. The near infrared colors of the reflection nebulae are extremely different from the colors of the stars within the reflection nebulae.

The observed $J-H$ and $H-K$ colors of NGC 7023, 2023, and 2068 are plotted *vs.* projected radial offset from the visual illuminating stars in Figure 8. The values of $J-H$ and $H-K$ are clearly independent of projected radial distance, emphasizing the similarity of nebular colors at all positions.

The conclusion that the nebular energy distribution is independent of position within the nebula makes it possible to use integrated flux densities at 2.2 μm for each nebula, combined with an average nebular energy distribution, to determine the total flux density of the nebulae at wavelengths between 1.25 and 4.8 μm. The total energy distribution of each nebula is shown in Figure 9, in units of the flux per logarithmic frequency interval. This figure demonstrates that the near infrared emission from 1.25 to 4.8 μm is a small fraction of the total luminosity of the nebulae. Most of the nebular energy is emitted at far infrared wavelengths as thermal radiation from dust at temperatures of 40 - 60 K. The far infrared luminosity is typically 30-50 % of the stellar luminosity, while the near infrared emission accounts for only ~ 1 % of the stellar luminosity.

c. The central stars

The photometry and spectrophotometry of the central stars of the reflection nebulae are shown in Figure 10. The spectra of these stars are featureless, as expected, except for weak 3.3 μm emission in the central star of NGC 2023, with a feature-to-continuum ratio of 0.35, presumably due to the contribution of the nebular emission within the 12" diaphragm. Upper limits of 0.15 can be placed on the 3.3 μm feature-to-continuum ratios in HD 200775 and HD 38563-N. The 2.2 μm surface brightnesses near the central stars inferred from the 3.3 μm feature-to-continuum ratios are consistent with a smooth

interpolation of the 2.2 μm surface brightness maps. The detection of a nebular contribution to near infrared measurements of HD 37903 with a 12" diaphragm implies care must be taken, as has been noted by Guetter (1979), with both the diaphragm size and separation of source and sky positions when determining the extinction curves of early type stars near molecular clouds, especially when the value of $R = A_V/E(B-V)$ is inferred from the longest wavelength photometry obtained.

IV. DISCUSSION

a. Overview of the problem

The main features of the near infrared observations of these visual reflection nebulae that must be explained are the spatial distribution and the energy distribution of the emission. The near infrared surface brightness distributions in two of the nebulae show strong peaks near the illuminating star of the visual reflection nebula, and agree with the surface brightness distributions of the visual reflected light. The energy distribution consists of a smooth continuum from 1.25 to 4.8 μm which is characterized by a color temperature of $\sim$ 1000 K, in addition to the unidentified 3.3 and 3.4 μm emission features; the spectrum is seen to be the same in all three nebulae, and to be independent of position or distance from the central star within each nebula, over a region 3-6' in diameter, or 0.4-0.9 pc at the distances (Viotti 1969; Lee 1968) of these nebulae.

The observations above, and in particular the source of the near infrared continuum emission, are not easily understood. In Appendix A five mechanisms are studied in detail and are found to be unable to explain the continuum emission. Section IV*b* presents a possible model which may explain the observations. I would like to emphasize that the true explanation may prove to be none of the mechanisms discussed in this paper.

The mechanisms for producing the near infrared continuum emission discussed in Appendix A are equilibrium thermal emission, fluorescence, reflected light, stars, and free-free emission. A brief summary of the reasons why these mechanisms can be ruled out is given here; further details are given in Appendix A.

Equilibrium thermal emission is ruled out by the high value of the observed color temperature, $\sim$ 1000 K, at distances $\gtrsim$ 0.1 pc from a moderate luminosity

B star. Thermal emission from dust with very low ratios of infrared to ultraviolet emissivities, $Q_{IR}/Q_{UV} \sim 10^{-7}$, would account for the observed color temperature, but would then be inconsistent with the observed spatial distribution of the emission and fail to explain the constancy of the observed color temperature with distance from the central star. Fluorescent processes may produce line emission, such as has been proposed for the 3.3 and 3.4 μm emission features (Allamandola, Greenberg, and Norman 1979), but are unable to produce the remaining smooth, featureless continuum over the factor of 4 in wavelength observed, from 1.25 to 4.8 μm, and also require an unreasonably high conversion efficiency of UV to infrared photons. Reflected light can be ruled out because the observed integrated nebular flux densities, at 2.2 μm in NGC 2023 and 2068, are larger than the dereddened 2.2 μm flux densities of the stars which illuminate the visual reflection nebulae; and because the 3.8 μm surface brightness observed in positions in all three nebulae is too large by factors of 2-30 to be explained by reflected light. The difference between the observed nebular colors and stellar colors of paper 2, as well as predictions (Appendix F) of the surface brightness due to faint stars, rule out undetected stars as significant contributors to the observed nebular emission. Free-free emission can be ruled out because of the low values of observed radio continuum emission in the nebulae.

b. A thermal fluctuation model

A number of authors (Duley 1973; Greenberg and Hong 1974; Harwit 1975; Allen and Robinson 1975; Purcell 1976) have suggested that the temperature of small grains may fluctuate strongly under interstellar heating conditions, due to their small heat capacity. This mechanism may offer a plausible explanation for the observed near infrared emission.

The heat capacity C_V of a grain is most often approximated by the Debye theory. In the applications previously considered, a typical grain in a dark cloud, whose equilibrium temperature of 10-15 K is determined by the interstellar radiation field, is briefly heated to much higher temperatures after absorption of a UV photon (Duley 1973; Greenberg and Hong 1974; Harwit 1975; Purcell 1976) or upon formation of a chemical bond between molecules on the grain surface (Allen and Robinson 1975). These authors found peak grain temperatures lower than the Debye temperatures of typical grain materials, 200-500 K (Allen and Robinson 1975), so that the low temperature approximation to the heat capacity, $C_V \propto T^3$, was appropriate. At the higher temperatures characteristic of the reflection nebulae observed here, $\sim$ 1000 K, the high temperature limit of the heat capacity must be used, $C_V = 3Nk$, where $3N$ is the number of degrees of freedom in the grain. The high temperature limit is a reasonable approximation as long as the temperature is higher than about one-fifth of the Debye temperature (Kittel 1969), and thus is appropriate even for materials with very high Debye temperatures, such as diamond with a Debye temperature of 2200 K. The value of N will range from the number of molecules in the grain lattice to the number of atoms in the grain lattice, depending on the degree to which the internal vibrational degrees of freedom of molecules in the grain are excited at $\sim$ 1000 K.

A number of processes may contribute to the excitation of the thermal fluctuations. Absorption of UV photons and chemical reactions between molecules on the grain surface have already been mentioned. Other possibilities are collisions between the grain and atoms, molecules, or other grains; cosmic rays; and runaway chemical reactions among molecules on the grain surface, or "chemical explosions" (Greenberg 1973; d'Hendecourt *et al.* 1982). The efficiency of any excitation process for the thermal fluctuations depends on both

the expected rate, R, of the heating events, and the energy, E, of the event available for grain heating. Table 1 shows the rates and energies derived for a number of possible processes, for reasonable assumptions about the physical conditions in the nebulae. Appendix B describes how these values of R and E were derived. Table 1 shows values derived both for a grain size of 10 Å, which will be seen to be the grain size of interest for the thermal fluctuation model, and for a typical interstellar size of 0.1 μm, to show the dependence of E and R on the grain size.

From the observed near infrared luminosity of the reflection nebulae one can derive a minimum rate required for the heating events, as is shown in Appendix C. This minimum rate is $7 \times 10^{-6} - 7 \times 10^{-8}$ s^{-1}, for the densities of $10^2 - 10^4$ cm^{-3} appropriate to the reflection nebulae. The rates of Table 1 are the largest possible for each process, and so one can immediately rule out all processes with $R < 7 \times 10^{-6} - 7 \times 10^{-8}$ s^{-1} as explanations of the observed near infrared emission. This leaves the processes of photon absorption, gas-grain collisions, and molecular bond formation on grain surfaces.

The most energetic of the processes which occur frequently enough to account for the emission are gas-grain collisions in shock fronts and the absorption of UV photons. Processes occurring in shock fronts can be ruled out, however, on the basis of the spatial distribution, since these hypothetical shocked regions, caused by mass loss from pre-main sequence stars, are confined to regions within 15" of the pre-main sequence star (Appendix B). In NGC 2023 near infrared emission is seen 3' north of the central star (Figure 2), while all the pre-main sequence stars found at 2.2 μm in this nebula are $\sim$ 1' south of the central star (paper 2). The model to be described, therefore, assumes UV photons excite the thermal fluctuations.

The high temperatures characteristic of the reflection nebulae, ~ 1000 K, imply very small grain sizes. The number of molecules is determined by comparing the energy of the heating event, taken here to be the photon energy E_{ph}, to the integral of the heat capacity over temperature. Since for T large, $C_V = 3Nk$, a rough estimate of this integral is $E_{ph} = 3Nk\Delta T$, where ΔT is the difference between maximum and minimum temperatures. Thus for E_{ph} = 10 eV and ΔT = 1000 K, N = 30 molecules. For a lattice spacing of ~ 3 Å this corresponds to a grain radius of ~ 10 Å. A more careful calculation, using the theory outlined by Allen and Robinson (1975), gives N = 70 and 90, and radii of 9 and 6 Å, for silicate and graphite grains respectively.

One of the major advantages of this model is that the surface brightness of the near infrared emission, if excited by UV radiation from the central star, is predicted to follow the distribution of stellar flux throughout the nebula. Since the visual surface brightness of reflected light also depends on the stellar flux at each point, this model naturally predicts the observed agreement between the surface brightness distributions at visual and near infrared wavelengths. Furthermore, since the peak temperature depends only on the grain size and the energy of the UV photon, the color temperature would be expected to be independent of distance from the central star, as observed.

It is of interest to estimate what the number of small grains required to explain the observations implies about the grain size distribution in the reflection nebulae. One way of investigating this question is to compare the observations with the grain size distribution of Mathis, Rumpl, and Nordsieck (1977, hereafter MRN). This grain size distribution, $n(a)da = n_0 a^{-3.5} da$, where a is the grain radius, extends over the range $a_+ > a > a_-$, where MRN adopted a_+ = 0.25 μm and a_- = 0.005 μm. Biermann and Harwit (1980) have proposed that the origin of this grain size distribution is grain-grain collisions in the regions, such

as red giant atmospheres, where grains form, and find that the $a^{-3.5}$ distribution should extend to grain radii as small as 10 Å. In Appendix D this grain size distribution, extended to smaller grain sizes than considered by MRN, is found to provide good agreement with the observations of reflection nebulae. The expected fraction x of the total dust mass in 10 Å sized grains, from the extension of the MRN distribution, is $x = 2 \times 10^{-3}$. Appendix C shows that the fractional dust mass required by the observations, for a photon rate of 2×10^{-4} s^{-1} (Table 1; Appendix B) and a hydrogen density of 10^3 cm^{-3}, is $x = 3 \times 10^{-3}$. The fraction of the stellar luminosity absorbed by 10 Å sized grains and reradiated in the near infrared, compared to the total stellar luminosity absorbed by dust and reradiated at all infrared wavelengths, is observed to be $\sim 10^{-2}$. The value expected for a MRN distribution, extended to smaller grain sizes, is found in Appendix D to be $\sim 4 \times 10^{-3}$. The good agreement of the number of grains required to explain the near infrared emission with the number expected from a MRN size distribution is encouraging and demonstrates that quite reasonable numbers of small grains are required to account for the observations.

An obvious concern when grain sizes this small are involved is whether heat capacities and optical constants measured for bulk materials will apply to grains of this size. Martin (1973) finds that calculations of the heat capacity and absorption coefficients of ionic crystals containing 64 atoms differ very little from calculations for infinite crystals. Similarly, Kreibig (1974) finds that bulk optical constants for metals need only minor modifications to provide agreement with measurements of metal particles containing as few as 50 atoms. The differences between the small particle and bulk heat capacities are much smaller than the uncertainties in the calculations of this paper due to the use of the Debye approximation or due to the unknown composition of the grains. The

differences in the optical constants also are not important for the calculations of this paper, but may eventually imply interesting effects in the spectra of these grains, such as the increasing importance of surface phonon modes at far infrared wavelengths.

c. Implications

The model described in section IVb, while not unique, does explain many of the observed features of the near infrared emission of these three visual reflection nebulae. The grain sizes required to explain peak temperatures ~ 1000 K are uncomfortably small, $a \sim 10$ Å, but the numbers of these grains required are consistent with the extrapolation of the MRN grain size distribution to smaller grain sizes.

It seems likely that the observed near infrared emission exists in other regions, but has not been detected previously due to the small fraction, $\sim 10^{-2}$, of the total luminosity involved. This small contribution is easily masked by other near infrared emission mechanisms. If the emission is excited by UV photons, then it should be found only near O and B stars, the hotter of which have substantial H II regions which have associated free-free emission as well as equilibrium thermal emission from dust heated by trapped L α radiation. Most cooler stars probably produce too few UV photons to produce observable amounts of the near infrared emission. The reflection nebulae observed were originally selected for having the most luminous central stars possible without having significant H II regions, as well as having modest amounts of dust. Thus these sources represent a special set of physical conditions where the amount of UV radiation is sufficient to produce observable near infrared emission from the thermally fluctuating small grains, yet insufficient to ionize an H II region which masks the near infrared emission.

One feature of the proposed 10 Å sized grains is that they are difficult to detect except through their thermal fluctuations. They represent only a small fraction of the total dust mass. Similarly, they contribute little to the extinction at visual and ultraviolet wavelengths. This is because grains absorb efficiently only at wavelengths comparable to and shorter than $2\pi a$ (Appendix D), i.e., for a = 10 Å, the wavelength of soft X-rays, a wavelength region where processes other than grain extinction dominate the absorption.

The constancy of the 3.3 μm feature-to-continuum ratio in the three visual reflection nebulae (paper 1) suggests that the feature is associated with the continuum. One possible explanation is that the 3.3 μm feature is due to fluorescence (Allamandola, Greenberg, and Norman 1979), so that both the feature emission and the continuum emission from the thermally fluctuating grains is proportional to the incident UV stellar flux. The similarity of α_{UV}, the required conversion efficiency of UV photons to 3.3 μm feature photons, in the reflection nebulae to the values of α_{UV} found in other sources (Dwek *et al.* 1980) where the fluorescence model fails, however, argues against this explanation. Another possibility is that the 3.3 μm feature, as well as the continuum, is due to thermal emission from thermally fluctuating grains. Sellgren (1981) has argued that the 3.3 μm emission in the Orion nebula arises in the H II region-molecular cloud interface, and that the 3.3 μm emitting material is destroyed when heated to high temperatures in the vicinity of the Trapezium. This suggests the 3.3 μm emitting grains in the reflection nebulae may be somewhat larger grains (~ 15 Å) than those producing the 3 μm continuum, with correspondingly lower peak temperatures (~ 300 K). In sources where the equilibrium grain temperatures are high enough to produce the observed 3.3 μm emission, such as Orion, the 3.3 μm feature would arise mainly from grains with a ~ 50 Å, as proposed by Dwek *et al.* (1980), since the smaller grains (a ~ 10-15 Å) absorb a smaller fraction of

the heating radiation.

While the 3.3 μm emitting material may be volatile, the grains producing the near infrared continuum emission by thermal fluctuations must be relatively refractory. The time scale for two UV photons being absorbed by a small grain, close enough in time to raise the peak temperature to twice the peak temperature caused by a single UV photon, is $\sim 10^2$ yr. Thus the thermal fluctuation model requires that the continuum emitting grains survive occasional heating to $\sim$ 2000 K. The rate of absorption of three UV photons simultaneously is negligibly small.

V. SUMMARY

The observations presented in this paper and in paper 1 show the following results:

1. Near infrared emission is found in three visual reflection nebulae, extended over 0.4-0.9 pc. The emission in NGC 7023 and 2023 peaks near the visual illuminating star and falls off with projected distance from the central star. The emission in NGC 2068 has no strong peak and has approximately constant surface brightness across the nebula.

2. The energy distribution of each nebula shows no evidence for any dependence on position in the nebula or offset from the central star. The spectra of the three nebulae are very similar.

3. The spectrum with 1-5 % resolution of the nebulae consists of a smooth continuum from 1.5 to 3.7 μm, except for emission features at 3.3 and 3.4 μm. The continuum from 1.25 to 4.8 μm can be characterized by a color temperature of $\sim$ 1000 K. The feature-to-continuum ratio of the 3.3 μm emission feature is 6.

4. The spatial distribution of near infrared surface brightness in NGC 7023 and NGC 2023 agrees extremely well with that of visual reflected light.

The following model may be able to account for the observations:

1. Thermal emission from very small grains undergoing thermal fluctuations could explain the high observed color temperatures. These small grains have low heat capacities, so that they momentarily reach high temperatures after being excited by absorption of UV photons, chemical reactions on their surface, or collisions.

2. The most efficient excitation mechanism, in terms of frequency of occurrence and available heating energy, is absorption of UV photons.

3. The required number of molecules in the grain, to reach a color temperature of 1000 K after absorption of a 10 eV photon, is ~ 70-90 molecules. This corresponds to a grain radius of ~ 10 Å.

4. This mechanism naturally explains the good agreement of near infrared and visual surface brightness distributions, since both the rate of excitation of the thermal fluctations and the visual reflected light depend directly on the incident stellar flux. Furthermore, the peak grain temperature attained is predicted to be independent of distance from the star, in agreement with the observed constancy of the color temperature throughout these nebulae.

5. The mass of grains required is a small fraction, ~ 10^{-3}, of the total mass of grains, and is consistent with an extrapolation of the grain size distribution of Mathis, Rumpl, and Nordsieck (1977) to smaller grain sizes. The ratio of the near infrared to total infrared luminosities observed is also consistent with the ratio of UV absorption cross sections predicted for this grain size distribution.

Acknowledgements

I thank the staff of Mt. Wilson Observatory for their hospitality during my interminable observing runs; my night assistants at Mt. Wilson Observatory, J. Frazer and H. Lanning; and my telescope operators at the Infrared Telescope Facility, C. Kaminski and D. Griep. Additional assistance with observations was provided by G. Berriman, R. Capps, H. L. Dinerstein, J. H. Lacy, M. Malkan, Y. Pendleton, A. Rosenthal, B. T. Soifer, M. W. Werner, S. E. Whitcomb, and R. L. White. I especially thank S. E. Whitcomb, who collaborated on the 2.2 μm observations of NGC 7023. I thank the Infrared Telescope Facility for providing their RC-2 InSb system; E. Erickson for the loan of a 2–4 μm circular variable

filter wheel; G. Neugebauer for the use of, and K. Matthews for the construction and maintenance of, Caltech infrared group equipment; and A. N. Witt and A. Sargent for communicating results prior to publication. Useful conversations were held with S. E. Whitcomb, R. L. White, M. Jura, M. W. Werner, A. N. Witt, L. Allamandola, F. Baas, H. L. Dinerstein, B. T. Soifer, and G. Neugebauer. This research was supported by NASA and NSF.

APPENDIX A

The following mechanisms can be ruled out as explanations of the observed near infrared continuum emission:

1) Equilibrium thermal emission. The lack of a radial dependence of the shape of the nebular energy distribution provides a stringent observational constraint on explaining the continuum emission by thermal emission from dust in equilibrium with the radiation field of the central star. In Figure 11 the ratio of the 3.8 and 2.2 μm surface brightnesses, from paper 1, is plotted *vs.* the stellar flux incident on a grain. The ratio of 3.8 to 2.2 μm surface brightnesses is seen to be independent of incident stellar flux in the three nebulae, and of projected radial distance within each nebula. For comparison, Figure 11 also shows the dependence on incident stellar flux of the ratio of 3.8 to 2.2 μm flux densities for thermal emission from a dust grain with an infrared emissivity proportional to the frequency ν. This emissivity would imply $T_d \propto (L_*/4\pi r^2)^{1/5}$, and a surface brightness $S_\nu \propto \nu B_\nu(T_d)$. Here T_d is the grain temperature, L_* is the total stellar luminosity, r is the distance of the grain from the star, and $B_\nu(T_d)$ is the Planck function. Figure 11 shows that the 3.8 to 2.2 μm flux density ratio, which has been fit through the observations at an incident stellar flux of $L_*/4\pi r^2 \sim 10$ erg cm^{-2} s^{-1}, should decrease a factor of 2.2 for the range of a factor of 4 in the incident stellar flux shown. In contrast, the observed ratio is constant and clearly independent of stellar flux.

The observed constancy of the surface brightness ratios (Figure 8; Figure 11), or color temperature, with offset from the central star requires either that the grains are at a distance from the star along the line of sight which is large compared to the extent of the nebula on the sky, so that grains at different offsets on the sky are equidistant from the star, or requires that the grains are sublimating. Sublimation, while holding the grain temperature constant, would

destroy grains at a rapid rate and likely create holes in the dust density near the star, for which no evidence is seen. The flatness of the surface brightness distribution in NGC 2068 might suggest a geometry, in this particular source, in which the dust is equidistant from the star. The surface brightness distributions of NGC 7023 and 2023, in contrast, are strongly centrally peaked. This would require that the dust, if contained in a sheet which is distant from the central star, have a column density which fortuitously peaks along the line of sight to the central star and falls off with projected distance on the sky. This geometry, while not ruled out, seems unlikely.

An even more severe difficulty with thermal emission from dust in equilibrium with the stellar radiation field, as an explanation of the near infrared continuum emission, is the observed high value of the color temperature. This color temperature, ~ 1000 K, is much higher than the dust temperatures achieved by grains with generally accepted compositions. A grain which is in equilibrium with the radiation field of a nearby star has a temperature T_d determined by:

$$\int \frac{\pi a^2 L_*(\nu)\, Q_{abs}(\nu)\, d\nu}{4\pi r^2} = \int 4\pi a^2\, Q_{abs}(\nu)\, \pi B_\nu(T_d)\, d\nu\,, \qquad (1)$$

where $L_*(\nu)$ is the stellar luminosity at frequency ν, r is the distance of the dust grain from the star, a is the grain radius, and $Q_{abs}(\nu)$ is the grain absorption efficiency at frequency ν. One can then introduce the Planck averaged emissivities Q_{UV} and Q_{IR}, defined by

$$\frac{\pi a^2 L_*\, Q_{UV}}{4\pi r^2} = \int 4\pi a^2\, Q_{abs}(\nu)\, \pi B_\nu(T_d)\, d\nu = 4\pi a^2\, Q_{IR}\, \sigma T_d{}^4\,, \qquad (2)$$

where σ is the Stefan-Boltzmann constant. Generally Q_{IR} depends both on T_d and a. Draine (1981), for example, finds $Q_{IR} = 6.7 \times 10^{-4}\, aT_d$ (a in microns) for

amorphous carbon, while Dwek *et al.* (1980) adopt $Q_{IR} = 1.7 \times 10^{-3}\ aT_d$ and $3.6 \times 10^{-6}\ a^2T_d^2$ (a in microns) as approximations for grains with emissivities proportional to ν and ν^2 respectively.

For the observed nebulae $L_* \sim 10^4\ L_\odot$, and $r \sim 4 \times 10^{17}$ cm (corresponding to 1' at the distances of these sources). If the grain size is big compared with the wavelength where most of the stellar luminosity is emitted, then $Q_{UV} \sim 1$. In this case, for the above emissivities, $T_d \sim 30 - 40\ a^{-1/5}$ for $Q_{IR} \propto aT_d$, or $T_d \sim 50\ a^{-1/3}$ for $Q_{IR} \propto (aT_d)^2$. Here a is in microns. At sufficiently small grain sizes, Q_{UV} is no longer ~ 1. In this case one might expect $Q_{UV} \sim 6.7 \times 10^{-4} - 1.7 \times 10^{-3}\ aT_*$, or $Q_{UV} \sim 3.6 \times 10^{-6}\ a^2T_*^2$, to approximately hold, where the stellar temperature, T_*, is $\sim$ 20000 K. In this limit of small grain size the grain temperature reaches a maximum value which is independent of a. This maximum value is $T_d \sim 70 - 180$ K.

The predicted grain temperatures above, $T_d \lesssim 180$ K, are much less than the color temperature of the near infrared emission, $\sim$ 1000 K. Calculations based on other emissivities (Jewitt 1982) than those of Draine (1981) and Dwek *et al.* (1980) do not yield predicted grain temperatures significantly higher than 70 - 180 K. The low predicted grain temperatures for grain materials generally considered by other authors, compared to the high color temperature of the near infrared emission, is the most powerful argument against an equilibrium thermal emission model. From eq. 2, with $T_d = 1000$ K, one sees that to satisfy the observations a material would need to have $Q_{IR}/Q_{UV} \sim 10^{-7}$. Since none of the popularly considered candidate grain materials have such low values of Q_{IR}/Q_{UV}, and since this mechanism encounters additional difficulties with explaining the observed spatial distribution, it does not seem likely that equilibrium thermal emission can explain the observations of reflection nebulae.

2) Fluorescence. The most appealing feature of fluorescence is its ability to explain the good agreement of the spatial distributions of the near infrared emission and visual reflected light. If the fluorescence is excited by ultraviolet photons from the central star, then the emission should follow the distribution of stellar flux through the nebula, which is approximately traced by the visual scattered light. A fluorescent mechanism suggested by Allamandola, Greenberg, and Norman (1979) as a possible explanation for the 3.3 μm emission feature involves molecules frozen on grain mantles. The mantle molecules absorb ultraviolet photons and, due to their poor coupling to the phonon modes of the grain core, radiate their energy in vibrational lines rather than transmitting thermal energy to the rest of the grain. This mechanism, however, like fluorescence in gas phase molecules, produces only discrete lines. The spectrum of the near infrared emission, aside from the 3.3 and 3.4 μm features, appears to consist of a continuum at resolutions of 1-5 %, which is difficult to explain as a series of lines produced by fluorescence. Molecular hydrogen, which can be excited by ultraviolet photons into fluorescent emission in the infrared, does produce large enough numbers of lines that its infrared spectrum appears continuous with resolutions of 1-5 % (Black and Dalgarno 1976). The predicted spectrum of Black and Dalgarno, however, shows large fluctuations of relative intensity between different resolution elements, due to the varying strengths of individual lines of the fluorescence spectrum. Any substance, whether in the solid or gas phase, which gives rise to fluorescence in the infrared will be expected to have a spectrum which fluctuates strongly as a function of wavelength, particularly as the resolution increases from 5 % to 1 %. The smoothness of the nebular spectrum at resolutions of 1 and 5 % from 1.5 to 3.7 μm, and the flatness, in units of flux per unit frequency, of the energy distribution from 1.25 to 4.8 μm, most probably rule out fluorescent

mechanisms as explanations for the observed near infrared continuum emission.

A final objection to UV excited fluorescence as an explanation of the near infrared continuum emission is that the required values of α_{UV}, the conversion efficiency for UV to infrared photons, are too high. Following Dwek *et al.* (1980), α_{UV} is calculated by assuming all of the stellar luminosity absorbed by grains, taken to be the observed far infrared luminosity of the nebula, is absorbed as 10 eV photons, of which a fraction α_{UV} are converted to infrared fluorescent photons. The values for α_{UV} for the three reflection nebulae, including the continuum from 1.25 to 4.8 μm but excluding the 3.3 and 3.4 μm emission features, range from α_{UV} = 0.1 to 0.7. These values are considerably higher than expected fluorescence efficiencies (Dwek *et al.* 1980), and therefore argue against fluorescence as an explantion of the observed continuum emission.

3) Reflected light. Reflected light might appear to be the most natural explanation for the extended near infrared emission, because the visual emission is known to be reflection nebulosity. Two problems immediately arise with this interpretation. One is the color of the nebulosity compared to the color of the illuminating stars. Reflection nebulae should be similar in color to or somewhat bluer than their illuminating stars. NGC 2023 and 2068 in contrast have energy distributions in the near infrared markedly different from, and much redder than, the Rayleigh-Jeans energy distributions of the central stars. HD 200775 has an identified circumstellar infrared excess, hence NGC 7023 and its central star have similar near infrared colors. The similarity of the energy distributions in the three nebulae, however, argues that all three have the same emission mechanism. The second problem with interpreting the nebular emission as near infrared reflection nebulosity is the integrated flux densities of the nebulae compared to those of the central stars. At 3.8 μm the total flux densities of NGC 7023, 2023, and 2068 are 4.4, 13, and 13 Jy respectively (cf.

Figure 9), while the 3.8 μm flux densities of the central stars are 12, 0.33, and 0.49 Jy respectively. If there is little reddening of the illuminating star of a reflection nebula, as would be the case for these stars in the infrared, then the flux density of the nebula should be less than that of the star. The fact that the nebular flux densities range from comparable with, to much greater than, the stellar flux densities is a severe problem for a reflected light hypothesis.

This problem with the nebular brightness can be quantified using a comparison of the observed nebular surface brightness with the maximum surface brightness possible for reflected light. The maximum surface brightness S_{max} of a reflection nebula, derived in Appendix E, is $S_{max} = \tau F_* (4\pi\varphi^2)^{-1}$ for optically thin ($\tau < 1$) nebulae and $S_{max} = F_* (4\pi\varphi^2)^{-1}$ for optically thick ($\tau > 1$) nebulae. Here τ is the total extinction optical depth through the nebula, φ is the angular offset on the sky from the illuminating star of the observed nebular position, and F_* is the dereddened flux density of the illuminating star. In Appendix F the value of the total nebular optical depth at 2.2 μm is estimated to be 0.4, 4, and 2 for NGC 7023, 2023, and 2068 from ^{13}CO measurements. The corresponding values of the 3.8 μm optical depth are 0.2, 2, and 1 if the extinction between 2.2 and 3.8 μm is proportional to λ^{-1}. Dereddening the central stars with a typical extinction curve (Johnson 1968) and comparing the observed surface brightness S_{obs} to the derived value of S_{max} leads to ratios of S_{obs}/S_{max} at 2.2 μm, averaged over the nebula, of ~ 0.5, 6, and 3 for NGC 7023, 2023, and 2068 respectively. At the positions observed at 3.8 μm the typical ratios of S_{obs}/S_{max} are ~ 2, 30, and 10 in NGC 7023, 2023, and 2068 respectively. Thus the near infrared surface brightnesses of these 3 nebulae are much brighter than can be explained by reflected light. Since S_{max} is derived by adopting grain parameters and a nebular geometry which maximize the surface brightness of reflection nebulae, conditions which in general will not prevail, the

actual contribution of reflected light to the observed nebular emission is likely to be considerably smaller than the upper limit of 3-50 % at 3.8 μm suggested by the value of S_{max}/S_{obs}.

A possible solution to the inability of the illuminating stars of the visual reflection nebulae to account for the observed near infrared surface brightness is to hypothesize illumination by a different star. The radio observations (Sellgren *et al.* 1983c) and far infrared observations (Whitcomb *et al.* 1981; Emerson, Furniss, and Jennings 1975; Harvey, Thronson, and Gatley 1980; Sargent 1982) of these nebulae find no evidence for any additional sources of ionizing photons or luminosity in these regions. A T Tauri star could be brighter than the central star at near infrared wavelengths while contributing little luminosity and no ionizing photons. The stars found in 2.2 μm scans of these regions (paper 2), many of which are T Tauri stars, are unable to produce enough reflected light to account for the observed emission. A T Tauri star could be hidden in these regions by extinction which obscures the star along the observer's line of sight only, while allowing it to still illuminate reflection nebulosity. This would require, however, the unlikely coincidence of all three nebulae having hidden stars illuminating infrared reflection nebulosity, with positions on the sky very close to the stars which illuminate visual reflection nebulosity in order to account for the positions of peak infrared surface brightness.

While reflected light can be ruled out as the explanation of the observed near infrared emission, reflected light still can contribute some small amount to the observed emission, particularly in NGC 7023 at the shorter wavelengths. The detection of a small but finite amount of 2.2 μm polarization in NGC 7023, with the same polarization position angles as are found for visual reflected light (Sellgren *et al.* 1983b), supports this possibility. This reflected light

contribution, while interesting, is small enough that all three nebulae can be considered together in striving to understand the source of the near infrared emission.

4) Stars. NGC 7023, 2023, and 2068 have associated with them clusters of young stars (paper 2). The emission from the stars already discovered in 2.2 μm scans has already been subtracted from all the observations presented here. There presumably are, however, stars present in the clusters with magnitudes fainter than the detection limits of the 2.2 μm scans. In Appendix F the luminosity function derived for the cluster stars (paper 2) is used to estimate the integrated 2.2 μm flux density of these fainter stars. These estimates are $\sim$ 10 % of the observed 2.2 μm flux densities of the reflection nebulae. The observed colors of the stars (paper 2) and nebulae can be used to predict the fraction of the observed flux densities at wavelengths other than 2.2 μm which are due to faint cluster stars. This implies $\lesssim$ 20 % of the emission at other wavelengths can be due to stars. Further arguments against any significant contribution due to stars are the smoothness of the surface brightness distributions (Figures 1 and 2), the constant value of the surface brightness in diaphragms of 6" to 60" (paper 1), and most importantly, the marked difference between the stellar colors and nebular colors (Figure 7). It seems unlikely that the faint cluster stars, even if they were smoothly distributed on the sky in numbers much larger than predicted from a luminosity function, would have colors that differ so strongly from the colors of the brighter stars.

5) Free-free emission. Free-free emission, while having a near infrared spectrum similar to that observed for the continua of the reflection nebulae, is unable to produce enough near infrared surface brightness to account for the observed 2.2 μm emission. The optically thin free-free emission observed at 6 cm in NGC 2023, 30 mJy, and in NGC 2068, 60 mJy (Sellgren *et al.* 1983c), can

account for only ~ 0.1-0.2 % of the 2.2 μm flux densities of these sources. The upper limit of 10 mJy on 6 cm emission from NGC 7023 (Haslam *et al.* 1978) implies a similarly small contribution to the total 2.2 μm flux density of this source.

Free-free emission which is optically thick at radio wavlengths could explain the near infrared emission only if it were due to many (~ 10^3) small (< 6×10^{14} cm diameter), dense (> 4×10^7 cm^{-3}) clumps of ionized gas. These clumps, however, would expand freely at the sound speed, ~ 10 km s^{-1}, and so only survive $\lesssim$ 2 yr. The upper limit on B γ in the spectra of NGC 7023 and NGC 2023 (Figure 5), which is < 5% of the strength B γ would have if the 2 μm continuum were due to optically thin free-free emission, would require that the optical depth be high not only for free-free emission at 6 cm but also high in the B γ line. This would in turn imply even more extreme limits on the size and density of clumps of ionized gas required to explain the extended near infrared continuum emission as free-free emission.

APPENDIX B

The efficiency of any given heating process in a grain depends both on its expected rate, R, and its energy available for grain heating, E. Table 1 summarizes the rates and energies of a number of different heating processes. In this table R and E are given for both small (10 Å) and large (0.1 μm) grains. To heat a grain containing N atoms to $T \sim 1000$ K requires $E \sim 3NkT$, or $E \sim 10$ eV for 10 Å sized grains and $E \sim 1 \times 10^7$ eV for 0.1 μm sized grains. The following describes the method by which R and E are derived for each process; in general Table 1 gives the maximum possible value of R.

The physical conditions in each reflection nebula are characterized by three regions. The first is the H II region, which has an electron temperature $\sim 10^4$ K, an electron density $\sim 10^2$ cm^{-3}, and a radius $\sim 4 \times 10^{17}$ cm (Sellgren *et al.* 1983c). A second region is the molecular cloud, which contains not only CO but C II, and has a total hydrogen density $\sim 10^4$ cm^{-3}, an electron density ~ 2 cm^{-3}, and a gas temperature ~ 20 K (Brown *et al.* 1975; Knapp, Brown, and Kuiper 1975; Pankonin and Walmsley 1976, 1978). The distance from the star considered in the molecular cloud is also 4×10^{17} cm. A third region is a shock front, the possible existence of which is suggested by the presence of pre-main sequence stars (paper 2), which may have stellar winds, in these nebulae. While no direct observational evidence exists for shocks in these reflection nebulae, shocks still may be present at levels which have escaped detection yet may be important for grain heating. Low mass pre-main sequence stars undergoing mass loss are observed to have mass loss rates $\dot{M} \sim 10^{-8}\ M_\odot$ yr^{-1} and outflow velocities of $v_{sh} \sim 100$ km s^{-1} (Felli *et al.* 1982). The parameters implied therefore for this hypothetical shocked region are a temperature of the postshock gas of 2×10^5 K (Cowie 1978), and a radius of the shocked region around the star undergoing mass loss of $r = 1 \times 10^{17}$ cm. The radius is

determined by the balance between the thermal pressure nkT of the surrounding material and the ram pressure $\dot{M}v_{sh}/4\pi r^2$ of the stellar wind, and has similar values for the H II region and molecular cloud, for the the values of the density n and temperature T taken above. These three distinct regions, which are representative of conditions observed in NGC 7023, 2023, and 2068, are considered individually in the calculations of possible grain heating processes.

1. Photon absorption. The rate at which photons are absorbed by a grain at a distance r from a star is $L_*(\nu)\Delta\nu Q_{abs}\sigma_d/4\pi r^2 h\nu$, where $L_*(\nu)$ is the luminosity per unit frequency of the star at frequency ν, $\Delta\nu$ is the frequency bandwidth over which the photons are absorbed, Q_{abs} is an absorption efficiency for the grain, and $\sigma_d = \pi a^2$ where a is the grain radius. The absorption efficiency adopted is $Q_{abs} = 2\pi a/\lambda$ for $\lambda > 2\pi a$, and $Q_{abs} = 1$ for $\lambda < 2\pi a$, where λ is the wavelength of the stellar photon. For simplicity stellar photons of a single energy are considered, namely those between wavelengths of 900 and 1100 Å, or a photon energy $E_{ph} \sim 12$ eV. The model atmospheres of Kurucz (1979) have been used to derive 900-1100 Å photon fluxes for the central stars of the reflection nebulae, which give a typical value of $L_*(\nu)\Delta\nu/h\nu = 2 \times 10^{47}$ photons s^{-1}. The distance r is taken as 4×10^{17} cm. Extinction between the star and grain has been ignored. The photon energy is assumed to be entirely transferred to grain heating.

2. Gas-grain collisions (H II region). Collisions between grains and electrons are the most frequent gas-grain collision process in the H II region. While radiation pressure from the central star will accelerate the grain, there is also a plasma drag force on the grain, which is collisionally or photoelectrically charged (Spitzer 1978). This drag force results in a grain velocity which is less than the thermal velocity of hydrogen atoms or electrons. The energy of the

collision is therefore kT_e, where T_e, the electron temperature, is $\sim 10^4$ K. Assuming a sticking probability of 1, then all of the kinetic energy of the collision is available for grain heating. The collision rate is $n_e \sigma_d v_e$, where n_e is the electron density, $\sim 10^2$ cm^{-3}, and v_e is the thermal velocity of the electrons.

3. Gas-grain collisions (molecular cloud). Collisions between hydrogen atoms and grains within the molecular cloud are governed by a rate equal to $n_H \sigma_d v_d$, where n_H is the number density of hydrogen (atomic or molecular), and v_d is the velocity of the dust grain. The balance between radiation pressure from the central star and the drag force due to collisions of the grain with gas atoms and molecules results in a grain velocity $v_d = t_s w_a^2 / 2r$, where t_s is the slowing down time due to collisional drag, and w_a is the velocity the grain would have, due to radiation pressure, if there were no drag force (Spitzer 1978). If the grain velocity is larger than the gas velocity, then $t_s = 4\rho a / 3 n_H m_H v_d$, where ρ is the density of the grain, taken to be 2 g cm^{-3}, and m_H is the mass of the hydrogen atom. The quantity w_a is given by $w_a^2 = 3 L_* Q_p / 8\pi c r a \rho$, where L_* is the luminosity of the star, taken to be 10^4 $L_\odot$, Q_p is the grain efficiency for radiation pressure, taken equal to Q_{abs} at the peak of the stellar energy distribution ($\lambda \sim 0.15$ μm), and c is the speed of light. A typical density within the molecular cloud is $n_H = 10^4$ cm^{-3}. Again extinction between the star and grain is ignored. For the parameters adopted, $v_d = 2$ km s^{-1} for $a = 0.1$ μm and $v_d = 0.4$ km s^{-1} for $a = 10$ Å. The kinetic energy of atoms hitting the grain is low, $\lesssim 2 \times 10^{-2}$ eV for hydrogen, but Allen and Robinson (1975) argue that the adsorption energy E_{ads} of the atom onto the grain also goes into heating the grain. For physical adsorption $E_{ads} \sim 0.1$ eV. Again a sticking probability of 1 is adopted. The grain velocity would be lower if photoelectric charging of the grain were considered, due to plasma drag from ionized carbon in the C II region. The parameters for photoelectric charging are uncertain, however. Since Table 1

gives the maximum values of R and E, the value of v_d determined by collisional drag has been used.

4. Bond formation (molecular cloud). Another possible heating process, discussed by Allen and Robinson (1975) in detail, is formation of bonds between atoms or molecules adsorbed on the grain surface. They argue that usually the energy of formation, E_{bond}, is transferred to heating the grain rather than to ejecting the newly formed molecule. Typically $E_{bond} \sim 5$ eV (Allen and Robinson 1977). The rate of formation is derived by assuming every second collision of an atom with the grain results in a new bond, or $R = \frac{1}{2} n_{mol} \sigma_d v_d$, where n_{mol} is the number density of atoms or molecules colliding with the grain. Earlier a maximum value of $v_d = 0.4 - 2$ km s^{-1} was found. The rates given in Table 1 are the rates found by considering molecular hydrogen formation, or $n_{mol} = n_H = 10^4$ cm^{-3}. If instead only reactions between hydrogen and heavier atoms and molecules were considered, or reactions only between heavier species, the rates would be lower by n_{mol}/n_H, or by $\sim 3 \times 10^{-4}$ for carbon.

5. Gas-grain collisions (shock front). The effective rate of gas-grain collisions in the shocked region is the collision rate $n_e \sigma_d v_e$ times the ratio of volumes of shocked and unshocked material. The volume of the shocked material V_{sh} is $4\pi r_{sh}^2 \lambda_c$, where $r_{sh} = 1 \times 10^{17}$ cm is the radius of the shocked region and λ_c is the cooling length. The cooling length is $\lambda_c = kT_e v_{sh}/n_e \Lambda$, where v_{sh} is the shock velocity, 100 km s^{-1}, and Λ is the cooling function. For $T_e = 2 \times 10^5$ K, $\Lambda \sim 8 \times 10^{-22}$ erg cm^3 s^{-1} (Dalgarno and McCray 1972). The volume of the unshocked material V_{neb} is $4\pi r_{neb}^3/3$, where a minimum nebular radius of $r_{neb} = 4 \times 10^{17}$ cm is taken. Note that R is independent of the density of the postshock gas. The energy of gas-grain collisions in the shocked region is kT_e, since the electron velocity is higher than the grain velocity.

6. Grain-grain collisions (molecular cloud). The rate of grain-grain collisions is $n_d \sigma_d v_d$, where n_d is the number density of dust grains. The value of n_d depends on the grain size distribution, which is assumed here to be the grain size distribution of MRN, $n(a)da = n_0 a^{-3.5} da$. The value of n_0 is determined by requiring

$$\int_{a_-}^{a_+} \frac{4\pi\rho a^3}{3} n(a)da = \beta\, n_H m_H,$$

where $\beta = 10^{-2}$ is the dust-to-gas mass ratio. Values for a_+ and a_- of 0.25 μm and 0 respectively were taken (cf. Appendix D). The highest collision rate, for both large (a = 0.1 μm) and small grains (a = 10 Å), is for collisions with the small grains. Collisions with the large grains are more energetic but less frequent. The value of n_d assumed is therefore $n(a)da$, with $da = a$ = 10 Å. The kinetic energy of a collision available for heating a grain is $\frac{1}{2}\xi m_d v_d^2$, where m_d is the mass of the 10 Å radius grain, and ξ is the fraction of the kinetic energy of the collision which is transfered to heating the grain. The value of ξ is likely considerably less than 1. As before in the molecular cloud, $n_H = 10^4$ cm^{-3} and a maximum value of v_d = 0.4 - 2 km s^{-1} is used.

7. Grain-grain collisions (H II region). The rate of grain-grain collisions in the H II region is $n_d \sigma_d v_d$, as in the molecular cloud, with the main difference being that v_d is determined by plasma drag rather than collisional drag. The grain velocity is less than the ion velocity, and so the slowing down time due to plasma drag is (Spitzer 1978)

$$t_s = \frac{(2\pi)^{1/2}\rho a^3 (kT_e)^{3/2}}{2\, m_H^{1/2}\, n_e Z_d^2 Z_H^2 e^4 \ln\Lambda_D}$$

where Z_H = +1 is the proton charge, and Z_d is the grain charge. In the H II region $T_e = 10^4$ K and $n_e = 10^2$ cm^{-3}. The Debye shielding factor Λ_D =

$(3/2e^3)\,(k^3T_e^3/\pi n_e)^{1/2}$. The grain velocity is $v_d = t_s w_a^2/2r$. If only charging due to collisions is considered, then $Z_d = aykT_e/e^2$, where y is determined by $e^y = (m_e/m_H)^{1/2}(1-yZ_H)$. Here m_e is the electron mass, and $y = eU/kT_e$, where eU is the grain potential (Spitzer 1978). This results in a grain velocity ~ 0.3 km s^{-1} for $a = 0.1$ μm. For $a = 10$ Å, the grain velocity determined by the balance between radiation pressure and plasma drag is less than the random velocity acquired by collisions with the gas. Thus for $a = 10$ Å, $v_d = (2kT_e/m_d)^{1/2} = 0.2$ km s^{-1}. Again the heating energy is less than the kinetic energy of the collisions by an unknown fraction ξ. Including photoelectric grain charging increases Z_d and decreases v_d for $a = 0.1$ μm, giving lower values of R and E than those in Table 1.

8. Grain-grain collisions (shock front). The effective rate of grain-grain collisions in the shocked region is the grain-grain collision rate found before, weighted by the ratio of the shocked and unshocked volumes, or $R = n_d \sigma_d v_d V_{sh}/V_{nsb}$. The grains enter the shocked region with a velocity $v_d = 3/4\ v_{sh}$ (Cowie 1978), where $v_{sh} = 100$ km s^{-1}, and are then slowed down by plasma drag to velocities more typical of unshocked regions. Grain acceleration in the postshock region by compression of the magnetic field appears to be unimportant for the densities considered here (Shull 1978). Thus the shocked volume of interest is $V_{sh} = 4\pi r_{sh}^2 t_s v_d$, where t_s is the slowing down time for plasma drag, and $v_d = 3/4\ v_{sh}$. The smaller grains are slowed down faster, since t_s is proportional to a, but the collision rate is much higher for the smaller grains, so that t_s is calculated for $a = 10$ Å. As before, $r_{sh} = 1 \times 10^{17}$ cm, and $V_{nsb} = 4\pi r_{nsb}^3/3$ with $r_{nsb} = 4 \times 10^{17}$ cm. The grain charge is determined by collisional charging in the shocked region; formulae for Z_d in this case and for t_s when the electron velocity exceeds the grain velocity are given above. The heating energies of the grain-grain collisions are again $\frac{1}{2}\xi m_d v_d^2$, and the rates

are again independent of n_H.

9. Cosmic rays. The main way in which a cosmic ray deposits energy in a grain is by ionization energy loss. The loss rate is dE/dx, and so the total energy deposited in the grain is $2a\ dE/dx$, which is assumed to be transferred to grain heating. The collision rate is $4\pi\varphi\Delta E\sigma_d$, where φ is the cosmic ray flux, and ΔE is the range of cosmic ray energies. The values adopted here are those adopted by Leger, Omont, and Jura (1983):

$$\begin{aligned} dE/dx &= 5Z^2(1+0.15/E) && E > 0.1 \\ \varphi_H(E) &= 0.3E^{-1} && 0.2 < E < 1 \\ \varphi_H(E) &= 0.3E^{-2} && E > 1 \end{aligned}$$

where the energy loss rate dE/dx is given in units of MeV/cm, E is the cosmic ray energy in GeV/nucleon, and φ_H is the cosmic ray flux for protons (H) in units of cosmic rays $cm^{-2}\ s^{-1}\ sr^{-1}\ GeV^{-1}$. Leger, Omont, and Jura also adopt a cosmic ray flux for iron nuclei (Fe) of $\varphi_{Fe} = 2 \times 10^{-4}\ \varphi_H$. The atomic number Z is 1 for H and 26 for Fe. The most efficient collisions are with lower energy cosmic rays, since both the energy loss rate and the cosmic ray flux increase with decreasing energy. The energies and rates in Table 1, therefore, have been calculated for $\Delta E = E = 0.2$ for both hydrogen and iron nuclei. The fluxes of cosmic rays with $E < 0.2$ are not well known. However Cesarsky and Völk (1978) find that cosmic rays with $E < 0.05$ do not penetrate typical molecular clouds, so that the neglect of cosmic rays with $E < 0.2$ has little effect on the rates and energies of Table 1.

10. Chemical explosions. Greenberg (1973) has suggested that chemical explosions may occur in interstellar grains. These chemical explosions have been observed in the laboratory, after warming of UV irradiated "dirty ice" mixtures above 27 K (d'Hendecourt *et al.* 1982). If cold grains store chemical potential energy in molecules in their grain mantle, then after some triggering event a runaway chemical reaction may occur which heats the grain, and which

may cause loss of some or all mantle molecules. This triggering event provides either the necessary activation energy, or a higher grain temperature which allows diffusion of reactive molecules through the grain mantle. The energy available for grain heating is $\sim N_{bond} E_{bond}$, where N_{bond} is the number of bonds formed in the chemical explosion, and E_{bond} as before is ~ 5 eV. Grains which are as small as 10 Å, in the vicinity of a B star, are heated by absorption of UV photons too frequently to retain molecules accreted from the gas in a mantle. Thus for 10 Å sized grains a chemical explosion can occur at most once, perhaps when a grain previously isolated in the molecular cloud is first exposed to stellar radiation. The rate for 10 Å sized grains, therefore, is on the order of the inverse of the cloud lifetime, T_{cloud}, which is taken to be the age of the central stars of the reflection nebulae, ~ 10^5 y (Strom *et al.* 1975). In this case also N_{bond} is taken to be the total number of atoms N in the grain, or $N_{bond} = N \cong (a/d)^3$, where $d \sim 3$ Å is the grain lattice spacing. Larger grains may be able to retain grain mantles, in which case the rate of chemical explosions would depend on the rate of the triggering event, which is not known. For this mechanism to be effective as an explanation of the observed near infrared emission, $N_{bond} E_{bond}$ must at least equal the energy $3NkT$ required to heat a grain containing N atoms to a temperature T = 1000 K. A rough estimate of the required rate, since the expected rate is unknown, is the inverse of the time to accrete $N_{bond} = 3NkT/E_{bond}$ atoms, or $R \sim n_{mol} \sigma_d v_d / N_{bond}$. This is the value given in Table 1. The number density of molecules n_{mol} is on the order of $3 \times 10^{-4}\, n_H$, where $n_H = 10^4$ cm^{-3} and 3×10^{-4} is the abundance of carbon relative to hydrogen. As before v_d is taken to be 2 km s^{-1} for grains of radius $a = 0.1\ \mu$m in the molecular cloud. Heating events which raise the grain temperature high enough to evaporate some of the accreted mantle molecules probably occur more frequently than the events which cause chemical explosions, so the true

rate is probably lower than that in Table 1. It is possible, in fact, that the equilibrium grain temperature near the star, ~ 70 K, is high enough that the mantle molecules are unable to store chemical energy, in which case the rate would be the same as for smaller grains, ~ T_{cloud}^{-1}.

APPENDIX C

The observed near infrared luminosity L_{NIR}, if due to thermal emission, is related to the number of grains N_d by $L_{NIR} = N_d L_d$, where L_d is the average luminosity of an individual dust grain. The average grain luminosity is given by $L_d = RE$, where R is the rate of heating events and E is the average energy of a heating event. This is true whether the grain radiates its heat input E in a time short compared to the time between heating events, as is the case for thermal fluctuations, or whether the grain is in thermal equilibrium with the input heating energy, so that its luminosity as a function of time is approximately constant and equal to L_d. The number of grains is $N_d = x\beta n_H V m_H / m_d$, where m_H is the mass of a hydrogen atom, m_d is the mass of an individual grain, x is the mass fraction of grains which radiate in the near infrared, β is the total dust-to-gas mass ratio, and the total number of hydrogen atoms is given by the product of the number density of hydrogen, n_H, and the emitting volume, V. The mass of a grain is $m_d = 4\pi\rho a^3/3$, where ρ is the density of the grain and a is the grain radius. Thus the fraction of the dust mass which radiates in the near infrared is

$$x = \frac{4\pi\rho a^3 L_{NIR}}{3\beta m_H n_H V E R}.$$

If thermal fluctuations are considered, then the heat input E is $\sim 3NkT$, where N is the number of molecules in the grain and T is the peak temperature attained after the heating event. This assumes that the high temperature limit of the Debye heat capacity is applicable. The value of N is approximately $(a/d)^3$, where d is the grain lattice spacing. In this case, therefore,

$$x = \frac{4\pi\rho d^3 L_{NIR}}{9\beta m_H n_H V kT R}.$$

The observed value of L_{NIR}/V for the three reflection nebulae, assuming a spherical geometry, is $\sim 2 \times 10^{-20}$ erg cm^{-3} s^{-1}, and the observed color temperature is 1000 K. By adopting $\rho = 2$ g cm^{-3}, $\beta = 10^{-2}$, and $d = 3$ Å, one finds

$$xR = 7 \times 10^{-7} \left[\frac{10^3 \text{ cm}^{-3}}{n_H}\right] \left[\frac{1000\ K}{T}\right] \text{s}^{-1}.$$

This value for xR allows one to find x, given an assumed rate of heating events R. Alternatively, one can find a minimum value for R, by requiring $x \leq 1$.

APPENDIX D

The grain size distribution proposed by MRN is $n(a)da = n_0\, a^{-3.5}da$, $a_+ > a > a_-$, where these authors took the size limits of the distribution to be a_+ = 0.25 μm and a_- = 0.005 μm. This distribution was derived by fitting the observed interstellar extinction between 0.1 and 1 μm with a mixture of graphite and silicate grains. Since the extinction at any wavelength λ is most sensitive to grains of size a_0, where $a_0 = \lambda/2\pi$, the limits they adopted for their size distribution primarily reflect the wavelength range of the observations to which they fit their model.

The mass of grains in a size range da is

$$m(a)da = \frac{4\pi\rho a^3}{3}\, n_0\, a^{-3.5}da,$$

while the total mass of grains is

$$M_d = \int_{a_-}^{a_+} m(a)da = \frac{8\pi\rho n_0}{3}(a_+^{1/2} - a_-^{1/2}).$$

The mass fraction of grains in a given size range, $x(a)da$, then is

$$x(a)da = \frac{m(a)da}{M_d} = \frac{da}{2\,a^{1/2}\,(a_+^{1/2} - a_-^{1/2})}.$$

For thermal fluctuations in small grains, $a \sim T^{-1/3}$, where T is the peak temperature, and $da/a = \Delta T/3T$. The observed color temperatures in the reflection nebulae range from 900 to 1100 K (paper 1), or $\Delta T/T \sim 0.2$. The mass fraction is not sensitive to the value of a_-, so $a_- = 0$ is taken. If a = 10 Å and a_+ = 0.25 μm, then $x(a)da = 2 \times 10^{-3}$. This should be compared to the value of x found before, $xR \sim 7 \times 10^{-7}$ (10^3 cm$^{-3}/n_H$) (1000 K/T) s^{-1}. The value of x found by adopting $R = 2 \times 10^{-4}$ s^{-1}, the rate for photon absorption by 10 Å radius grains (Table 1; Appendix B), is $x \sim 3 \times 10^{-3}$, in good agreement with the value

found by extrapolating the MRN grain size distribution to smaller grain sizes.

The absorption cross section in a size range da is

$$C_{abs}(a)da = Q_{abs}(a)\,\pi a^2\,\frac{n(a)da}{n},$$

where $n = \int_{a_-}^{a_+} n(a)da$. As before $n(a)da = n_0\,a^{-3.5}da$. For simplicity an absorption efficiency $Q_{abs}(a)$ is taken of $Q_{abs}(a) = 1$ for $a > a_0$ and $Q_{abs}(a) = a/a_0$ for $a < a_0$, where $a_0 = \lambda/2\pi$. The total absorption cross section at the wavelength λ is

$$C_{abs} = \int_{a_-}^{a_+} C_{abs}(a)da$$

$$= \int_{a_-}^{a_0} \frac{a}{a_0}\pi a^2\,\frac{n_0 a^{-3.5}}{n}da + \int_{a_0}^{a_+} \pi a^2\,\frac{n_0 a^{-3.5}}{n}da$$

$$= \frac{2\pi n_0}{n\,a_0^{1/2}}\left[2 - \left[\frac{a_-}{a_0}\right]^{1/2} - \left[\frac{a_0}{a_+}\right]^{1/2}\right].$$

Thus the fraction of the total absorption cross section due to a size range da is

$$\frac{C_{abs}(a)da}{C_{abs}} = \frac{Q_{abs}(a)}{2\left[2 - \left[\frac{a_-}{a_0}\right]^{1/2} - \left[\frac{a_0}{a_+}\right]^{1/2}\right]}\left[\frac{a_0}{a}\right]^{1/2}\frac{da}{a}.$$

The fraction of stellar luminosity absorbed by grains in a size range da, relative to the total stellar luminosity absorbed by grains, is on the order of $C_{abs}(a)da/C_{abs}$, evaluated at the wavelength where the star emits most of its energy. For the central stars of the reflection nebulae this wavelength is ~ 0.15 μm. Since $a_0 = (0.15/2\pi)$ μm, $Q_{abs}(a) = a/a_0$ for $a = 10$ Å. Adopting the same values for a_+, a_-, and da/a as before, then the MRN size distribution would predict $\sim 4 \times 10^{-3}$ of the reradiated stellar luminosity, absorbed by grains, would be emitted at near infrared wavelengths. This is in reasonable agreement with

the observed fraction of near infrared to total infrared luminosity, $\sim 10^{-2}$.

APPENDIX E

One is interested in finding the maximum surface brightness S_{max} of a reflection nebula, in order to estimate the largest possible contribution to the observed emission from reflected light. If a reflection nebula is optically thin, then its surface brightness due to reflected light is maximized by assuming the dust is distributed in a thin sheet which is for convenience taken to be perpendicular to the line of sight. In this case the surface brightness, S, at an angular offset on the sky φ from the illuminating star, depends on the total extinction optical depth through the nebula τ, the dust albedo ω, the scattering angle θ, the phase function of the grains $H(\theta)$, and the dereddened stellar flux density F_* as follows (Jura 1979):

$$S = \frac{\tau\omega\, H(\theta)\, \sin^2\theta\, F_*}{4\pi\varphi^2}. \qquad \text{(A1)}$$

$H(\theta)$ is most often characterized by a Henyey-Greenstein phase function,

$$H(\theta) = (1-g^2)\,(1+g^2-2g\cos\theta)^{-\frac{3}{2}}, \qquad \text{(A2)}$$

where $g = \langle\cos\theta\rangle$ is the phase asymmetry mentioned earlier, or by a Rayleigh phase function,

$$H(\theta) = \frac{3}{4}(1+\cos^2\theta). \qquad \text{(A3)}$$

One now finds the maximum surface brightness S_{max} by varying the distance of the star from the sheet of dust, along the line of sight, which at a given angular offset on the sky φ corresponds to varying the scattering angle θ. For Rayleigh scattering (eq. A3), the maximum surface brightness is found when the distance between the star and the sheet is 0, or when the scattering angle is 90°. For a Henyey-Greenstein phase function (eq. A2) one finds, by differentiating eq. A1

with respect to θ, that for a given phase asymmetry g there is a value of θ which maximizes the surface brightness. The value of S at this optimum scattering angle depends weakly on g, and is maximum for $g = 0$ or isotropic scattering. The scattering angle which maximizes S when $g = 0$ is again 90°, as was found for Rayleigh scattering. The maximum surface brightness is therefore found by assuming that the scattering is isotropic and the distance of the observed nebular position from the star is equal to the projected distance on the sky, which implies that the illuminating star is embedded in the thin sheet of dust. Since the nebula is so far assumed to be optically thin, extinction between the star and the scattering dust can be ignored. The maximum surface brightness for an optically thin nebula is thus found by setting $g = 0$, $\omega = 1$, and $\theta = 90°$ in eq. A1:

$$S_{max} = \frac{\tau F_*}{4\pi\varphi^2}. \tag{A4}$$

The surface brightness S of an optically thick nebula is much more difficult to calculate than for an optically thin nebula, since multiple scattering and internal extinction are important. Estimating S_{max}, however, is somewhat simpler than finding an exact value of S. One would like by analogy with eq. A4 to write

$$S_{max} = \frac{\tau_{eff} F_*}{4\pi\varphi^2}, \tag{A5}$$

where τ_{eff} and hence S_{max} are functions of the angular dependence of scattering $H(\theta)$, ω, φ, the true optical depth τ of the nebula, and the nebular geometry. Intuitively one expects $\tau_{eff} \cong 1 - e^{-\tau}$, or $\tau_{eff} \lesssim 1$.

Chandrasekhar (1950) presents the solution to the equation of transfer in the case of a star in front of a uniform slab of dust of infinite optical depth, for

isotropic and Rayleigh scattering. Approximate solutions are also presented for the case of a star in front of a uniform slab of dust of finite optical thickness, for isotropic scattering. The results for infinite optical depth and isotropic scattering are that $\tau_{eff} \leq 1$ for $\omega \leq 0.925$, and the maximum value of τ_{eff} is for $\omega = 1$, where $\tau_{eff} = 1.5$. The results for Rayleigh scattering with infinite optical depth and $\omega = 1$ are almost identical to the case of isotropic scattering with $\omega = 1$. The value of τ_{eff} for finite optical depths is less than that for infinite optical depth, as expected. As τ increases τ_{eff} also increases, until at $\tau = 2$ there is little difference between the finite and infinite optical depth cases.

Chandrasekhar's results are limited to relatively isotropic phase functions and to parallel illumination of the dust by a foreground star. White (1979) has considered parallel illumination of an infinite slab with nonisotropic phase functions, while Witt (1977*a*,*b*) has considered the cases of stars embedded in or extremely close to the surfaces of slabs of finite optical depth, with both isotropic and nonisotropic phase functions. The results of these numerical calculations are that $\tau_{eff} < 1$ for all the cases considered by White and Witt. It thus seems that in the wide range of physical situations investigated in these theoretical calculations the surface brightness S does not much exceed the value obtained by setting $\tau_{eff} = 1$ in eq. A5, and is generally considerably less. It therefore seems reasonable to adopt as the maximum possible surface brightness for an optically thick nebula

$$S_{max} = \frac{F_*}{4\pi\varphi^2}. \qquad \text{(A6)}$$

APPENDIX F

The 2.2 μm luminosity function in NGC 2068 derived in paper 2 can be used to predict the number and luminosity of stars fainter than the scan completeness limits, in order to estimate how much of the extended near infrared emission observed at 2.2 μm in the three reflection nebulae is actually due to emission from stars in the associated cluster.

The luminosity functions for main sequence (MS) and pre-main sequence (PMS) stars are assumed to take the form $n(K) \sim 10^{\gamma K}$ until some cutoff in luminosity, fainter than which it is zero. The cutoff for PMS stars is at spectral type M5 (Herbig and Rao 1972). The cutoff for MS stars is also taken to be M5, somewhat earlier than the M6 turnover in field MS stars found by Probst and O'Connell (1982).

At distances of 440 pc for NGC 7023 and 500 pc for NGC 2023 and NGC 2068, a MS spectral type of M5 corresponds to observed, unreddened, K magnitudes of 15.5 mag and 15.8 mag respectively. The PMS stars were assumed to lie above the main sequence at K by the same amount, 3.3 mag, that HD 200775 does. This assumption is consistent with published 2.2 μm data on PMS stars in other regions, for a wide range of spectral types. The H-R diagrams derived by Cohen and Kuhi (1979) from their observations also show that the PMS stars lie in a band $\sim$ 3.6 mag above the main sequence. With this assumption, then, the M5 cutoff in the luminosity function for PMS stars corresponds to observed K magnitudes of 12.2 and 12.5 mag for distances of 440 pc and 500 pc respectively.

The model for the star clusters in the reflection nebulae is one in which the stars are contained in a uniform slab of dust. The spatial distribution of the stars is assumed to be uniform along the line of sight direction, and to depend on the projected radius R as R^x, where x is determined from the observations of the stellar clusters in each nebula (paper 2). Stars within the cloud will be

reddened by amounts proportional to their depth within the cloud, up to an amount corresponding to the total extinction through the cloud. Thus the total surface brightness from stars fainter than the scan completeness limit in each cloud, at a projected radius R, is found by integrating the luminosity function up to its cutoff at a given depth into the cloud, and then integrating the reddened flux density along the line of sight, normalizing by the surface brightness of stars brighter than the scan completeness limit at that projected radius.

The total extinction through the cloud assumed for the three reflection nebulae was the extinction derived from the ^{13}CO column densities. Using $A_V/^{13}CO = 4 \times 10^{-16}$ mag cm^2 (Dickman 1975), $A_V/A_K = 11$ (Johnson 1968), and peak ^{13}CO column densities of 1×10^{16} cm^{-2} (Loren, VandenBout, and Davis 1973), 1×10^{17} cm^{-2} (Milman *et al.* 1975), and 6×10^{16} cm^{-2} (Milman *et al.* 1975), for NGC 7023, 2023, and 2068 respectively, one finds A_K = 0.4, 4, and 2 mag.

The best estimate of the values of the total 2.2 μm flux density from faint stars in the three reflection nebulae are 240, 400, and 250 mJy for NGC 7023, 2023, and 2068 respectively. These values have had subtracted from them the flux densities of those stars fainter than the completeness limit which have already been discovered (paper 2). These values are typically uncertain by factors of $\sim$ 2, mainly due to the uncertainty in the fraction of stars which are PMS, in the sense that a higher fraction of PMS stars corresponds to a lower flux density of faint stars. This fraction was taken, in the best estimate, to be the lower limit determined in paper 2 for each nebula, or 50%, 60%, and 30% for NGC 7023, 2023, and 2068 respectively. The faint stars are not the dominant component of the observed near infrared extended emission in NGC 7023, NGC 2023, and 2068, accounting for at most 10-20 % of the surface brightness.

REFERENCES

Aitken, D. K. 1981, in IAU Symposium **96**, *Infrared Astronomy*, eds. C.G. Wynn-Williams and D.P. Cruikshank (Dordrecht:Reidel).

Allamandola, L. J., Greenberg, J. M., and Norman, C. A. 1979, *Astr. Ap.*, **77**, 66.

Allen, M. and Robinson, G. W. 1975, *Ap. J.*, **195**, 81.

Allen, M. and Robinson, G. W. 1977, *Ap. J.*, **212**, 396.

Beckwith, S., Evans, N.J., Becklin, E.E., and Neugebauer, G. 1976, *Ap. J.*, **208**, 390.

Biermann, P. and Harwit, M. 1980, *Ap. J.*, **241**, 405.

Black, J. H., and Dalgarno, A. 1976, *Ap. J.*, **203**, 132.

Brown, R. L., Knapp, G. R., Kuiper, T. B. H., and Kuiper, E. N. R. 1975, *Ap. J. (Letters)*, **195**, L23.

Cesarsky, C. J. and Völk, H. J. 1978, *Astr. Ap.*, **70**, 367.

Chandrasekhar, S. 1950, *Radiative Transfer* (Oxford University Press).

Cohen, M. and Kuhi, L. V. 1979, *Ap. J. Suppl.*, **41**, 743.

Cowie, L. L. 1978, *Ap. J.*, **225**, 887.

Dalgarno, A., and McCray, R. A. 1972, *Ann. Rev. Astron. Ap.*, **10**, 375.

d'Hendecourt, L. B., Allamandola, L. J., Baas, F., and Greenberg, J. M. 1982, *Astr. Ap.*, **109**, L12.

Dickman, R.L. 1975, Ph.D. thesis, Columbia University.

Draine, B. T. 1981, *Ap. J.*, **245**, 880.

Duley, W. W. 1973, *Nature Phys. Science*, **244**, 57.

Dwek, E., Sellgren, K., Soifer, B. T., and Werner, M. W. 1980, *Ap. J.*, **238**, 140.

Elias, J.H. 1978, *Ap. J.*, **223**, 859.

Elias, J.H., Frogel, J.A., Matthews, K., and Neugebauer, G. 1982, *A. J.*, **87**, 1029.

Emerson, J. P., Furniss, I., and Jennings, R. E. 1975, *M. N. R. A. S.*, **172**, 411.

Felli, M., Gahm, G. F., Harten, R. H., Liseau, R., and Panagia, N. 1982, *Astr. Ap.*, **107**, 354.

Greenberg, J. M. 1973, in *Molecules in the Galactic Environment*, eds. M. A. Gordon and L. E. Snyder (John Wiley:New York).

Greenberg, J. M., and Hong, S. S. 1974, in *IAU Symposium No. 60, Galactic and Radio Astronomy*, eds. F. Kerr and S. C. Simonson (Dordrecht:Reidel).

Guetter, H. H. 1979, *A. J.*, **84**, 1846.

Harvey, P. M., Thronson, H. A., and Gatley, I. 1980, *Ap. J.*, **235**, 894.

Harwit, M. 1975, *Ap. J.*, **199**, 398.

Haslam, C.G.T., Hills, D.L., Matthews, H.E., and Salter, C.J. 1978, *Astr. Ap.*, **70**, 575.

Herbig, G.H. and Rao, N.K. 1972, *Ap. J.*, **174**, 401.

Jewitt, D. 1982, private communication.

Johnson, H.L. 1968, in *Nebulae and Interstellar Matter*, eds. B.M. Middlehurst and L.H. Aller (The University of Chicago Press:Chicago).

Jura, M. 1979, *Ap. J.*, **231**, 732.

Kittel, C. 1969, *Thermal Physics* (John Wiley:New York).

Knapp, G. R., Brown, R. L., and Kuiper, T. B. H. 1975, *Ap. J.*, **196**, 167.

Kreibig, U. 1974, *J. Phys. F*, **4**, 999.

Kurucz, R. L. 1979, *Ap. J. Suppl.*, **40**, 1.

Lee, T.A. 1968, *Ap. J.*, **152**, 913.

Leger, A., Omont, A., and Jura, M. 1983, preprint.

Loren, R.B., VandenBout, P.A., and Davis, J.H. 1973, *Ap. J. (Letters)*, **185**, 67.

Martin, T. P. 1973, *Phys. Rev. B*, **7**, 3906.

Mathis, J.S., Rumpl, W., and Nordsieck, K.H. 1977, *Ap. J.*, **217**, 425 (MRN).

Milman, A.S., Knapp, G.R., Kerr, F.J., Knapp, S.L., and Wilson, W.J. 1975, *A. J.*, **80**, 93.

Neugebauer, G. 1982, private communication.

Neugebauer, G., Oke, J.B., Becklin, E.E., and Matthews, K. 1979, *Ap. J.*, **230**, 79.

Neugebauer, G., Soifer, B. T., Matthews, K., Margon, B., and Chanan, G. A. 1982, *A. J.*, **87**, 1639.

Pankonin, V. and Walmsley, C.M. 1976, *Astr. Ap.*, **48**, 341.

Pankonin, V. and Walmsley, C.M. 1978, *Astr. Ap.*, **67**, 129.

Price, S. D. 1977, AFGL-TR-77-0160.

Price, S. D., and Walker, R. G. 1976, AFGL-TR-76-0208.

Probst, R.G. and O'Connell, R.W. 1982, *Ap. J. (Letters)*, **252**, 69.

Purcell, E. M. 1976, *Ap. J.*, **206**, 685.

Sargent, A. I. 1982, private communication.

Sellgren, K. 1981, *Ap. J.*, **245**, 138.

Sellgren, K. 1983, to be published in *A. J.* (paper 2).

Sellgren, K., Werner, M. W., and Dinerstein, H. L. 1983*a*, submitted to *Ap. J. Lett.* (paper 1).

Sellgren, K., Werner, M. W., and Dinerstein, H. L. 1983*b*, in preparation.

Sellgren, K., Becker, R., Pravdo, S.H., and White, R.L. 1983*c*, in preparation.

Shull, J. M. 1978, *Ap. J.*, **226**, 858.

Spitzer, L. 1978, *Physical Processes in the Interstellar Medium* (John Wiley:New York).

Strom, K.M., Strom, S.E., Carrasco, L., and Vrba, F.J. 1975, *Ap. J.*, **196**, 489.

Strom, K.M., Strom, S.E., and Vrba, F.J. 1976, *A. J.*, **81**, 308.

Viotti, R. 1969, *Mem. Soc. Astr. Ital.*, **40**, 75.

Whitcomb, S.E., Gatley, I., Hildebrand, R.H., Keene, J., Sellgren, K., and Werner, M.W. 1981, *Ap. J.*, **246**, 416.

White, R.L. 1979, *Ap. J.*, **230**, 116.

Willner, S. P. 1983, in *Galactic and Extragalactic Infrared Spectroscopy, ESLAB Symposium No. 16*, ed. M. F. Kessler.

Witt, A.N. 1977*a*, *Ap. J. Suppl.*, **35**, 7.

Witt, A.N. 1977*b*, *Ap. J. Suppl.*, **35**, 21.

Witt, A.N., and Cottrell, M.J. 1980, *A. J.*, **85**, 22.

Witt, A. N., Schild, R. E., and Kraeman, J. 1983, in preparation.

Zellner, B. 1970, Ph.D. thesis, University of Arizona.

Table 1

Process	Energy (eV) E	grain radius (Å) 10	1000	Rate (s^{-1}) R	grain radius (Å) 10	1000
photon absorption	E_{ph}	10	10	$\frac{L_*(\nu)\Delta\nu Q_{abs}\sigma_d}{4\pi r^2 h\nu}$	2×10^{-4}	3×10^{1}
gas-grain collisions (H II region)	kT_e	1	1	$n_e\sigma_d v_e$	2×10^{-4}	2×10^{0}
gas-grain collisions (molecular cloud)	E_{ads}	0.1	0.1	$n_H\sigma_d v_d$	1×10^{-5}	6×10^{-1}
bond formation (molecular cloud)	E_{bond}	5	5	$\frac{1}{2}n_{mol}\sigma_d v_d$	6×10^{-6}	3×10^{-1}
gas-grain collisions (shock front)	kT_e	20	20	$\frac{n_e\sigma_d v_e V_{sh}}{V_{neb}}$	1×10^{-6}	1×10^{-2}
grain-grain collisions (molecular cloud)	$\frac{1}{2}\xi m_d v_d^2$	4ξ	100ξ	$n_d\sigma_d v_d$	8×10^{-13}	4×10^{-8}
grain-grain collisions (H II region)	$\frac{1}{2}\xi m_d v_d^2$	1ξ	3ξ	$n_d\sigma_d v_d$	4×10^{-15}	6×10^{-11}
grain-grain collisions (shock front)	$\frac{1}{2}\xi m_d v_d^2$	$1\times10^{5}\xi$	$1\times10^{5}\xi$	$\frac{n_d\sigma_d v_d V_{sh}}{V_{neb}}$	1×10^{-17}	1×10^{-13}
cosmic rays (H)	$2a\frac{dE}{dx}$	2	200	$4\pi\varphi_H\Delta E\sigma_d$	1×10^{-13}	1×10^{-9}
cosmic rays (Fe)	$2a\frac{dE}{dx}$	1×10^{3}	1×10^{5}	$4\pi\varphi_{Fe}\Delta E\sigma_d$	2×10^{-17}	2×10^{-13}
chemical explosion (a=10Å)	$N_{bond}E_{bond}$	200	-	T_{cloud}^{-1}	3×10^{-13}	-
chemical explosion (a=0.1μm)	$N_{bond}E_{bond}$	-	1×10^{7}	$\frac{n_{mol}\sigma_d v_d}{N_{bond}}$	-	1×10^{-10}

Note to Table: The rates R and energies E for each grain heating mechanism listed in the table, for grain radii of 10 and 1000 Å, are derived from the formulae given in columns 2 and 5. Explanations of the symbols used in these formulae, as well as detailed discussion of the derivation of the values for R and E given in the table, are given in Appendix B. The dashed line separates mechanisms with rates above and below the minimum required rate of 7×10^{-6} - 7×10^{-8} s^{-1} found in Appendix C.

Figure Captions

Figure 1. Surface brightness maps of NGC 7023 at 2.2 μm and 1.65 μm. Diaphragms of 30" and 60" diameter were used. The position of HD 200775 is marked with a cross. Observations could not be made closer than 30" from HD 200775; contours within this radius have been completed with dashed lines. The surface brightness has been corrected for the contributions of stars found at 2.2 μm in the nebula (paper 2), and for instrumental scattering of light from HD 200775. The contour intervals are 50 mJy into a 60" diameter diaphragm at both 2.2 and 1.65 μm. The 1-σ uncertainties in the surface brightness are 9-13 mJy per 60" diaphragm at 2.2 μm, and 4-17 mJy per 60" diaphragm at 1.65 μm.

Figure 2. Surface brightness maps of NGC 2023 and NGC 2068 at 2.2 μm. A 60" diameter diaphragm was used. The positions of HD 37903 and HD 38563-N are marked with a cross in NGC 2023 and NGC 2068 respectively. The surface brightness has been corrected for the contributions of stars found at 2.2 μm in these nebulae (paper 2). The contours in NGC 2023 are 25, 50, 75, 100, 150, 200, 250, 300, and 350 mJy into a 60" diaphragm. The contour interval in NGC 2068 is 25 mJy into a 60" diaphragm. The 1-σ uncertainty in the 2.2 μm surface brightness of NGC 2023 and NGC 2068 is 7 mJy per 60" diaphragm.

Figure 3. The surface brightness S_ν of NGC 7023 at 2.2 μm (*filled circles*) and 0.55 μm (*open circles*), *vs.* angular offset from HD 200775, north, south, east, and west of this star. The 2.2 μm data are from this paper, using 30" and 60" diameter diaphragms; the 0.55 μm data are from Witt and Cottrell (1980), who used a 50" diameter diaphragm. Error bars represent ± 1 σ uncertainties, and are shown only when larger than ± 0.03 in the log. Upper limits are 3-σ upper

limits at 2.2 μm. The surface brightnesses are given as watt m^{-2} Hz^{-1} $ster^{-1}$ at 2.2 μm and 0.55 μm. Positions with error bars in $\log S_\nu$ of ±0.2 are positions where 2.2 μm data were not directly available. At these positions the 2.2 μm surface brightness was estimated from the 2.2 μm contour map, estimated from a 1.65 μm measurement using an average ratio of 2.2 μm to 1.65 μm surface brightnesses, or was measured directly at 2.2 μm but was corrected for the contribution of a pre-main sequence star which may be variable.

Figure 4. The surface brightness S_ν of NGC 2023 at 2.2 μm (*filled circles*) and 0.55 μm (*open circles*), *vs.* angular offset from HD 37903, along lines at 45° to the cardinal directions, northeast, southeast, northwest, and southwest of this star. The 2.2 μm data are from this paper, using a 60" diameter diaphragm; the 0.55 μm data are from Witt, Schild, and Kraeman (1983), who used a 50" diameter diaphragm. Error bars represent ±1 σ uncertainties, and are shown only when larger than ±0.03 in the log. The upper limit is a 3-σ upper limit at 2.2 μm. The surface brightnesses are given as watt m^{-2} Hz^{-1} $ster^{-1}$ at 2.2 μm and 0.55 μm. Positions with error bars in $\log S_\nu$ of ±0.2 are positions where the 2.2 μm data were corrected for the contribution of a pre-main sequence star which may be variable.

Figure 5. The near infrared spectra of positions in NGC 7023 and NGC 2023. The positions observed are (*a*) 30" west 20" north of HD 200775 in NGC 7023; (*b*) 60" south of HD 37903 in NGC 2023; and (*c*) 14" west 23" north of HD 200775 in NGC 7023. The filled circles are spectrophotometry with 1% (*a*,*b*) or 5% (*c*) resolution. The open squares are broadband photometric measurements. Error bars represent ±1 σ uncertainties, and are only shown when larger than ±5%. Upper limits are 3-σ upper limits on the spectrophotometry. The 4.8 μm

broadband photometry of NGC 2023 (*b*) is a 2.8 σ measurement. The units are flux density within the diaphragm size used, which was 12" (*a*,*b*) or 16" (*c*) in diameter. The observations are from this paper and paper 1.

Figure 6. The 3.3 μm feature-to-continuum ratio plotted *vs.* the ratio of flux densities at 3.8 and 2.2 μm, for NGC 7023 (*filled circles*), NGC 2023 (*open circles*), and NGC 2068 (*open triangle*). The observations are from paper 1. Error bars represent $\pm$ 1 σ uncertainties, and are shown only when larger than $\pm$5%.

Figure 7. The $J-H$ colors plotted *vs.* the $H-K$ colors for nebular positions in NGC 7023 (*circles*), NGC 2023 (*squares*), and NGC 2068 (*triangles*). Error bars representing typical $\pm$1 σ uncertainties for the observations are shown in the upper left hand corner. Filled symbols are observations made at Mt. Wilson Observatory, for which no longer wavelength information is available (this paper), while open symbols are observations made at the Infrared Telescope Facility, where observations at 3.8 μm are available (this paper and paper 1). The $J-H$ and $H-K$ colors of the stars found in these nebulae (paper 2) are outlined for comparison with the nebular colors.

Figure 8. The $J-H$ and $H-K$ colors of NGC 7023, NGC 2023, and NGC 2068, plotted *vs.* angular offset from the illuminating star of each reflection nebula. The error bars represent $\pm$1 σ uncertainties.

Figure 9. The energy distributions of NGC 7023 (*top*), NGC 2023 (*middle*), and NGC 2068 (*bottom*). Filled circles are near infrared measurements derived from the integrated 2.2 μm flux density of each nebula (this paper) and the ratios of

surface brightnesses at 1.25, 1.65, 3.8, and 4.8 μm to that at 2.2 μm, at each nebular peak (this paper and paper 1). The open squares are 11 and 20 μm measurements from the AFGL Catalog (Price and Walker 1976) for NGC 7023 and NGC 2023, and from the AFGL Supplemental Catalog (Price 1977) for NGC 2068. The open circles are far infrared measurements from Whitcomb *et al.* (1981) for NGC 7023 and from Harvey, Thronson, and Gatley (1980) for NGC 2023.

Figure 10. The spectra of HD 200775, HD 38563-N, and HD 37903, which are respectively the illuminating stars of the reflection nebulae NGC 7023, NGC 2068, and NGC 2023. For HD 200775 and HD 37903, filled circles represent spectrophotometry, and open squares broad band photometry. For HD 38563-N open circles represent both broad band photometry, at 1.25, 1.65, 2.2, and 3.8 μm, and a 1% resolution spectrophotometric measurement at 3.3 μm. For HD 200775 the resolution for the spectrophotometry was 5% from 1.5 to 2.5 μm, and 1% from 2.9 to 3.6 μm. The spectrophotometry of HD 37903 is 1% resolution. Error bars representing ± 1 σ uncertainties are shown only when larger than $\pm 5\%$.

Figure 11. Ratio of flux densities at 3.8 and 2.2 μm *vs.* the incident stellar flux in units of erg cm^{-2} s^{-1}. The stellar flux is $L_*/4\pi r^2$, where L_* is the total stellar luminosity of the central star and r is the projected distance of the nebular position from the central star. This ratio is plotted for NGC 7023 (*filled circles*), NGC 2023 (*open circles*), and NGC 2068 (*open triangle*); the observations are from paper 1. Error bars represent ± 1 σ uncertainties. The solid curve is the predicted dependence on stellar flux of the ratio of 3.8 to 2.2 μm flux densities, for thermal emission from dust in equilibrium with the stellar radiation field. A dust emissivity proportional to λ^{-1}, where λ is the wavelength, is adopted,

implying the dust temperature T_d is proportional to $(L_*/4\pi r^2)^{1/5}$. The solid curve has been forced through the data at $L_*/4\pi r^2$ = 10 erg cm^{-2} s^{-1} by requiring T_d = 850 K for this value of the stellar flux. Grain models predict a much lower value of T_d for this value of the stellar flux (Appendix A), resulting in a ratio of 3.8 to 2.2 μm flux densities falling far above the top of this figure.

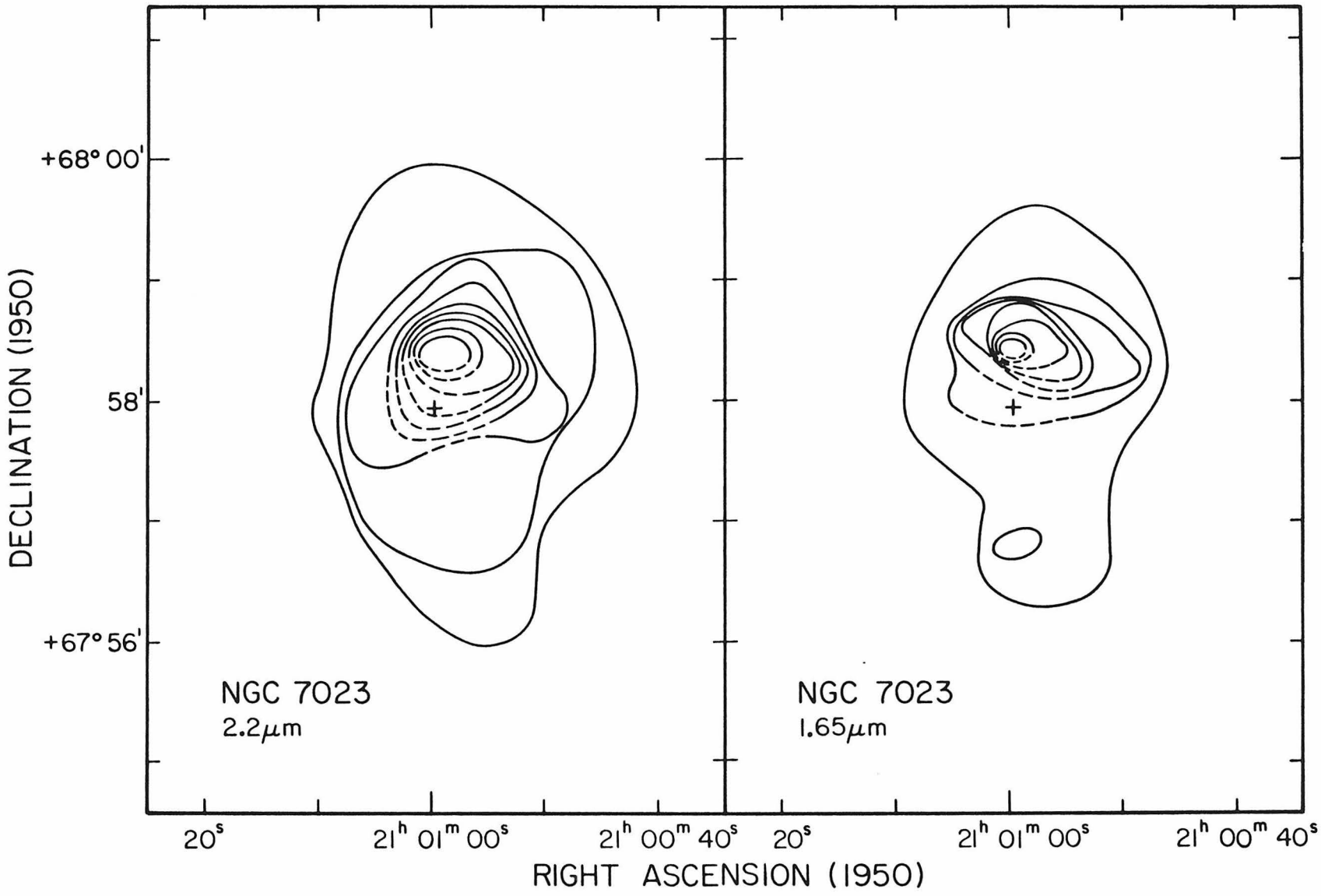
+68° 00'
58'
+67° 56'
DECLINATION (1950)
NGC 7023
2.2μm
NGC 7023
1.65μm
20s
21h 01m 00s
21h 00m 40s
20s
21h 01m 00s
21h 00m 40s
RIGHT ASCENSION (1950)

Figure 1

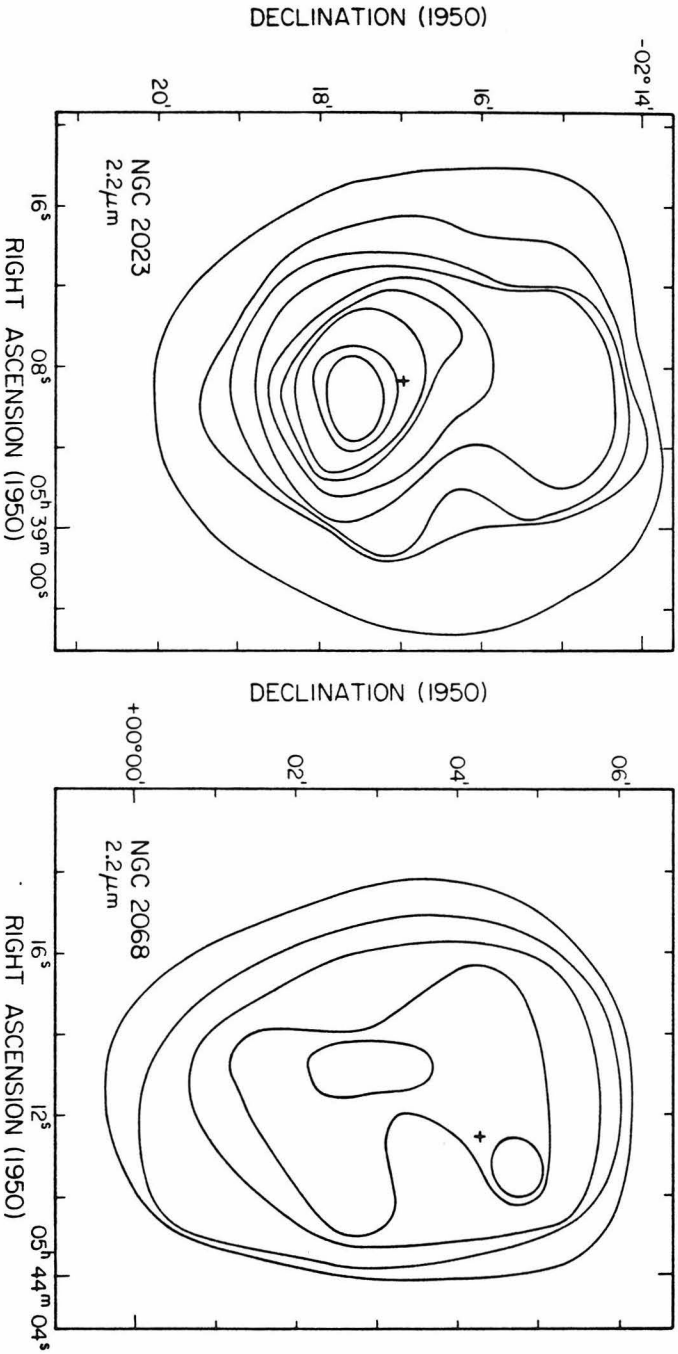
DECLINATION (1950)
-02° 14'
20'
18'
16'
NGC 2023
2.2μm
16ˢ
08ˢ
05ʰ 39ᵐ 00ˢ
RIGHT ASCENSION (1950)
DECLINATION (1950)
+00° 00'
02'
04'
06'
NGC 2068
2.2μm
16ˢ
12ˢ
05ʰ 44ᵐ 04ˢ
RIGHT ASCENSION (1950)

Figure 2

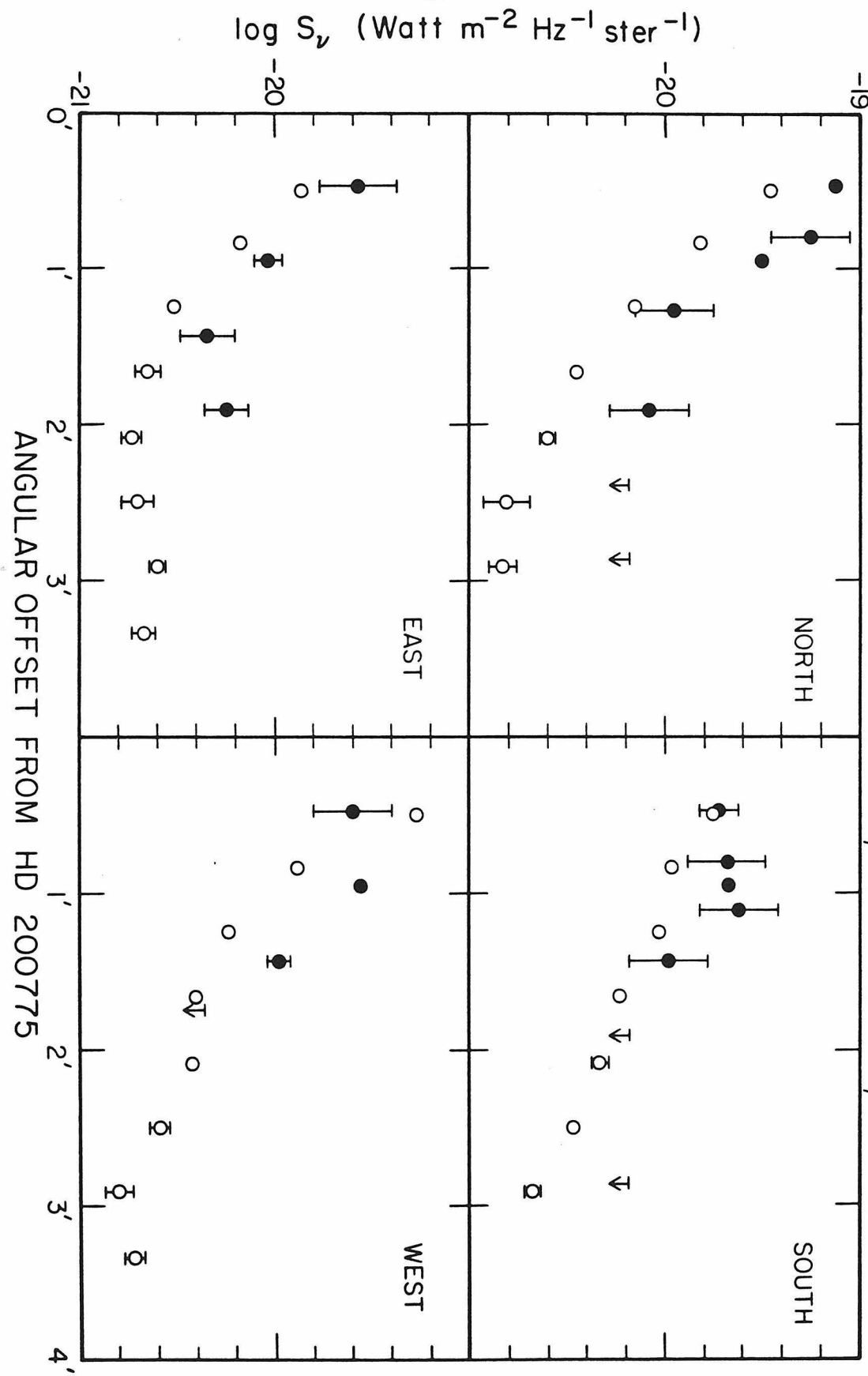
NGC 7023
log S_ν (Watt m^{-2} Hz^{-1} $ster^{-1}$)
-19
-20
-21
NORTH
EAST
SOUTH
WEST
● 2.2μm
○ 0.55μm
0'
1'
2'
3'
4'
ANGULAR OFFSET FROM HD 200775

Figure 3

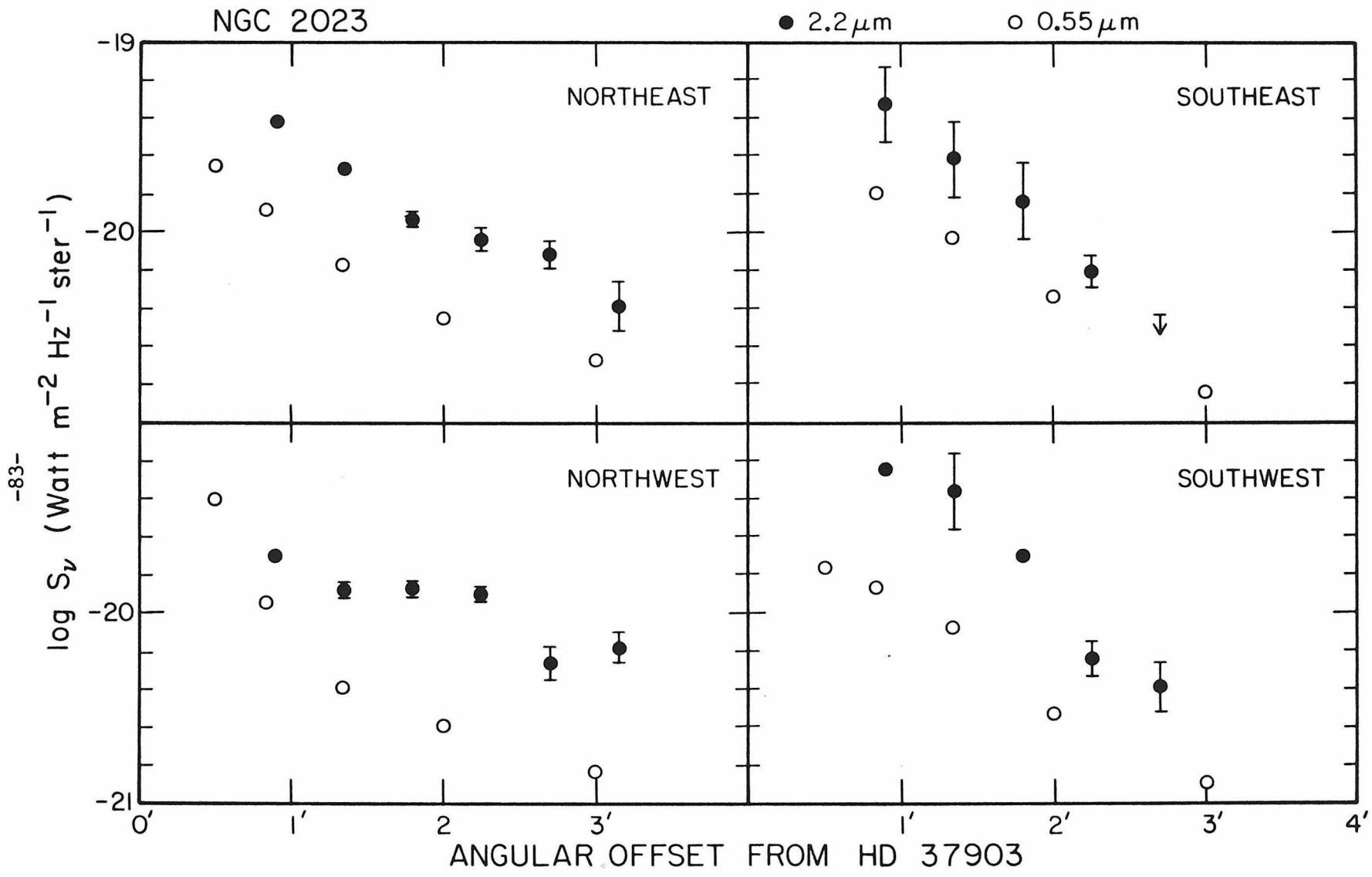
NGC 2023
● 2.2μm
○ 0.55μm
NORTHEAST
SOUTHEAST
NORTHWEST
SOUTHWEST
-19
-20
-20
-21
log S_ν (Watt m^{-2} Hz^{-1} $ster^{-1}$)
0′
1′
2
3′
1′
2′
3′
4′
ANGULAR OFFSET FROM HD 37903

Figure 4

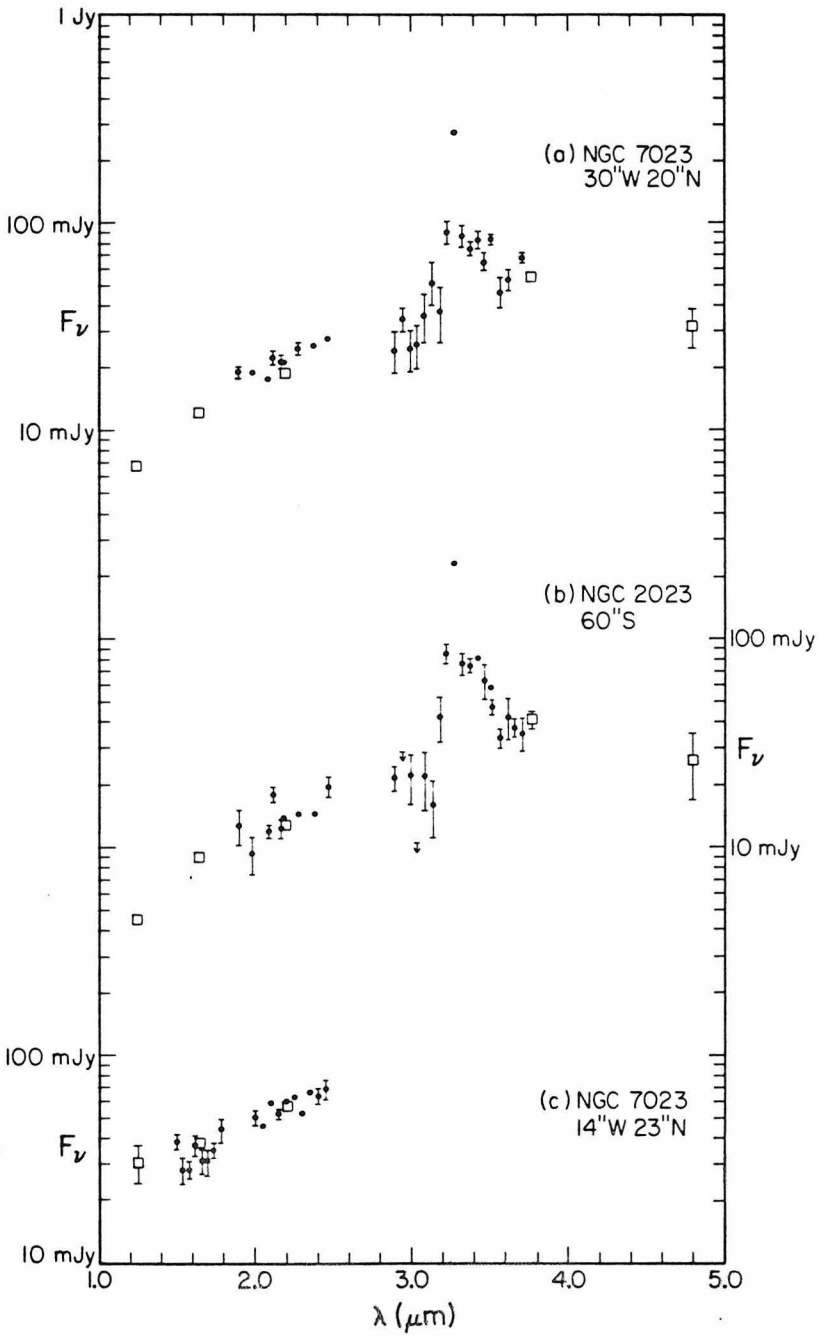
1 Jy
100 mJy
F_ν
10 mJy
(a) NGC 7023
30"W 20"N
(b) NGC 2023
60"S
100 mJy
F_ν
10 mJy
100 mJy
F_ν
10 mJy
(c) NGC 7023
14"W 23"N
1.0
2.0
3.0
4.0
5.0
λ (μm)

Figure 5

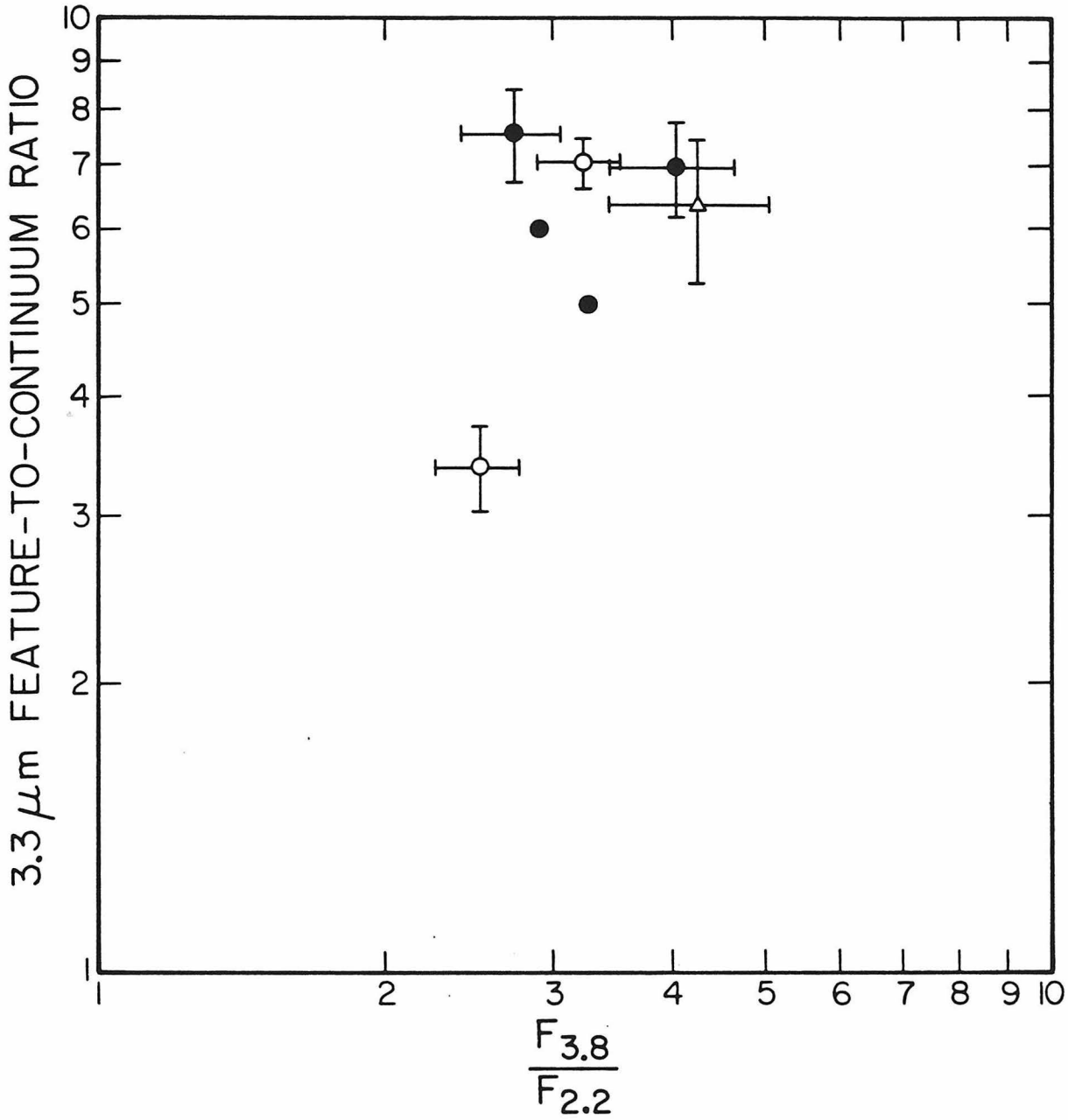
3.3 μm FEATURE-TO-CONTINUUM RATIO
10
9
8
7
6
5
4
3
2
1
1
2
3
4
5
6
7
8
9
10
F3.8 / F2.2

Figure 6

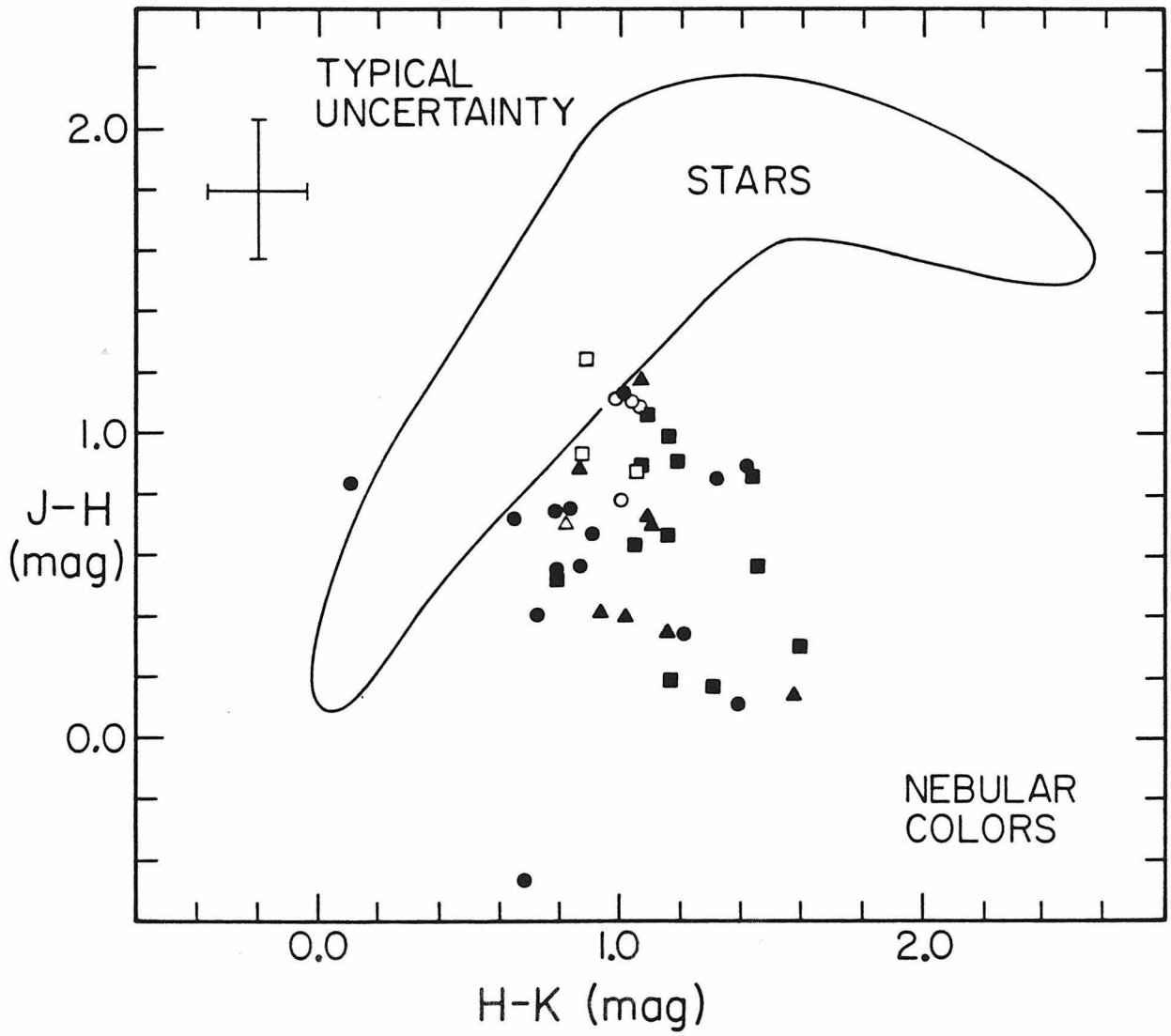
TYPICAL
UNCERTAINTY
STARS
NEBULAR
COLORS
2.0
1.0
0.0
J-H
(mag)
0.0
1.0
2.0
H-K (mag)

Figure 7

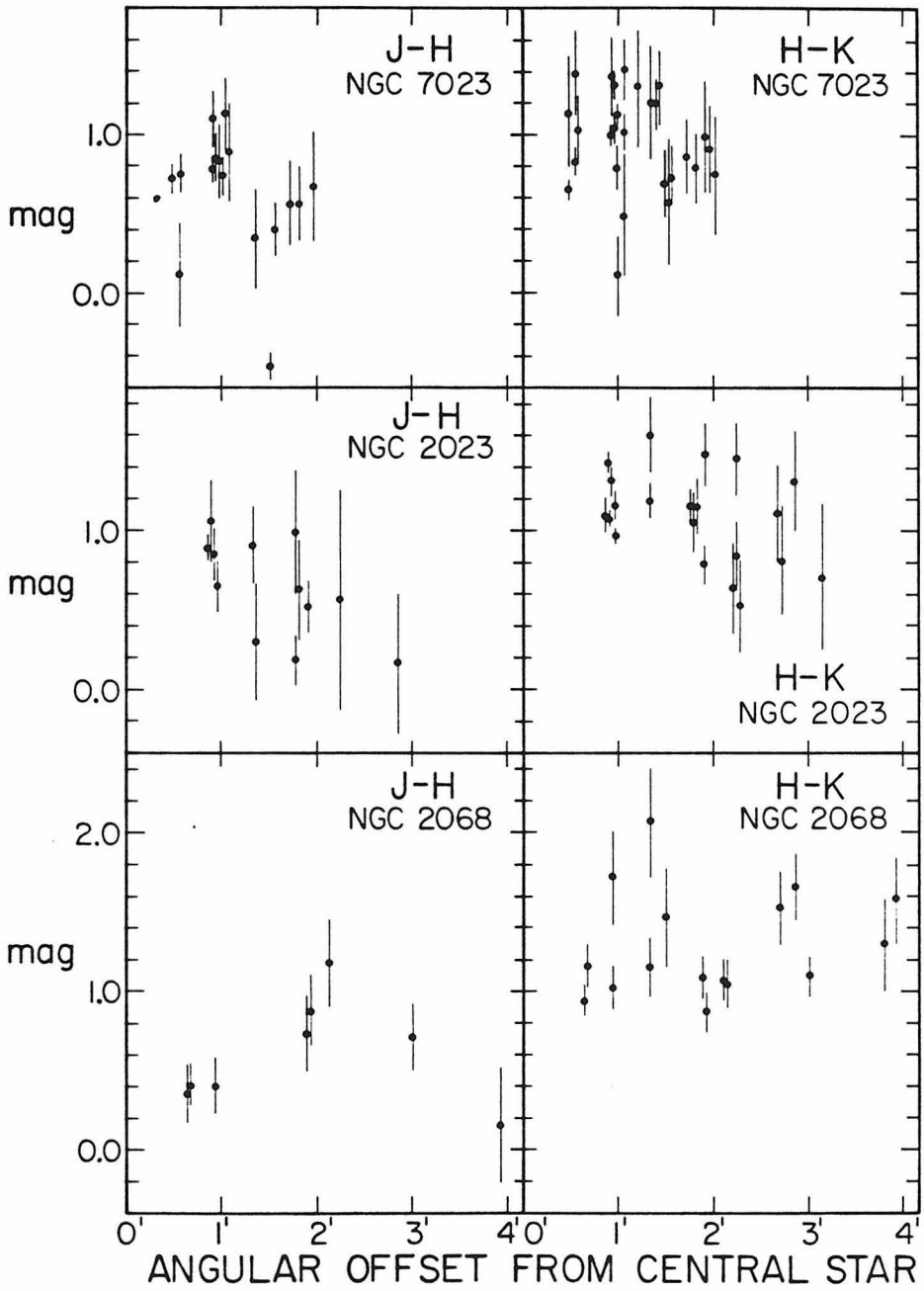
J-H
NGC 7023
H-K
NGC 7023
J-H
NGC 2023
H-K
NGC 2023
J-H
NGC 2068
H-K
NGC 2068
mag
1.0
0.0
2.0
0'
1'
2'
3'
4'
ANGULAR OFFSET FROM CENTRAL STAR

Figure 8

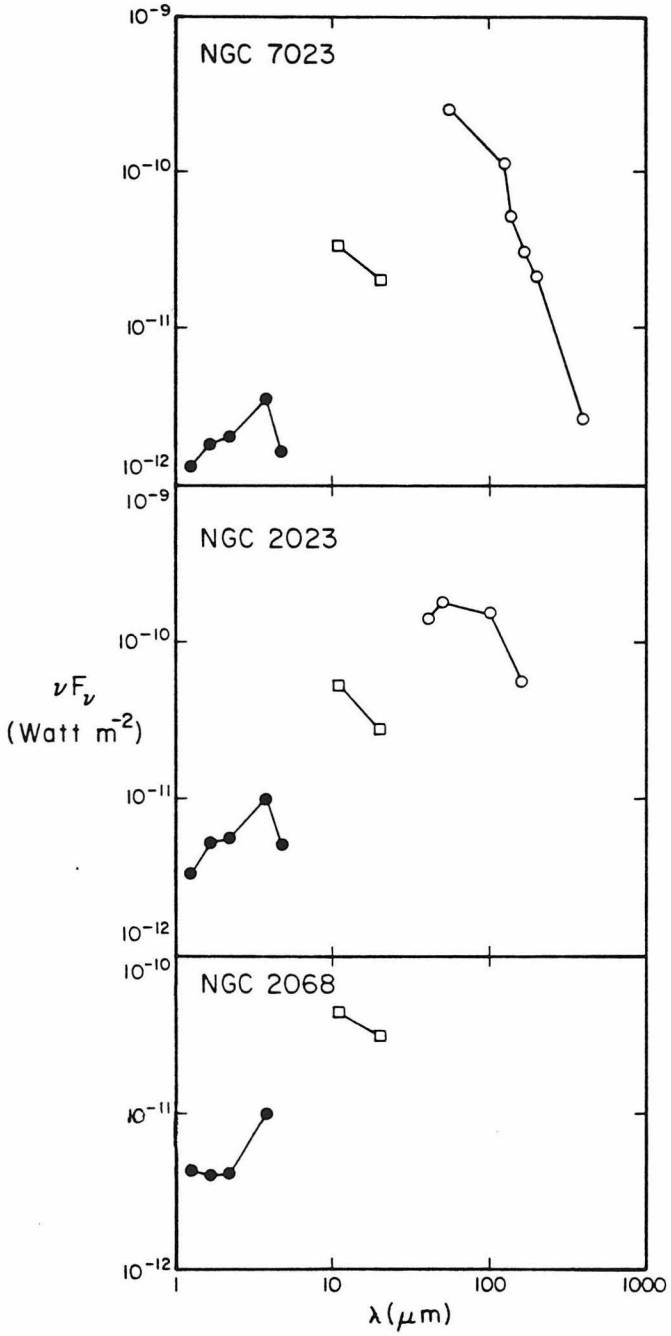
NGC 7023
NGC 2023
NGC 2068
νF_ν
(Watt m^{-2})
$\lambda(\mu m)$
10^{-9}
10^{-10}
10^{-11}
10^{-12}
1
10
100
1000

Figure 9

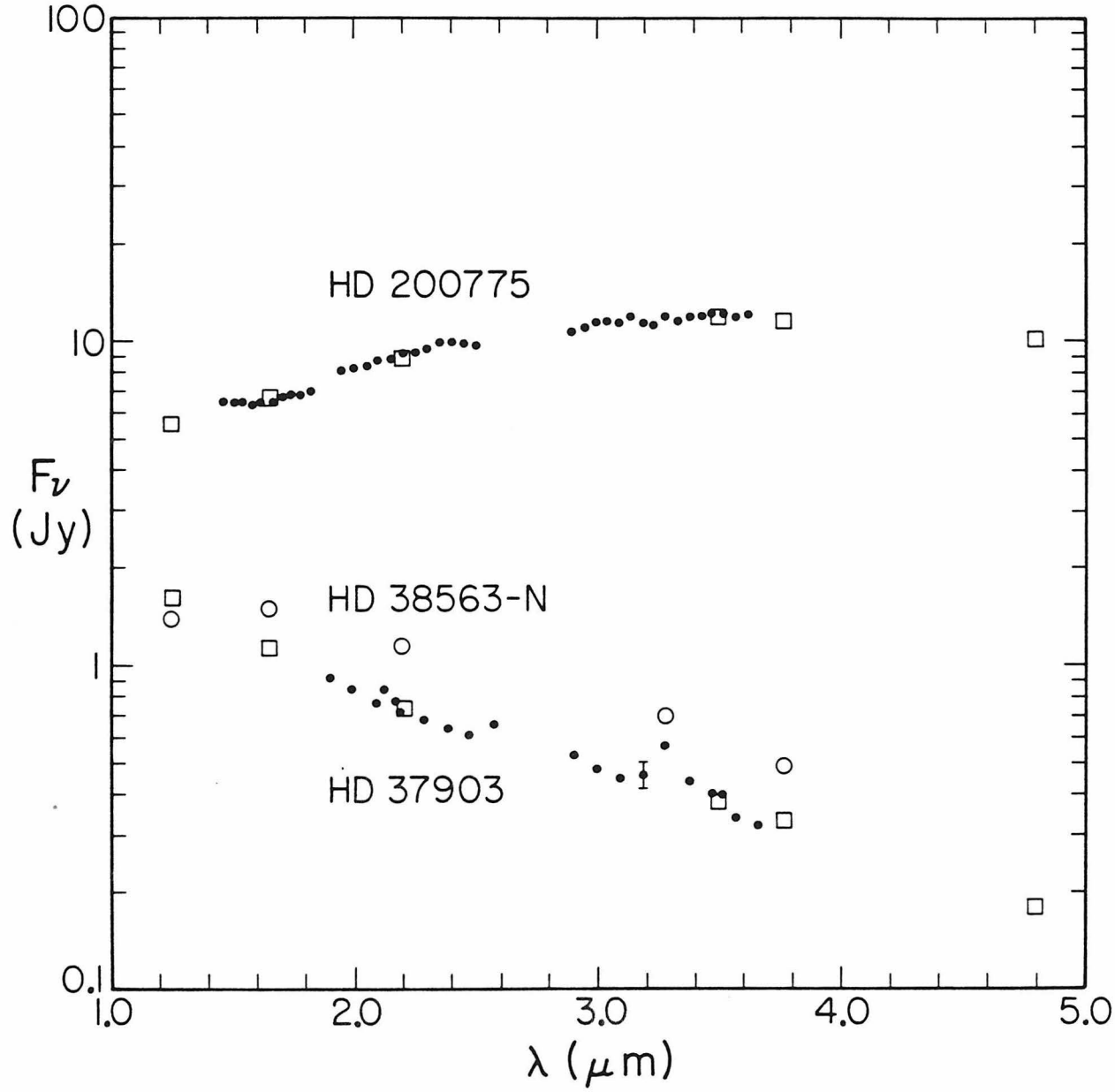

Figure 10

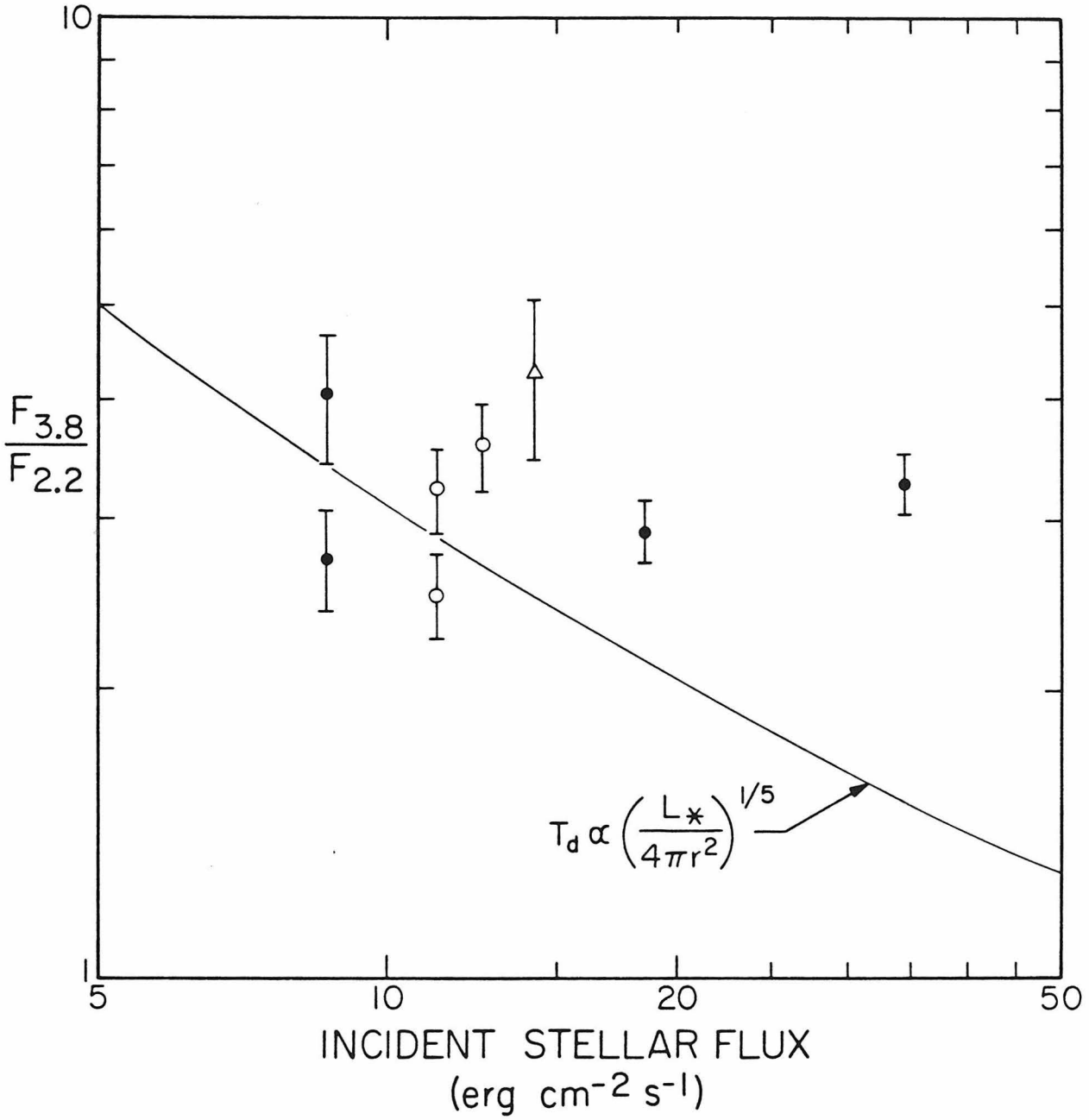
10
1
5
10
20
50
$\frac{F_{3.8}}{F_{2.2}}$
$T_d \propto \left(\frac{L_*}{4\pi r^2}\right)^{1/5}$
INCIDENT STELLAR FLUX
(erg cm^{-2} s^{-1})

Figure 11

PAPER III: PROPERTIES OF YOUNG CLUSTERS NEAR VISUAL REFLECTION NEBULAE

ABSTRACT

Near infrared observations in the reflection nebulae NGC 7023, 2023, and 2068 are used to study clusters of young stars found associated with these nebulae. At least 30-60 % of these stars are pre-main sequence objects, as indicated by their infrared excesses, hydrogen line emission, or irregular variability. The spatial distributions and observed luminosity functions of these young open clusters are derived, and the inferred mass function and star formation efficiencies are discussed.

I. INTRODUCTION

Near infrared observations of dark clouds provide a unique approach to studying low mass star formation. Optical observations are hampered by the large extinctions associated with dark clouds, while radio continuum observations are sensitive only to more massive ionizing stars. Early near infrared searches for embedded stars found an obscured young cluster in the Ophiuchus dark cloud (Grasdalen, Strom, and Strom 1973; Vrba *et al.* 1975), and searches were soon made in many other dark clouds (see Hyland 1981 for a review). Elias (1978*a*,*b*,*c*) showed that many sources found in 2.2 μm scans of dark clouds were background stars not associated with the regions, and that many stars associated with the clouds were pre-main sequence objects. The identification of a substantial background component to 2.2 μm star counts in dark clouds led to an improved understanding of the near infrared extinction in these clouds. The presence of background stars, and of stars not yet on the main sequence, also showed that extreme care must be taken in interpreting near infrared star formation studies in these regions. These effects have been considered in recent estimates of the star formation efficiency in the Chamaeleon dark cloud (Hyland, Jones, and Mitchell 1982).

The observations discussed in this paper are of stars found in the regions near three reflection nebulae, NGC 7023, 2023, and 2068. These stars are shown to be members of young clusters associated with the reflection nebulae. The spatial distributions and luminosity functions of these stars are derived, and estimates of the mass functions and star formation efficiencies are made. The high success rate in finding young clusters of low mass stars is attributable to selecting reflection nebulae for these observations, since this guarantees the absence of high mass (O) stars which would ionize substantial H II regions, while identifying a region of star formation by the presence of a lower mass (B) early

type star still young enough to be physically associated with the cloud from which it formed.

NGC 7023 is at the northern end of a 30' × 60' molecular cloud at a distance of 440 pc (Viotti 1969). The visual reflection nebula is illuminated by the Herbig Be star HD 200775, and the nebula is also associated with a small cluster of T Tauri stars (Weston 1953). NGC 2023 is found in the dark cloud L 1630 (Lynds 1962), and is 20' south of the H II region NGC 2024. The visual reflection nebula is illuminated by the B1.5V star HD 37903. NGC 2068, or M78, is also in L1630. NGC 2068 is 14' south of the active star formation region NGC 2071, and is also 18' north of the Herbig-Haro object HH-24. The visual reflection nebula is illuminated by the northernmost of a pair of stars having $V \sim 10$ mag (Elvius and Hall 1967). These stars, following the notation of Strom *et al.* (1975), will be referred to as HD 38563-N and HD 38563-S. NGC 2023 and 2068 are at a distance of 500 pc (Lee 1968).

The observations reported here include scans at 2.2 μm, and occasionally 1.65 μm, to search for stellar sources; near infrared photometry at 1.25, 1.65, and 2.2 μm for the brighter sources found at 2.2 μm; visual photometry for stars in two of the regions at 0.655 μm; visual and near infrared spectrophotometry for a few stars; and an image tube plate at 0.8 μm of one region. This diverse body of data allows an investigation of the colors, reddening, spectral features, and variability of the stars in these dark clouds. These observations lead to a better understanding of the nature of young stellar objects and low mass star formation occuring in dark clouds, as well as the nature of the dark cloud extinction.

II. OBSERVATIONS

Scans of the reflection nebulae NGC 7023, NGC 2023, and NGC 2068 were made at 2.2 μm, and in some cases, 1.65 μm, using the 100 inch, 60 inch, and 24 inch telescopes at Mt. Wilson Observatory. The areas scanned, wavelength, diaphragm, spacing between source and sky positions, and faintest magnitude detectable are listed in Table 1 for the three nebulae. Adjacent scans were spaced by half the diaphragm diameter. The scans were usually made in nonphotometric conditions, so that the inferred magnitudes are typically reliable to only ~ 0.3 mag, with worse uncertainties in some cases.

A plate of the NGC 7023 region was obtained on the Yerkes Observatory 41 inch reflector, at an effective wavelength of 0.8 μm, using a RG-8 filter and a S-25 image intensifier tube. The 20 brightest stars from this plate were selected and searched for at infrared wavelengths.

Infrared photometry at J (1.25 μm), H (1.65 μm), and K (2.2 μm), using the filters defined by Neugebauer *et al.* (1979), was obtained of many of the stars found in scans and on the 0.8 μm plate. The photometry was calibrated relative to the standard stars given by Elias *et al.* (1982).

Photometry at a wavelength of 0.655 μm, using an r filter as defined by Thuan and Gunn (1976), was obtained for stars in NGC 2023 and NGC 2068 on 1981 September 25. This photometry was derived from 11 direct SIT frames taken on the Palomar 60 inch telescope, using standard techniques described by Kent (1979). Nonphotometric sky conditions resulted in photometric uncertainties of ± 0.2 mag.

A spectrum with a resolution of $\Delta\lambda/\lambda = 1.7 \times 10^{-3}$, from 2.15 to 2.22 μm, was obtained of HD 200775 on 1980 October 9 with the Mt. Wilson Observatory 60 inch telescope. This spectrum was measured with a Fabry-Perot spectrometer, using techniques described in more detail by Sellgren *et al.* (1983*a*).

Spectra from 0.38 μm to 0.76 μm were obtained of 3 stars in NGC 2023 and NGC 2068 on 1981 August 30-31, using the Palomar 200 inch telescope and the double spectrograph blue camera described by Oke and Gunn (1982).

III. RESULTS

a. Photometry

The observations of stars in NGC 7023, 2023, and 2068 are presented in Table 2. The designation given in the first column will be the notation used to refer to the stars throughout this paper, although other designations are also given in Table 2 when available.

Table 2 contains 30, 14, and 56 stars found in NGC 7023, 2023, and 2068 respectively at infrared wavelengths, as well as some stars found only at visual wavelengths. Of these stars, respectively 11, 8, and 15 are brighter than K = 10.5 mag in scan areas typically 6-8' on a side.

The background star count model of Jones *et al.* (1981) can be used to estimate the expected number of background stars in these scan areas. This model agrees very well with observations of background stars in many regions. In particular scans of a 2.4 square degree region near NGC 7023 (Elias 1983, private communication) find 19.2 ± 2.8 stars per square degree brighter than K = 7.5 mag, while the model predicts 15.4 stars per square degree brighter than K = 7.5 mag, in good agreement with the observations. The background star count model predicts that at the galactic latitudes of NGC 7023, 2023, and 2068, 14.2°, 16.6°, and 14.5°, one expects 120, 75, and 86 background stars per square degree with $K \leq 10$ mag, respectively. Similarly one expects 230, 150, and 170 background stars per square degree, respectively, with $K \leq 11$ mag. Thus in the areas scanned only 2 or less background stars with $K \leq 10.5$ mag are expected. Many more stars than this were found in each nebula, so that 75–90% of the stars found in near infrared scans are stars physically associated with the reflection nebulae. This confirms the suggestions of other observers of NGC 7023 (Weston 1953; Strom *et al.* 1972), NGC 2023 (Strom *et al.* 1975), and NGC 2068 (Herbig and Kuhi 1963; Strom *et al.* 1975; Strom, Strom and Vrba 1976) that

these regions contain clusters of young stars. Further arguments for a large fraction of stars physically associated with the clouds are the clear spatial clustering of the stars and the identification of many stars as pre-main sequence stars, as discussed in more detail in sections IV*b* and IV*c*.

Photometry at J, H, and K was obtained for some of these stars, and is given in Table 2. All J, H, and K photometry for each star was obtained on the same night, so that possible variability of a star should not affect its infrared colors. The $J-H$ and $H-K$ stellar colors are plotted in Fig. 1 for each nebula. In these $J-H$ *vs.* $H-K$ diagrams, the reddening line (cf. section IV*a*) is drawn through a point corresponding to the average color of a foreground or background star, which model predictions at 2.2 μm indicate is most likely a K giant. The reddening line for an early type main sequence star is also shown.

In NGC 7023 (Fig. 1*a*) most of the stars appear to have colors appropriate to a normal reddened star. Three stars, however, fall substantially below the reddening line for early type stars, implying that these stars have an infrared excess. The remaining stars are, by their colors, consistent with either being background giants or stars without strong infrared excesses associated with the cloud. In NGC 2023 (Fig. 1*b*), almost half the stars observed fall below the reddening line for early type stars, and therefore have infrared excesses. The color-color diagram for NGC 2068 is shown in Fig. 1*c*. Of the stars in NGC 2068 whose photometry is reported in Table 2, stars 5, 15, 19, and 30 have infrared excesses. For NGC 2068 the photometry of this paper was supplemented by the observations of Strom, Strom, and Vrba (1976), transformed to the photometric system of Neugebauer *et al.* (1979) using the relation of Frogel *et al.* (1978). Of the stars listed in Table 2 for which the colors of Strom *et al.* have been adopted, stars 4 and 2 have infrared excesses, while stars 20 and 53 have no evidence for infrared excesses. All stars in the three nebulae with identified

infrared excesses have this noted in Table 2.

The r photometry in NGC 2023 and 2068 is also presented in Table 2. Typically $r-K \sim 6$ mag in the two nebulae. The stars detected at only r or K, but not both, have upper or lower limits on $r-K$ generally consistent with $r-K \sim 6$ mag also.

b. Spectrophotometry

A spectrum of HD 200775 was obtained from 2.15 to 2.22 μm with $\Delta\lambda/\lambda = 1.7 \times 10^{-3}$. B γ was seen in emission from the star, with a strength of 2.3×10^{-12} erg cm^{-2} s^{-1}, and was unresolved with an instrumental resolution of 500 km s^{-1}. A 3 σ upper limit of 9×10^{-13} erg cm^{-2} s^{-1} was placed on other possible features in the spectrum.

Visual spectrophotometry was obtained for two stars in NGC 2023, stars H and C, and for one star in NGC 2068, star 20. The continua of these stars are extremely red, with $B-V = 1.6$, 1.8, and 2.2 mag respectively for 2023-H, 2023-C, and 2068-20. In 2023-H and 2023-C, H α is seen in emission from the star, while in 2068-20 both H α and H β are seen in emission. H α emission was previously identified in 2068-20 by Herbig and Kuhi (1963), who refer to this star as LkHα 304.

The hydrogen line emission in HD 200775, 2023-H, 2023-C, and 2068-20 must come from dense circumstellar shells or stellar winds. This is because the observed B γ and H α fluxes would predict optically thin free-free emission at radio wavelengths, far in excess of the 6 cm upper limits observed by Sellgren *et al.* (1983*b*) for these stars.

c. Variability

The observations reported here also include measurements at K, and sometimes H, made at different times, which can be used to investigate the variability of the stars observed in the three reflection nebulae. Both scan

magnitudes and photometric magnitudes obtained on different dates are presented in Table 3, as well as measurements by other observers when available. Only stars suspected of variability are included in this table.

In comparisons between different sets of photometry, with uncertainties ~ 0.05 mag, differences ≥ 0.15 mag were considered evidence of variability. When comparisons included scan magnitudes, which are uncertain by ≳ 0.3 mag, differences ≥ 0.75 mag were taken as evidence of variability. Only differences ≥ 0.75 mag were considered in establishing variability based on comparisons between the measurements presented in this paper and those of other observers, due to the possibility of unknown systematic differences among the various sets of data.

In NGC 7023, 6 stars are definitely identified as variable stars, based on photometry, while another 3 stars may be variable, based on scan magnitudes. Only the stars whose photometric magnitudes varied are identified as variable in Table 2*a*. These 6 stars varied by amounts ranging from 0.17 mag to 0.59 mag at K. The shortest time scale variability was seen in star D, where two photometric measurements on 1981 July 26, separated by 5 hours, differed by 0.15 ± 0.04 mag at *K*. HD 200775 (star A) was extensively observed at *J*, *H*, and *K*. Although this star is a Herbig Be star, stars which as a class are frequently variable, HD 200775 itself shows no evidence for infrared variability on time scales of hours, days, or years.

There is little evidence of variability ≥ 0.75 mag for the stars in NGC 2023. Star F appeared to vary by 1.4 mag at *K* from intercomparisons of different scans and photometry, but this is probably due to confusion (see footnote to Table 2*b*).

In NGC 2068 13 stars may have varied by ≥ 0.75 mag. Evidence for variability in stars 13 and 15 depends on single bright *K* measurements on the

Mt. Wilson 24 inch telescope, near the scan detection limit. The variation in stars 26a and 26b is likely due to confusion. The remaining 9 stars have been identified as variable in Table 2*c*. Star 14 varied 0.9 mag at *H*, based on measurements of other observers (Strom *et al.* 1975; Strom, Strom, and Vrba 1976). The other 8 stars varied by amounts ranging from 1.0 mag to 1.5 mag at *K*.

It is important to realize that while the fractions of stars found to vary in NGC 2023 and 2068 are less than in NGC 7023, the variability identified in NGC 7023 would have been missed if two sets of photometry separated by two years had not been available. Only one set of photometry exists in the other two nebulae, so that only variability $\geq$ 0.75 mag can be detected by comparison with scan magnitudes. The largest variation in the NGC 7023 photometry is smaller than this. This suggests that additional photometry in NGC 2023 and 2068 may uncover many more variable stars.

IV. DISCUSSION

a. Near infrared extinction in reflection nebulae

The reddening line in Fig. 1, $E(J-H)/E(H-K) = 1.90$, is derived from the value of Jones and Hyland (1980), measured on the AAO photometric system, by transforming it (Elias *et al.* 1983) to the photometric filters used here. A slightly different value, $E(J-H)/E(H-K) = 1.6$, has been obtained by Elias (1978c). Use of this reddening law instead would have no effect on the numbers of pre-main sequence stars found or on other conclusions of this paper.

Jones and Hyland (1980) have argued that the extinction curve in the near infrared, at least at J, H, K, and perhaps L (3.4 μm), is identical, within the uncertainties, in the general interstellar medium and in dense molecular clouds where large values of $R = A_V/E(B-V)$ have been reported. As discussed by Hyland (1981), the upper envelope of a $J-H$ *vs.* $H-K$ diagram for the stars observed towards a dark cloud is composed of background late type giants and stars without infrared excesses associated with the cloud, and therefore defines the near infrared extinction curve in the dark cloud. As can be seen from the good agreement between the reddening line of Jones and Hyland (1980) indicated in Fig. 1 and the observed upper envelopes to the color-color diagrams, the observed near infrared extinction curves in these three reflection nebulae support the hypothesis that a single near infrared extinction curve applies in a wide variety of physical environments.

While the near infrared extinction curve, as defined by $E(J-H)/E(H-K)$, is seen to be constant, the absolute value of the extinction is not known. Jones and Hyland (1980) fit a power law to their infrared extinction curve at J, H, K, and L, and find that at these wavelengths the extinction is consistent with a $\lambda^{-2.5}$ power law. This neglects the possibility of a grey component to the near

infrared extinction. Without more information on the absolute value of the near infrared extinction, it seems reasonable to adopt an extinction proportional to $\lambda^{-2.5}$, which implies that $E(J-H)/A_K$ = 2.06 and $E(H-K)/A_K$ = 1.05. These values are adopted throughout this paper.

b. The fraction of stars which are pre-main sequence

To determine the fraction of the total number of stars which are pre-main sequence (PMS), one must first restrict the sample so that it is complete and reasonably uniform. For this reason the only stars considered are those found in 2.2 μm scans in 1979 of NGC 7023, with a detection limit of 11.0 mag; 2.2 μm scans in 1981 January of NGC 2023, with a detection limit of 11.1 mag; and 2.2 μm scans in 1981 September and 1981 November of NGC 2068, with detection limits of 11.9 - 12.6 mag. These samples are estimated to be complete to K = 10.5 mag for NGC 7023 and 2023, and to 11.25 mag for NGC 2068. Stars below the scan completeness limit in each case are excluded from the sample. This provides uniform selections of stars in each nebula found from a set of scans with a single completeness limit, over a wide area. The small fraction of background stars, 10 - 25%, will be neglected in determining the characteristics of the stellar clusters associated with the reflection nebulae. The scan areas for these samples are 0.58, 1.39, and 1.26 pc^2 respectively for NGC 7023, 2023, and 2068. The stars included in the sample are all stars in Table 2 brighter than the scan completeness limit, except for stars 40 and 42 in NGC 7023, stars L and N in NGC 2023, and stars 1, 2, 3, 4, 5, 6, and 55 in NGC 2068. Note that star D in NGC 7023 is included in the sample, since it was brighter than the scan completeness limit when first discovered (Table 3*a*).

Some of the stars which are listed in Table 2*a* are also identified with variable or suspected variable stars found by Rosino and Romano (1962). When suitable observations exist at both wavelengths, all of the stars known to vary in

NGC 7023 are seen to be variable at both visual and near infrared wavelengths. The study of Rosino and Romano (1962), which is more extensive in its time coverage, shows that the stars in NGC 7023 vary irregularly with time, which is characteristic of nebular variables such as T Tauri stars. The time coverage of the observations reported in Table 3 is not complete enough to establish the nature of the variability of the stars observed in the three reflection nebulae. The good correspondence between variability at K and identification as an irregular variable at visual wavelengths in NGC 7023, however, suggests that it is a reasonable assumption that infrared variability indicates that a star is a PMS star physically associated with the cloud.

The variety of observations described above provide an approach to estimating the number of young PMS stars in the reflection nebula fields. One method of identifying a PMS star is by its variability. The presence of an infrared excess or Hα emission, both of which are indicators of circumstellar shells which surround PMS stars (Strom, Strom, and Grasdalen 1975), can also be used to identify PMS stars. These three characteristics are noted in Table 2 for each star that is known to show them.

In the sample which has been restricted so as to be complete, 6 out of 11 stars in NGC 7023 are identified as PMS stars, using the criteria of variability, infrared excesses, and hydrogen line emission. Similarly 5 out of 8 stars in NGC 2023, and 9 out of 26 stars in NGC 2068, are PMS stars. Many of the irregular variables in NGC 7023 show no evidence of an infrared excess in the color-color diagrams, but the observations of this paper are not sufficient to determine the variability of most stars in NGC 2023 and 2068. Thus these numbers set lower limits to the fraction of the detected stars which are PMS stars.

All the stars in NGC 2023 and 2068 cannot be PMS, since star A in NGC 2023 is classified B1.5V (Abt and Levato 1977), and stars 31 and 36 in NGC 2068 are

classified ~ B3V (Sellgren *et al.* 1983*b*). These stars, in addition to star 33 in NGC 2068 (B2II-III; Strom *et al.* 1975) appear to be normal stars with no evidence of variability, H α emission, or infrared excesses. The earliest type star in NGC 7023, HD 200775, is a PMS star (Strom *et al.* 1972), with an infrared excess and H α emission, although it is not photometrically variable (section IIIc; Breger 1974). The remaining stars in NGC 7023 are either PMS or unclassified, so it is possible that no stars in NGC 7023 have reached the main sequence yet.

c. The luminosity function and spatial distribution of the stars

The spatial distibution of stars in the three nebulae is shown in Fig 2. The surface density of stars can be seen to be highest near the cluster centers, which in NGC 2068 and NGC 7023 is consistent with the positions of the visual illuminating stars of the reflection nebulae, star 33 and star A respectively. In NGC 2023 the visual illuminating star, star A, does not appear to be at the center of the cluster, so the NGC 2023 cluster center is assumed to be the mean position of the stars, 60" east and 67" south of star A. The radial distribution of stars from the cluster center for each nebula appears to follow a power law of the form $N(R) \sim R^x$, where $N(R)$ is the total number of stars inside of a circle of projected radius R. Power laws were found for NGC 7023, 2023, and 2068 of $x = 0.94 \pm 0.28$, $x = 0.83 \pm 0.33$, and $x = 0.89 \pm 0.10$, respectively, using only the stars in the samples which have been limited so as to be complete. These are all consistent with $x = 1$, or $N(R) \sim R$. This distribution corresponds to a surface density of stars $\sigma(R) \sim R^{-1}$, if σ is uniform. If the clusters are spherically symmetric, the observed distribution $N(R)$ also corresponds to a volume density of stars $n(r) \sim r^{-2}$, where r is the true radius from the cluster center.

The distribution in apparent magnitude can also be determined from the observations of the three reflection nebulae. The cumulative number of stars

$N(K)$ *vs.* observed K magnitude is shown in Fig. 3 for NGC 2068, where the largest number of stars were found. This figure includes data from all the K scans, up to a K magnitude 0.5 mag brighter than each scan detection limit, scaled to account for the different surface densities of stars sampled by different scans, and weighted by the uncertainties due to counting statistics in each magnitude bin. The assumption is made that $N(K)$ is independent of position in the nebula. The observed distribution suggests a form for the observed luminosity function of $N(K) \sim 10^{\gamma K}$. In NGC 2068 the observed value of γ is $\gamma = 0.29 \pm 0.03$. In NGC 7023 and NGC 2023, the number of stars is smaller and the uncertainties therefore larger, but consistent results are found of $\gamma = 0.24 \pm 0.05$ and $\gamma = 0.21 \pm 0.09$ respectively.

The relationship between the observed luminosity function, $N(K)$, and the intrinsic luminosity function $n(K_0)$, where K_0 is the absolute K magnitude, and $n(K_0)$ is the number of stars in a magnitude interval dK_0, depends on a number of characteristics of the cluster, such as the spatial distribution of stars and dust. However, as long as $n(K_0)$ is everywhere the same in the nebula, then for $N(K) \sim 10^{\gamma K}$, as was found for the three reflection nebulae, $n(K_0) \sim 10^{\gamma K_0}$. This also assumes that any cutoff or change in slope in $n(K_0)$ does not occur within the observed magnitude range of the sample from which $N(K)$ was derived. For the finite number of stars observed here, it is possible that differences in the reddening of individual stars will alter the slope of the observed luminosity function. Since the reddening deduced from the color-color diagrams (Fig. 1), however, is typically only $A_K \sim 0.5$ mag, and at most $A_K \sim 1$ mag, while the observed luminosity function is determined over 4 magnitudes at K, the reddening of individual stars should have little effect on the slope of the intrinsic luminosity function derived from the observations.

To convert the observed luminosity function $n(K_0)$ into a mass function one needs to know the relation between absolute K magnitude and stellar mass. This relation is completely unknown for the PMS stars, which comprise at least 30% of the stars in NGC 2068. A simple-minded approach is to assume the mass-luminosity relation for PMS stars has the same slope as the main sequence mass-luminosity relation. This assumption is more or less equivalent to assuming that the ratio of PMS to main sequence stellar luminosity is approximately independent of spectral type within a given cluster. This simplistic assumption appears to be a fair approximation to published 2.2 μm observations of PMS stars in other regions, for a wide range in spectral types, and to the H-R diagrams derived by Cohen and Kuhi (1979) for PMS stars, which show the PMS stars in a cluster to generally lie in a band on the H-R diagram parallel to and above the main sequence.

A second problem in estimating the mass function is that the observed luminosity function contains contributions from both PMS and main sequence stars. For this the simplifying assumption is made that the fraction of PMS stars is the same at each observed luminosity. While an increasing fraction of PMS stars with decreasing luminosity might be expected to be more appropriate, a constant fraction is consistent with the observations and more complicated expressions do not seem warranted.

With these two simple-minded assumptions, then, the main sequence mass-luminosity relation combined with the derived cluster luminosity function can be used to estimate the cluster mass function. The main sequence mass-luminosity relation, for main sequence stars, is approximately $L_K \propto M^{2.4}$, where L_K is the luminosity at 2.2 μm and M is the mass. Since $L_K \propto 10^{-0.4K_0}$, the luminosity function $n(K_0) \sim 10^{\gamma K_0}$ implies a power law distribution with mass, $n(M) \sim M^{\beta}$, where β is the power law index for mass, and $n(M)$ is the number of

stars in a logarithmic mass interval $d\log M$. From the observed luminosity function in NGC 2068, with the above assumptions, one derives a mass power law index of β = -1.8 ± 0.2. This is not significantly different from the standard Salpeter mass power law index β = -1.35, and agrees well with the range of mass power law indices observed in associations of T Tauri stars, β = -1.35 to -2.9 (Cohen and Kuhi 1979).

d. The stellar density and star formation efficiency

Norman and Silk (1980) have described a scenario for star formation in dark clouds where stellar winds from T Tauri stars in the clouds provide the energy input for further formation of T Tauri stars. This theory explains the noncoeval star formation in dark clouds suggested by the observed spread of ages of T Tauri stars in the same cloud. Norman and Silk argue that densities of T Tauri stars above a critical density of 10 pc^{-3} are needed for this mechanism to work, and so it is of interest to calculate the density of T Tauri stars in NGC 7023, 2023, and 2068.

The spatial densities of the stars in NGC 7023, 2023, and 2068 can be estimated in two ways. First, one can assume spherical symmetry. Second, one can estimate the extent of the cloud along the line of sight by a comparison of the gas density n_H and the gas column density N_H, and then assume that the stars and gas are coextensive. The gas density and gas column density can be obtained from molecular line observations.

For NGC 7023, the column density of ^{13}CO is 1×10^{16} cm^{-2} (Loren, VandenBout, and Davis 1973), and the hydrogen density is $\sim 10^3$ cm^{-3} (Whitcomb *et al.* 1981). For a ^{13}CO to hydrogen ratio of 2×10^{-6} (Dickman 1975), the approximate line of sight distance is ~ 2 pc. For NGC 2023, the column density of ^{13}CO is 1×10^{17} cm^{-2} (Milman *et al.* 1975), and the hydrogen density implied by the C II observations (Pankonin and Walmsley 1978) is $\sim 5 \times 10^4$ cm^{-3}, so that

the line of sight distance is ~ 0.4 pc. For NGC 2068 the column density of ^{13}CO is 6×10^{16} cm^{-2} (Milman *et al.* 1975), and the hydrogen density is 4×10^4 cm^{-3} (Loren 1981), implying a line of sight distance of ~ 0.2 pc. The scan areas in NGC 7023, 2023, and 2068, for the sample which has been limited so as to be complete, are respectively 0.58, 1.4, and 1.3 pc^2, and contain 6, 5, and 9 known PMS stars. Assuming spherical symmetry, the number densities of PMS stars are ~ 10, 3, and 6 pc^{-3} in NGC 7023, 2023, and 2068. Adopting instead the line of sight distances from a comparison of N_H and n_H gives PMS stellar densities of ~ 6, 10, and 30 pc^{-3}, respectively. The actual densities of PMS stars are likely higher, since there are probably PMS stars fainter than the scan limits, and also the methods of this paper for identifying PMS stars provide only lower limits to their numbers. Thus, the densities of PMS stars in these three regions are comparable to the densities required by the model of Norman and Silk (1980) to maintain continuing low mass star formations in dark clouds.

A comparison of the column densities of stars and gas does not depend on uncertain estimates of the line of sight extent of the stellar cluster. An effective star formation efficiency is then the ratio of the mass per unit area in stars to the combined mass per unit area of stars plus gas. The most conservative estimate is to assume all stars whose spectral types are unknown are PMS stars, since these stars are less massive than a main sequence star of the same luminosity; to make no correction for possible reddening of the stars; and to include only stars already found in the scans limited so as to be complete. This estimate will therefore be a strong lower limit, especially since there are presumable fainter stars which contribute considerably to the mass of the cluster. The estimates of stellar mass contained in the areas scanned in NGC 7023, 2023, and 2068 are respectively 10, 10, and 30 $M_\odot$ under these assumptions. The masses are ~ 10-40% higher if stars in Table 2 below the scan

completeness limits are included. The gas mass per unit area is found from the ^{13}CO column densities above. The observed lower limits to the effective star formation efficiencies in NGC 7023, 2023, and 2068 are ~ 30%, 2%, and 10% respectively. These efficiencies would be ~ 50%, 3%, and 20% if stars not known to be PMS stars were assumed to lie on the main sequence. While the conversion of gas into stars in NGC 7023 appears to be relatively efficient, this reflects in part the fact that the NGC 7023 stellar cluster is not at a molecular peak. In all three nebulae the molecular gas extends over a larger area than does the stellar cluster, so that the total star formation efficiency for the cloud is much lower than the local efficiency within the cluster. It would be extremely interesting to examine how the efficiency of star formation varied with radius in the stellar cluster. This comparison, however, must await molecular line observations with higher resolution than the angular resolution of ~ 3' presently available.

V. SUMMARY

The properties of stars found in 2.2 μm scans of reflection nebulae have been investigated, and several conclusions about the nature of the stars can be drawn:

1. The number of stars found is much larger than the number of expected background stars, implying that almost all of the stars found are in fact associated with the cloud.

2. Consideration of a number of indicators of the pre-main sequence (PMS) nature of stars, such as hydrogen line emission, infrared excesses, or irregular variability, shows that at least 30-60 % of the stars found in these stellar clusters have not reached the main sequence.

3. The observed variability indicates that at least 50 % of the stars in NGC 7023 are PMS objects, but most of the nebular variable stars in NGC 7023 do not have identifiable infrared excesses. This suggests that identification of young stars by their infrared excesses, as was done in NGC 2023 and 2068, severely underestimates the true numbers of PMS stars.

4. The observed luminosity function of the young stellar clusters is found to be $N(K) \sim 10^{\gamma K}$, with $\gamma = 0.29 \pm 0.03$.

5. The star formation efficiency local to the stellar cluster is found to be at least 30 % in NGC 7023, although the overall efficiency for the entire dark cloud is lower.

6. The spatial densities of PMS stars are found to be $\gtrsim$ 3-30 pc^{-3}, comparable to values required by the model of Norman and Silk (1980) to maintain constant low mass star formation in the dark clouds.

7. The surface density of the stars in all three nebulae decreases as the inverse of the projected radius from the cluster center. This, if spherically symmetric, corresponds to a volume density which depends on the true radius as r^{-2}.

Acknowledgements

I thank the staff of Mt. Wilson Observatory for their hospitality, and my night assistants M. Deak, J. Frazer, and H. Lanning. Additional assistance with the observations was provided by M. Ashley, G. Berriman, E. Grossman, J.H. Lacy, M. Malkan, P. McGregor, J.E. Nordholt, A.J. Rosenthal, B.T. Soifer, S.E. Whitcomb, and R.L. White. I especially thank S.E. Whitcomb, who contributed significantly to the initial observations of stars in NGC 7023. I thank M.W. Werner and A. Bentley for obtaining photometry of HD 200775 for me; S. E. Whitcomb for obtaining a 0.8 μm photograph of NGC 7023; J.G. Cohen for obtaining visual spectra of 3 stars in NGC 2023 and 2068; M. Malkan for obtaining SIT frames in NGC 2023 and 2068 and helping with their reduction; T. Jones for providing model predictions of background star counts; Yerkes Observatory and the University of Wyoming for the use of their telescope facilities; G. Grasdalen for a careful reading of the manuscript; and J. Elias for communication of unpublished data. Useful discussions were held with J.G. Cohen, S.E. Whitcomb, J. Elias, B.T. Soifer, and G. Neugebauer. This research was supported by grants from NASA and NSF.

REFERENCES

Abt, H.A. and Levato, H. 1977, *Pub. Astron. Soc. Pac.*, **89**, 797.

Breger, M. 1974, *Ap. J.*, **188**, 53.

Cohen, M. and Kuhi, L. V. 1979, *Ap. J. Suppl.*, **41**, 743.

Dickman, R.L. 1975, Ph.D. thesis, Columbia University.

Elias, J.H. 1978*a*, *Ap. J.*, **223**, 859.

Elias, J.H. 1978*b*, *Ap. J.*, **224**, 453.

Elias, J.H. 1978*c*, *Ap. J.*, **224**, 857.

Elias, J.H., Frogel, J.A., Matthews, K., and Neugebauer, G. 1982, *A. J.*, **87**, 1029.

Elias, J. H., Frogel, J. A., Hyland, A. R., and Jones, T. J. 1983, submitted to *Astron. J.*

Elvius, A. and Hall, J.S. 1967, *Interstellar Grains*, eds. J.M. Greenberg and T.P. Roark

Frogel, J.A., Persson, S.E., Aaronson, M., and Matthews, K. 1978, *Ap. J.*, **220**, 75.

Grasdalen, G.L., Strom, K.M., and Strom, S.E. 1973, *Ap. J. (Letters)*, **184**, 53.

Herbig, G.H. and Kuhi, L.V. 1963, *Ap. J.*, **137**, 398.

Herbig, G.H. and Rao, N.K. 1972, *Ap. J.*, **174**, 401.

Hyland, A.R. 1981, in IAU Symposium **96**, *Infrared Astronomy*, eds. C.G. Wynn-Williams and D.P. Cruikshank (Reidel, Dordrecht).

Hyland, A. R., Jones, T. J., and Mitchell, R. M. 1982, *M. N. R. A. S.*, **201**, 1095.

Jones, T.J., and Hyland, A.R. 1980, *M. N. R. A. S.*, **192**, 359.

Jones, T.J., Ashley, M., Hyland, A.R., and Ruelas-Mayorga, A. 1981, *M. N. R. A. S.*, **197**, 413.

Kent, S.M. 1979, *Pub. Astron. Soc. Pac.*, **91**, 394.

Lee, T.A. 1968, *Ap. J.*, **152**, 913.

Loren, R.B., VandenBout, P.A., and Davis, J.H. 1973, *Ap. J. (Letters)*, **185**, 67.

Loren, R. B. 1981, *A. J.*, **86**, 69.

Lynds, B. T. 1962, *Ap. J. Suppl.*, **7**, 1.

Milman, A.S., Knapp, G.R., Kerr, F.J., Knapp, S.L., and Wilson, W.J. 1975, *A. J.*, **80**, 93.

Neugebauer, G., Oke, J.B., Becklin, E.E., and Matthews, K. 1979, *Ap. J.*, **230**, 79.

Norman, C., and Silk, J. 1980, *Ap. J.*, **238**, 158.

Oke, J.B., and Gunn, J.E. 1982, *Pub. Astron. Soc. Pac.*, **94**, 586.

Pankonin, V. and Walmsley, C.M. 1978, *Astr. Ap.*, **67**, 129.

Romano, G. 1975, *Ap. Space Sci.*, **33**, 487.

Rosino, L., and G. Romano 1962, Contr. Asiago Obs. *127.*

Sellgren, K., Soifer, B.T., Neugebauer, G. and Matthews, K. 1983*a*, *Pub. Astron. Soc. Pac.*, to be published.

Sellgren, K., Becker, R., Pravdo, S.H., and White, R.L. 1983*b*, in preparation.

Strom, K.M., Strom, S.E., Carrasco, L., and Vrba, F.J. 1975, *Ap. J.*, **196**, 489.

Strom, K.M., Strom, S.E., and Vrba, F.J. 1976, *A. J.*, **81**, 308.

Strom, S.E., Strom, K.M., Yost, J., Carrasco, L., and Grasdalen, G. 1972, *Ap. J.*, **173**, 353.

Strom, S.E., Strom, K.M., and Grasdalen, G.L. 1975, *Ann. Rev. Astron. Ap.*, **13**, 187.

Thuan, T.X., and Gunn, J.E. 1976, *Pub. Astron. Soc. Pac.*, **88**, 543.

Viotti, R. 1969, *Mem. Soc. Astr. Ital.* **40**, 75.

Vrba, F.J., Strom, K.M., Strom, S.E., and Grasdalen, G.L. 1975, *Ap. J.*, **197**, 77.

Weston, E.B. 1953, *A. J.*, **58**, 48.

Whitcomb, S.E., Gatley, I., Hildebrand, R.H., Keene, J., Sellgren, K., and Werner, M.W. 1981, *Ap. J.*, **246**, 416.

Table 1

λ (μm)	scan limits α^a	δ^a	$m_{lim}{}^b$	date	θ^c (")	spacing^d (")	scan direction^e
			a. Scans of NGC 7023				
1.65	23E-23W	23S-158S	11.3	1979AUG22	11	20	ra
	23E-23W	23N-203N					
2.2	158E-113W	203N-203S	11.0	1979AUG23-24	11	20	ra
	113W-158W	23N-113S					
2.2	113W-158W	23N-203N	11.0	1979SEP03	11	32	ra
	113W-158W	113S-203S					
	23E-68E	23S-68N					
2.2	158E-203E	203S-203N	11.7	1981JUL30-AUG01	11	23	ra
	203W-158W	203S-113N					
	203E-316E	68S-23N					
	203W-312W	68S-23N					
2.2	129E-424E	15N-176N	12.0	1981NOV15-21	16	129	dec
	462W-301W	157S-4N					
	81W-81E	81S-81N					
	148E-172E	214S-52S					
			b. Scans of NGC 2023				
2.2	250E-250W	273N-200S	11.1	1981JAN05-08	20	70	dec
2.2	50W-50E	100S-100N	11.1	1981JAN07	10	70	dec
2.2	136E-310E	23S-68N	11.0	1981FEB01	11	36	ra
	226W-307W	23S-68N					
2.2	*f*	*f*	*f*	1981OCT20	19	344	ra
			c. Scans of NGC 2068				
1.65	0W-382W	382S-67N	11.0	1981FEB03-05	19	344	ra
2.2	0W-382W	29N-191N	10.6	1981FEB06-12	19	344	ra
	382W-764W	48S-191N					
2.2	50E-50W	0N-100N	12.6	1981SEP16-17	10	60	dec
2.2	50E-250E	0N-100N	11.9	1981SEP17-19	20	60	dec
2.2	0W-382W	0S-181S	8.7	1981OCT13-14	19	344	ra
2.2	90E-0E	100S-200S	11.9	1981NOV11	20	55	dec
2.2	161E-161W	0S-322S	12.0	1981NOV17-20	16	129	dec
	0W-322W	161N-0N					
	322E-161E	0S-161S					
	161E-81E	205N-44N					

(a) Offset in arcsec from HD 200775 = star A in NGC 7023, from HD 37903 = star A in NGC 2023, and from HD 38563-N = star 33 in NGC 2068.

(b) Faintest magnitude detectable

(c) Diameter of diaphragm

(d) Spacing between source and sky positions

(e) The scan technique used was a raster scan covering the area indicated. The direction of the scan lines was along the line connecting the source and sky positions.

(f) Specific search for a particular star rather than a systematic scan.

Table 2a

Stars found in 2.2 and 1.65 μm scans of NGC 7023

name	K[a]	H[a]	J[a]	$\sigma(K)$[b]	$\sigma(H)$[b]	$\sigma(J)$[b]	$\Delta\alpha$[c]	$\Delta\delta$[c]	Δpos[d]	Other designations[e]	PMS[f]
42	10.1						472W	191S	5		
41	10.7						442W	73S	5		
40	7.7						416W	77S	5		
39	12.0						349W	8S	5		
36	11.05	11.51	12.21			0.06	220W	6S	5	S3	
F	10.74	10.94	11.49			0.08	158W	140S	3		
I	10.35	10.74	11.72			0.09	138W	34N	3	S4	
J	8.97	9.62	10.67			0.07	59W	52N	3	R2, S5, *g*	I,V
K	9.36	9.80	10.64	0.06		0.09	34W	49N	3		
E	10.88	11.30	12.22			0.10	5W	88S	3	R3, S2, LkHα 425	H,V
A	4.62	5.42	6.09				0E	0N	3	HD 200775, MWC 361, BD +67° 1263	H,I
L	9.30	9.64	10.49				7E	106N	3	SX Cep	V
M	11.01	11.37	12.13			0.07	25E	75N	3	S6	
N	10.29	10.76	11.65	0.06		0.11	35E	192N	3	R5, S8	V
D	10.53	10.68	11.36			0.06	36E	11S	3	RS3, HZ Cep	V
B	9.61	9.77	10.42			0.06	46E	183S	3		
C	10.25	10.84	11.64			0.09	54E	64S	3	R6, S1, FU Cep, LkHα 427, *h*	H,I,V
29	11.7						77E	23S	5		
44	11.8						89E	0N	5		
10	11.7						99E	129S	3		
S	12.44	12.72	14.37	0.11	0.06	0.27	127E	50S	3		
O	10.40	10.86	11.74			0.07	135E	109N	3	S11	
45	12.0						148E	194S	5		
T	11.23	11.47	12.36			0.07	173E	32S	3		
46	10.9						177E	227S	5		
34	11.2						192E	150S	3		
30	9.47	10.36	12.20			0.07	200E	50N	3		
47	10.9						297E	215S	5		
37	11.69	12.30	13.35			0.11	317E	77S	5		
38	11.52	12.13	13.44			0.11	343E	62S	5		

(a) Magnitudes given to 0.1 mag are scan magnitudes, and are uncertain by ≳ 0.3 mag. Magnitudes given to 0.01 mag are photometric magnitudes.

(b) Uncertainties are ± 1σ, and include both photometric and statistical uncertainties. The uncertainties are given only when greater than 0.05 mag for photometry; no uncertainties are given for scan magnitudes.

(c) Offset in arcsec from HD 200775 = star A.

(d) Uncertainty in arcsec of stellar position.

(e) R and RS are variable and suspected variable stars found by Rosino and Romano (1962). S are very red stars (V–[1 μm] > 3 mag) identified by Strom *et al.* (1972).

(f) Indicators used to determine which stars are probable pre-main sequence (PMS) stars. H = hydrogen line emission, I = infrared excess, V = variable.

(g) Close visual binary (Romano 1975). Photometry includes both components.

(h) T Tauri star, also known as HRC 304 and Perrine B in the T Tauri star catalogue of Herbig and Rao (1972).

Table 2b

Stars found in 2.2 μm scans of NGC 2023

name	K^a	H^a	J^a	r^b	$\sigma(K)^c$	$\sigma(H)^c$	$\sigma(J)^c$	$\Delta\alpha^d$	$\Delta\delta^d$	Δpos^e	Other designations^f	PMS^g
M	10.86	10.95	11.32					156W	251S	4		
J	10.70	11.10	12.01				0.06	151W	94N	4		
E	11.15	11.41	12.12	16.6			0.06	55W	115S	3		
C	8.42	9.74	11.31	16.1				30W	76S	3	S108	H,I
D	10.32	12.79	14.37			0.06	0.21	20W	105S	3		I
A	7.32	7.34	7.44					0E	0N	3	HD 37903, BD -02° 1345	
B	9.92	10.37	11.26	14.9				29E	28S	3	S101	
I	10.31	11.82	13.51				0.12	60E	51S	4		I
G	10.83	11.38	12.12	17.2			0.06	62E	125S	3		I
205				16.4				74E	126S		S106	
217				17.5				89E	44S		*h*	
218				17.3				90E	34S		*h*	
219				17.5				94E	32S		*h*	
F	9.26	10.74	12.47					95E	34S	3	*h*	I
211				18.9				98E	81S			
220				17.6				101E	26S		*h*	
H	7.43	8.13	9.01					133E	65S	4	S105	H,I
K	10.12	10.99	12.91				0.07	212E	181S	4		
L	9.27	9.77	11.05					527E	39N	4		
N	8.6							667E	15N	10		

(a) K, H, and J magnitudes given to 0.1 mag are scan magnitudes, and are uncertain by $\gtrsim$ 0.3 mag. K, H, and J magnitudes given to 0.01 mag are photometric magnitudes.

(b) r magnitudes are photometric magnitudes, with typical uncertainties of 0.2 mag.

(c) Uncertainties at K, H, and J are $\pm$ 1σ, and include both photometric and statistical uncertainties. These uncertainties are given only when greater than 0.05 mag for photometry; no uncertainties are given for scan magnitudes.

(d) Offset in arcsec from HD 37903 = star A.

(e) Uncertainty in arcsec of stellar position, given only for stars measured in infrared.

(f) S = stars observed by Strom *et al.* (1975).

(g) Indicators used to determine which stars are probable pre-main sequence (PMS) stars. H = hydrogen line emission, I = infrared excess, V = variable.

(h) The region containing stars F, 217, 218, 219, 220, S102, S103, S104, and S110 is rather confused. Probably S104 = 220; S110 = 218 + 219; F = some or all of 217, 218, 219, and 220; and F = some or all of S102, S103, S104, and S110.

Table 2c

Stars found in 2.2 μm and 1.65 μm scans of NGC 2068

name	K^a	H^a	J^a	r^b	$\sigma(K)^c$	$\sigma(H)^c$	$\sigma(J)^c$	$\Delta\alpha^d$	$\Delta\delta^d$	Δpos^e	Other designations^f	PMS^g
1	9.0							649W	0N	10		
2	9.6							611W	29S	10	LkHα 298, SSV 51	H,I
3	10.1							406W	96N	10	SSV 54	
4		10.6						401W	344S	10	M78/111, SSV 48	I,V
5	7.98	9.08	10.46					392W	110S	10	LkHα 300, SSV 49	H,I
6	10.2							344W	181N	10		
7	11.6							326W	48S	8		
8	10.8							298W	20N	4	SSV 52	
9	11.8							286W	113N	4		
10	11.2							258W	24N	4		
11	11.1							242W	145S	4	M78-1	V
135				14.7				228W	308S			
12	11.1			16.4				218W	101N	4		
13	10.6			19.0				203W	77N	4	SSV 7	
14	10.0			16.1				177W	153S	4	M78/109, M78-2, SSV 13	V
15	11.91	12.75	13.72	18.0	0.09	0.09	0.25	173W	61N	4		I
133				17.5				163W	214N		SSV 16	
17	9.76	10.49	12.05					156W	81N	3	M78-4, SSV 6	V
16	11.2			17.5				151W	63S	8	M78-3, SSV 8	V
18	11.4							141W	226S	4		
19	9.67	11.06	13.18	16.9				133W	64N	3	M78-5, SSV 2	I,V
20	9.8	10.6		15.0				119W	242S	4	LkHα 304, M78/108, SSV 11	H,V
21	11.8			18.2				109W	81S	4		
22	12.0							105W	93N	4		
23	11.8							105W	161N	8		
24	11.1							93W	24N	4	SSV 5	
25	11.4							77W	81N	4		
26-1				20.3				69W	6S			
26a	10.15	10.48	11.51					67W	29S	3	M78/106, *h*	
26b	10.62	11.00	11.91					66W	18S	3	M78/107, *h*	
26-2				16.3				63W	17S			
26-3				15.1				61W	25S			
26-4				15.9				59W	10S			

(a) K, H, and J magnitudes given to 0.1 mag are scan magnitudes, and are uncertain by $\gtrsim$ 0.3 mag. K, H, and J magnitudes given to 0.01 mag are photometric magnitudes.

(b) r magnitudes are photometric magnitudes, with typical uncertainties of 0.2 mag.

(c) Uncertainties at K, H, and J are $\pm$ 1σ, and include both photometric and statistical uncertainties. These uncertainties are given only when greater than 0.05 mag for photometry; no uncertainties are given for scan magnitudes.

Table 2c continued

name	K^a	H^a	J^a	r^b	$\sigma(K)^c$	$\sigma(H)^c$	$\sigma(J)^c$	$\Delta\alpha^d$	$\Delta\delta^d$	Δpos^e	Other designations^f	PMS^g
119				16.2				52W	155S			
27	12.6							35W	70N	6		
28	12.4							35W	50N	6		
29	12.3							33W	5N	3		
30	8.63	10.74	12.61	18.1			0.06	27W	274S	4	M78-10, SSV19	I
31	8.23	8.39	8.61					20W	48S	4	HD 38563-S, M78-8, *i*	
32	8.94	9.35	10.38	14.2				17W	6N	3	M78/104	
33	6.82	7.03	7.59					0E	0N	3	HD 38563-N, M78-9, SSV 1, *i*	
34	10.2			16.4				5E	10N	6		
35	11.6			18.0				5E	98S	3		
36	8.66	9.05	9.65					8E	166S	4	HD 38563-C, M78-11, SSV 9, *i*	
37	12.0							10E	28N	3		
38	10.8							32E	109N	3		
39	11.2							32E	218S	8		
40	10.3			18.2				41E	78S	3	M78-12	V
42	11.4			17.2				41E	3N	3		
108				18.3				42E	126S			
41	11.9			14.1				43E	49S	6		
43	11.5			20.9				44E	25S	3		
44	11.4			17.4				45E	105S	5		
45	11.4							54E	31N	3		
113				17.2				57E	61S			
46	12.0							73E	84N	8		
47	10.3	11.0		13.1				83E	41S	5	LkHα 306, M78-13, SSV 3	H,V
48	11.6							105E	93S	4		
49	11.4							117E	49N	8		
50	10.2							133E	322S	4		
51	11.4							137E	290S	4		
107				17.3				144E	157S			
52	10.9							178E	13S	4	SSV 18	
53	9.7	10.3						204E	15N	4	SSV 17	
54	11.8							240E	85S	10		
55		10.6						363E	315S	10		

(d) Offset in arcsec from HD 38563-N = star 33.

(e) Uncertainty in arcsec of stellar position, given only for stars measured in infrared.

(f) Designations beginning M78/ and M78- refer to stars found optically and by infrared searches respectively by Strom *et al.* (1975). Designations beginning SSV refer to stars found in infrared searches by Strom, Strom, and Vrba (1976).

(g) Indicators used to determine which stars are probable pre-main sequence (PMS) stars. H = hydrogen line emission, I = infrared excess, V = variable.

(h) The stars 26a and 26b together are also known as M78-6 and SSV 4.

(i) HD 38563 also known as BD +00° 1177

Table 3a

Variability in NGC 7023

Name	K^a	$\sigma(K)^b$	H^a	$\sigma(H)^b$	date[c]
36	9.50				1972
36	11.0				1981JUL31
36	11.0				1981AUG01
36	11.0				1981AUG01
36	11.05		11.51		1981NOV15
J	9.2				1979AUG23
J	9.4				1979AUG24
J	9.3				1979AUG24
J	9.56		10.08		1979SEP02
J	8.97		9.62		1981JUL27
J	9.1				1981NOV20
K			10.0		1979AUG22
K	9.4				1979AUG23
K	10.2				1979AUG24
K	9.40		9.84		1979SEP02
K	9.36	0.06	9.80		1981JUL27
K	9.6				1981NOV19
E	10.50				1972
E			11.3		1979AUG22
E	10.5				1979AUG23
E	10.7				1979AUG24
E	10.60		11.13		1979SEP02
E	10.88		11.30		1981JUL26
E	11.4				1981NOV19
L			10.1		1979AUG22
L	9.4				1979AUG23
L	9.5				1979AUG23
L	9.6				1979AUG23
L	9.6				1979AUG24
L	9.55		10.05		1979SEP02
L	9.30		9.64		1981JUL27

Table 3a continued

Variability in NGC 7023

Name	K^a	$\sigma(K)^b$	H^a	$\sigma(H)^b$	date[c]
M	11.0				1979AUG23
M	11.0				1979AUG24
M	10.99		11.29		1979SEP02
M			11.42		1981JUL29
M	11.01		11.37		1981JUL30
M	11.8				1981NOV19
D	10.2				1979AUG23
D	10.04		10.30		1979SEP02
D	10.2				1979SEP03
D	10.38		10.56		1981JUL26
D	10.53		10.68		1981JUL26
D	10.3				1981NOV19
C	10.50				1972
C	9.9				1979AUG23
C	10.1				1979AUG24
C	10.1				1979AUG24
C	10.08		10.68		1979SEP02
C	10.25		10.84		1981JUL28
C	10.4				1981NOV19
T	11.19		11.49		1979SEP03
T	11.23		11.47		1981JUL29
T	11.0				1981JUL30
T	11.9				1981NOV16

(a) K and H magnitudes given to 0.1 mag are scan magnitudes, and are uncertain by $\gtrsim$ 0.3 mag. K and H magnitudes given to 0.01 mag are photometric magnitudes.

(b) Uncertainties are $\pm$ 1σ, and include both photometric and statistical uncertainties. The uncertainties are given only when greater than 0.05 mag for photometry; no uncertainties are given for scan magnitudes.

(c) Dates for which the year only is given are for observations by other observers, and refer to the year in which the data were published. The supplemental observations were taken from Strom *et al.* (1972).

Table 3b

Variability in NGC 2023

Name	K^a	$\sigma(K)^b$	date[c]
F	8.65	0.28	1975
F	8.5		1981JAN06
F	8.7		1981JAN06
F	9.9		1981FEB01
F	9.26		1981SEP15

(a) K magnitudes given to 0.1 mag are scan magnitudes, and are uncertain by $\gtrsim$ 0.3 mag. K magnitudes given to 0.01 mag are photometric magnitudes.

(b) Uncertainties are $\pm$ 1σ, and include both photometric and statistical uncertainties. The uncertainties are given only when greater than 0.05 mag for photometry; no uncertainties are given for scan magnitudes.

(c) Dates for which the year only is given are for observations by other observers, and refer to the year in which the data were published. The supplemental observations were taken from Strom *et al.* (1975), and are the sum of the contributions of S102, S103, S104, and S110 (see footnote to Table 2*b*).

Table 3c

Variability in NGC 2068

Name	K^a	$\sigma(K)^b$	H^a	$\sigma(H)^b$	date[c]
4	10.50	0.25			1975
4	9.09	0.1	10.25	0.1	1976
4			10.6		1981FEB04
11	9.8				1975
11	11.1				1981NOV20
13	10.80	0.25	11.54	0.25	1976
13	10.2				1981FEB12
13	11.0				1981NOV20
14	9.40	0.2	9.70	0.2	1975
14	9.91	0.1	10.59	0.25	1976
14	10.0				1981NOV20
15	9.3				1981FEB12
15	11.91	0.09	12.75	0.09	1981NOV19
15	12.0				1981NOV20
16	9.7				1975
16	11.07	0.25			1976
16	11.2				1981NOV18
16	11.2				1981NOV18
17	9.0				1975
17	10.08	0.1	11.04	0.25	1976
17	9.9				1981FEB06
17	9.6				1981FEB12
17	9.9				1981FEB12
17	9.8				1981NOV18
17	9.63		10.40		1981NOV19
17	9.8				1981NOV20
17	9.76		10.49		1982JAN16
19	9.2		10.3		1975
19	9.94	0.1	10.35	0.1	1976
19	9.4				1981FEB06
19	9.9				1981FEB06
19	9.0				1981FEB12
19	9.3				1981FEB12
19	10.1				1981NOV18
19	9.80		11.23		1981NOV19
19	9.67		11.06		1982JAN16

Table 3c continued

Variability in NGC 2068

Name	K^a	$\sigma(K)^b$	H^a	$\sigma(H)^b$	date[c]
20	8.90	0.2			1975
20	9.64	0.1	10.20	0.1	1976
20			10.6		1981FEB03
20	9.9				1981NOV18
20	9.7				1981NOV20
26	8.8				1975
26	9.87	0.1	10.10	0.1	1976
26			10.6		1981FEB03
26			10.3		1981FEB03
26	9.6				1981FEB12
26	9.6				1981FEB12
26	10.1				1981NOV17
26	9.74		10.15		1981NOV19
26	9.86				1981NOV19
26a	9.60	0.2			1975
26a	10.1				1981NOV18
26a	10.15		10.48		1982JAN16
26b	10.00	0.2			1975
26b	10.5				1981NOV18
26b	10.62		11.00		1982JAN16
40	9.5				1975
40	10.1				1981SEP16
40	10.1				1981NOV11
40	10.7				1981NOV17
47	9.5				1975
47	10.33	0.1	10.86	0.25	1976
47			11.0		1981FEB03
47	10.4				1981FEB12
47	9.9				1981FEB12
47	10.6				1981SEP17
47	10.2				1981SEP19
47	10.3				1981NOV17
47	10.4				1981NOV20

(a) K and H magnitudes given to 0.1 mag are scan magnitudes, and are uncertain by $\gtrsim$ 0.3 mag. K and H magnitudes given to 0.01 mag are photometric magnitudes.

(b) Uncertainties are $\pm$ 1σ, and include both photometric and statistical uncertainties. The uncertainties are given only when greater than 0.05 mag for photometry; no uncertainties are given for scan magnitudes.

(c) Dates for which the year only is given are for observations by other observers, and refer to the year in which the data were published. The supplemental observations were taken from Strom *et al.* (1975), and Strom, Strom, and Vrba (1976).

Figure Captions

Fig. 1. $J-H$ *vs.* $H-K$ colors in magnitudes of the stars observed in (*a*) NGC 7023, (*b*) NGC 2023, and (*c*) NGC 2068. Error bars are $\pm 1\sigma$. Filled circles indicate observations from this paper, while open circles in Fig. 2(*c*) indicate observations from Strom, Strom, and Vrba (1976). The solid curve is the main sequence, from A0V to M5V. The solid line indicates the expected reddening line for a background K giant, while the dashed line indicates the reddening line for an A0V star.

Fig. 2. Plot of positions of stars found in (*a*) NGC 7023, (*b*) NGC 2023, and (*c*) NGC 2068. Pluses indicate stars found at 2.2 or 1.65 μm, open circles indicate stars found at 0.655 or 0.8 μm, and an asterisk indicates the visual illuminating star of each reflection nebula. The solid outline indicates the scan area for the scans at 2.2 μm from which complete samples of stars were drawn, while the dashed outline indicates additional area scanned at 2.2 μm.

Fig. 3. Cumulative counts $N(K)$ *vs.* observed K magnitude for the stars in NGC 2068. The cumulative counts are given as number of stars per square degree brighter than the observed K magnitude. Error bars are $\pm 1\sigma$. The indicated line is a least squares fit of the function $N(K) = N_0\, 10^{\gamma K}$ to the data.

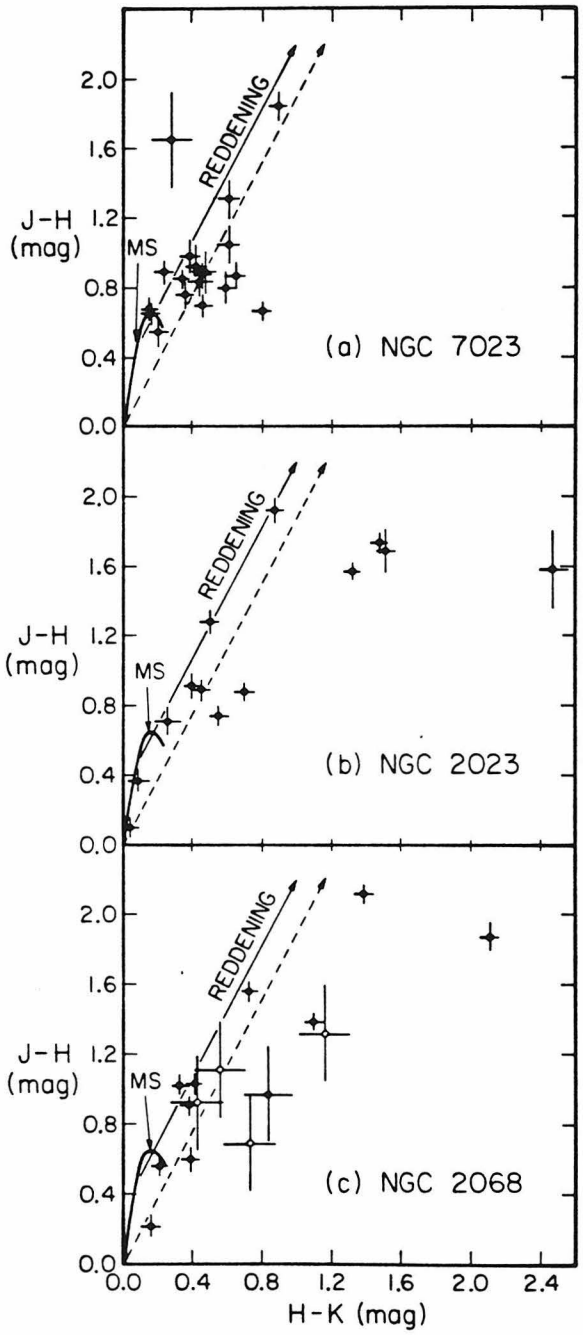
REDDENING
MS
(a) NGC 7023
(b) NGC 2023
(c) NGC 2068
J-H (mag)
H-K (mag)
0.0
0.4
0.8
1.2
1.6
2.0
2.4

Figure 1

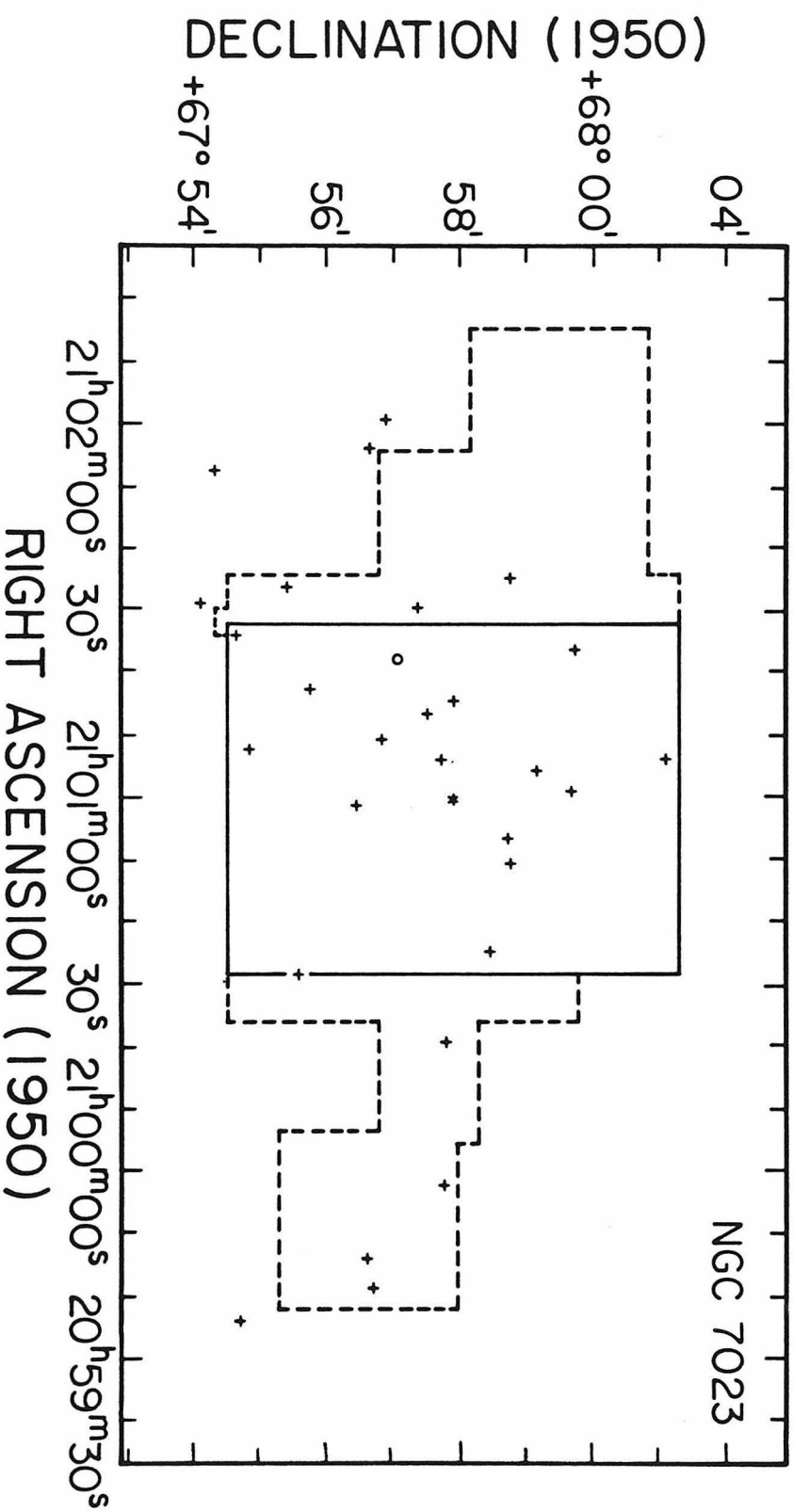
DECLINATION (1950)
+67° 54'
56'
58'
+68° 00'
04'
NGC 7023
21h02m00s
30s
21h01m00s
30s
21h00m00s
20h59m30s
RIGHT ASCENSION (1950)

Figure 2a

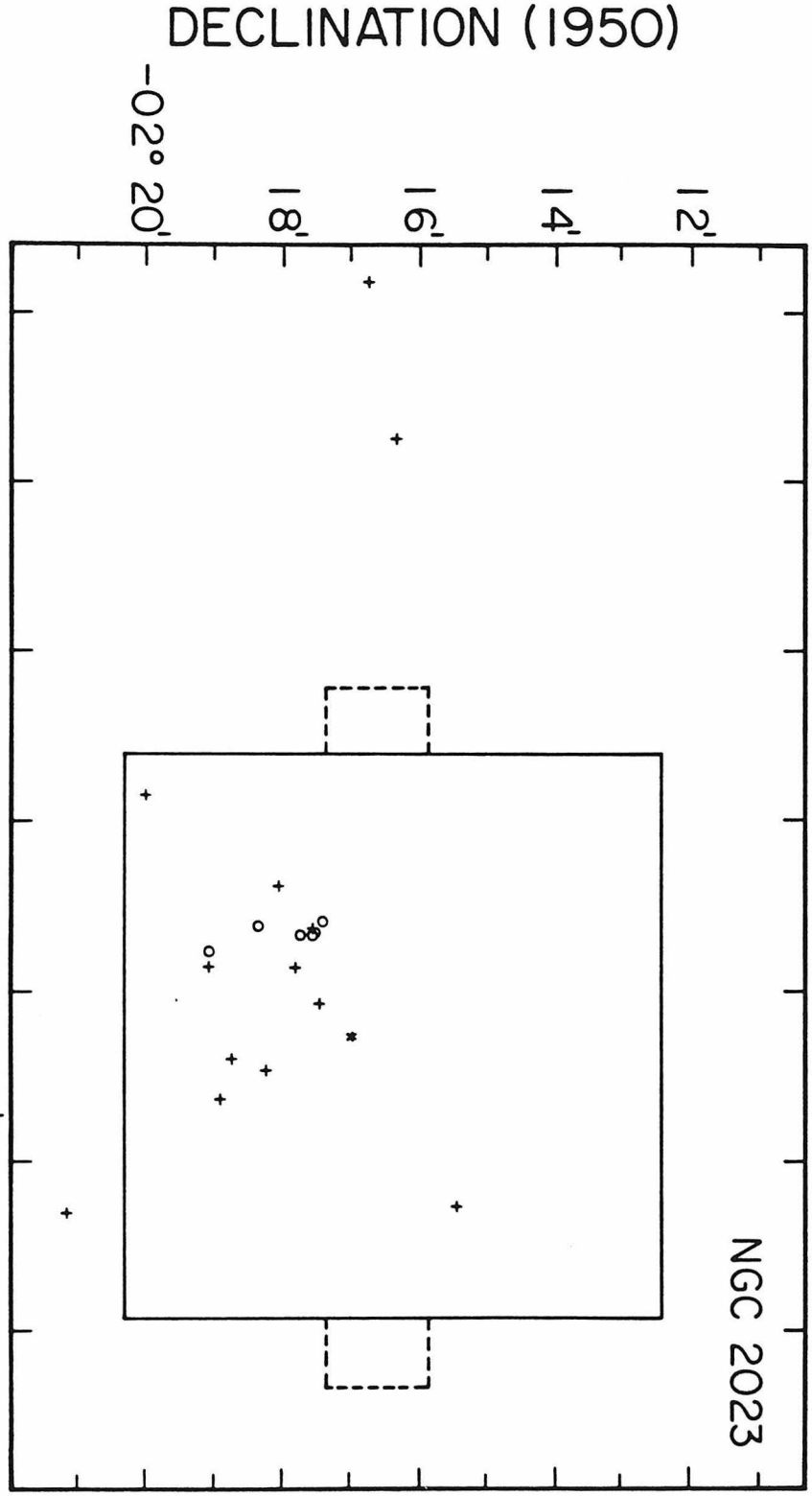
DECLINATION (1950)
-02° 20'
18'
16'
14'
12'
50s
40s
30s
20s
10s
05h 39m 00s
50s
RIGHT ASCENSION (1950)
NGC 2023

Figure 2b

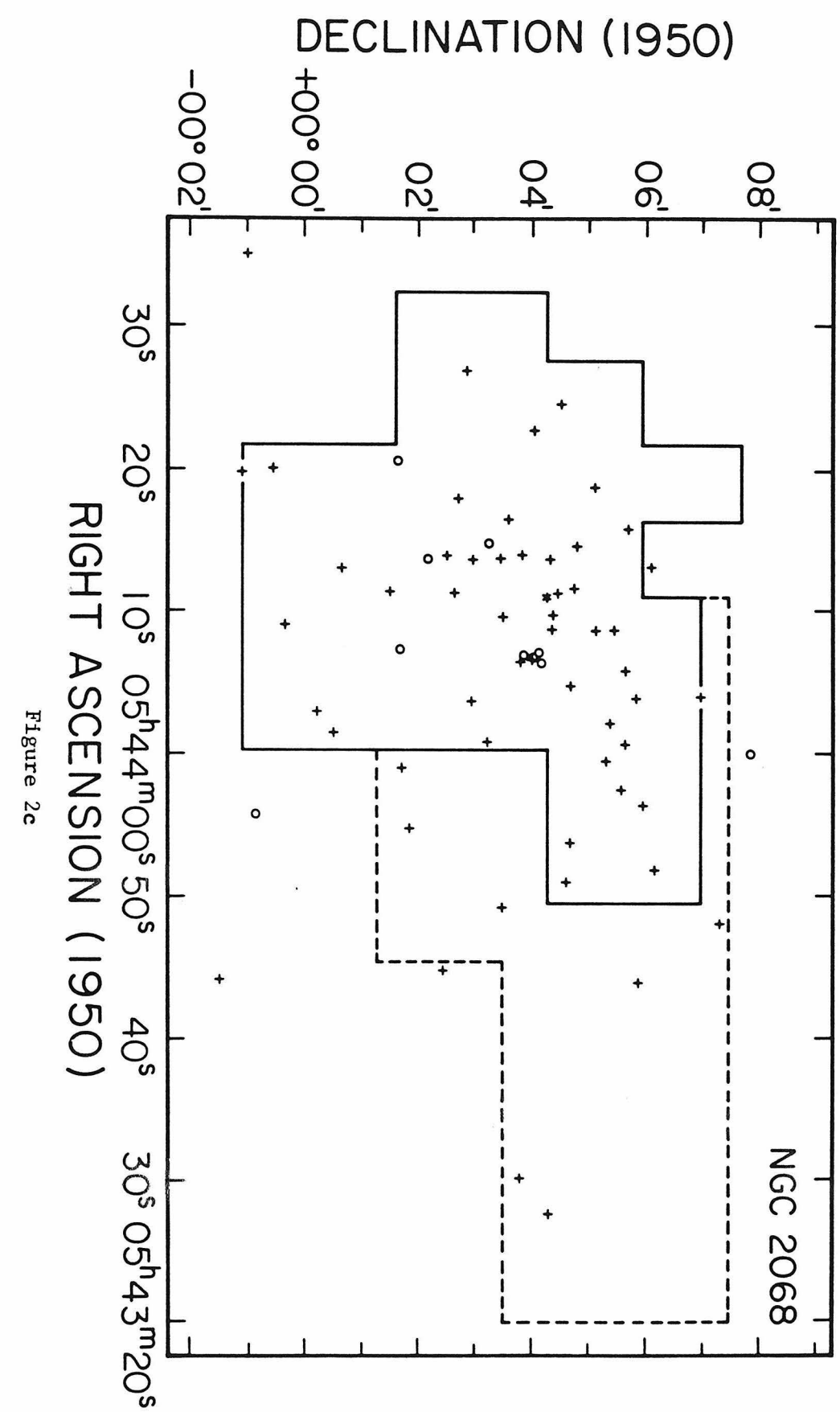
DECLINATION (1950)
+00° 00'
02'
04'
06'
08'
-00° 02'
30s
20s
10s
05h44m00s
50s
40s
30s
05h43m20s
RIGHT ASCENSION (1950)
NGC 2068

Figure 2c

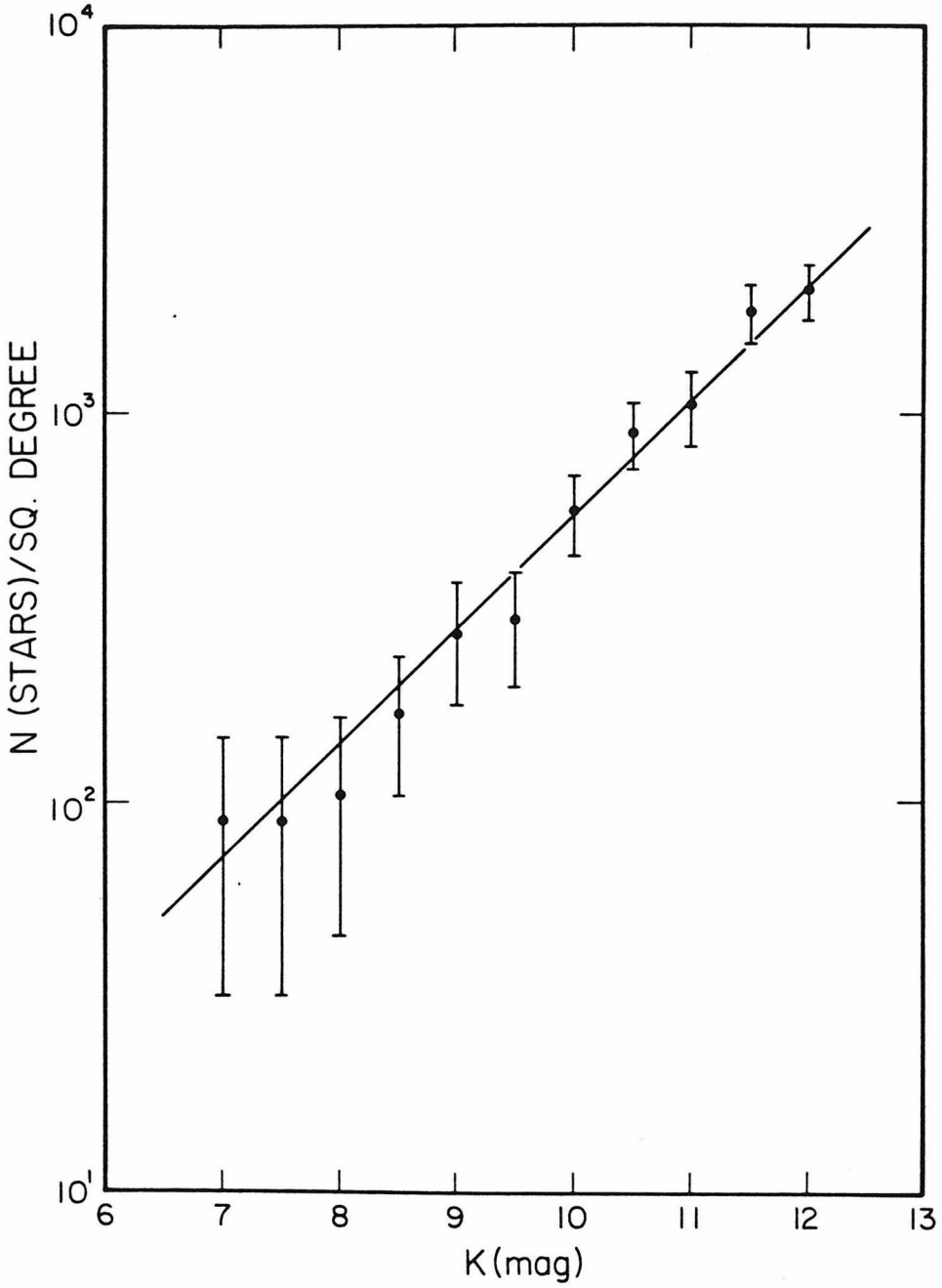

Figure 3